DISSECTING THE PHYSICAL PROPERTIES OF THE CHROMATIN SPRING IN MITOSIS

Andrew Stephens

A dissertation submitted to the faculty of the University of North Carolina at Chapel Hill in partial fulfillment of the requirements for the degree of Doctor of Philosophy in the Department of Biology.

Chapel Hill
2013

Approved by:

Kerry Bloom

Richard Cheney

Bob Goldstein

Ken Jacobson

Steve Rogers

ABSTRACT

ANDREW STEPHENS: DISSECTING THE PHYSICAL PROPERTIES OF THE CHROMATIN SPRING IN MITOSIS
(Under the direction of Kerry Bloom)

During cell division it is essential that each daughter cell receives a full copy of the genome. The mitotic spindle apparatus, composed of microtubules and chromatin, faithfully segregates the duplicated genome equally between daughter cells. Microtubules bind to sister chromatids and exert extensional forces towards opposite poles. The pericentric chromatin surrounding the attachment site resists the microtubule forces with contractile spring-like prosperities. Tension generated from these opposing forces silences the spindle checkpoint to ensure accurate segregation. Using budding yeast as a model system we find that the chromatin spring is composed of the intramolecular pericentromere loop along with SMC protein complexes cohesin and condensin. Simulations of the pericentric chromatin as a non-linear spring accurately recapitulate *in vivo* spindle and chromatin dynamics. This is contrary to the dogma that the chromatin spring is linear. In addition, we find that the pericentromeres of the 16 different chromosomes in yeast physically interact and behave as an ensemble. The interlinked network of attachment sites in the yeast spindle provides insight as to how multiple attachments sites function in a mammalian kinetochore. Cohesin, condensin and the pericentromere compose an interlinked network of chromatin springs that equalizes tension over multiple dynamic attachment sites to aid the faithful segregation of the genome in mitosis.

ACKNOWLEDGMENTS

I would like to thank all the people that have been involved in my growth as a scientist and as a person. UNC has been has been a wonderful place to learn.

To Bob, Steve, Ken, and Richard – My Committee

Thank you for your guidance and your insightful words over the course of graduate school. You are my A-Team (reference pending). I appreciate all of your view points and helpful guidance.

To Kerry Bloom

You are a great scientist and an even better person. Thank you for giving me the opportunity to chase my dreams as a scientist in your lab. Your teachings and experience will be instrumental in my continuing success as I pursue my scientific career.

To Leandra Vicci, Russ Taylor, and Mike Falvo – Physics Group

Thank you for collaborating with me for the majority of my graduate research. I have learned so much from our wonderful talks. I will always be grateful for all that you have taught me and helped me accomplish.

To Greg Forest, Paula Vasquez, and Yuan Jin – Math Group

Thank you for your ingenuity and aid in talking complex mathematical problems. I will always appreciate your commitment and collaboration that enabled us complete the projects at hand.

To Binny Chang, Rei Haggerty, Chloe Snider, Laura Fulbright – Undgraduates

Thank you for all your hard work. I could not have accomplished all that I have without your extra set of hands and strong minds. It has been a pleasure teaching you. I hope you enjoyed it as much as I have.

To Julian, Ben, and Jolien – Lab mates and friends

You are the best lab mates in the world. I owe a lot of my success to your support, experimental aid, and insightful conversations. Working alongside of you all has been motivating, enjoyable, and an experience I won't forget.

To Nehemiah, Adam, and Kang – Friends

Thank you for being my partners in crime to blow off steam and have fun. I will never forget all the memories we created and I look forward to creating more.

To Leo – Better Half

Thank you for letting me talk about science every day and supporting me in all of my endeavors. I look forward to spending my life with you.

To Mom, Dad, and Ryan – Family

You are the best nuclear family. Thank you for your support in every way possible. You are with me every step of the way and I could not have done it without. I love you all so much.

TABLE OF CONTENTS

LIST OF TABLES

LIST OF FIGURES

ABBREVIATIONS

3C	Chromosome Confirmation Capture
4C	Chromosome to Chromosome Conformation Capture
CEN	Centromere
CLS	Coupled Linear Stochastic model
CNLS	Coupled Non-Linear Stochastic model
DIC	Differential Interference Contrast
GALCEN	Galactose Promoter-Centromere
GFP	Green Fluorescent Protein
Gal-H3	Galactose-inducible Histone H3 protein
kb	Kilobases
LacO/I	Lactose Operator/Repressor
MLS	Minimal Linear Stochastic model
PCR	Polymerase Chain Reaction
rDNA	Ribosomal DNA
SMC	Structural Maintenance of Chromosomes
TetO/R	Tetracycline Operator/Repressor
WLC	Worm-like chain

CHAPTER 1

COHESIN, CONDENSIN, AND THE INTRAMOLECULAR CENTROMERE LOOP TOGETHER GENERNATE THE MITOTIC CHROMATIN SPRING

This chapter is adapted from a publication in The Journal of Cell Biology (Stephens et al., 2011). Julian Haase, Leandra Vicci, Russell M. Taylor II, and Kerry Bloom aided in experiments, analysis of data, and writing.

Summary

Sister chromatid cohesion provides the mechanistic basis together with spindle microtubules for generating tension between bioriented chromosomes in metaphase. Pericentric chromatin forms an intramolecular loop that protrudes bi-directionally from the sister chromatid axis. The centromere lies on the surface of the chromosome at the apex of each loop. The cohesin and condensin SMC protein complexes are concentrated within the pericentric chromatin, but whether they contribute to tension-generating mechanisms is not known. To understand how pericentric chromatin is packaged and resists tension, we map the position of cohesin (*SMC3*), condensin (*SMC4*) and pericentric LacO arrays within the spindle. Condensin lies proximal to the spindle axis and is responsible for axial compaction of pericentric chromatin. Cohesin is radially displaced from the spindle axis and confines pericentric chromatin. Pericentric cohesin and condensin contribute to spindle length

regulation and dynamics in metaphase. Together with the intramolecular centromere loop, these SMC complexes constitute a molecular spring that balance spindle microtubule force in metaphase.

Introduction

Metaphase is the crucial stage in mitosis when condensed sister chromatids are tethered by cohesin and bioriented along the mitotic spindle in preparation for chromosome segregation. The fidelity of chromosome segregation involves the balance of the microtubule-based outward force with chromatin-based inward force. Each chromosome is attached to the spindle microtubules via the kinetochore, a specialized protein-DNA structure built at the centromere (Bouck et al., 2008; Cheeseman and Desai, 2008). Upon attachment of sister kinetochores to the mitotic apparatus, tension is generated between sister chromatids and consequently the pericentromere chromatin (Tanaka et al., 2000; Goshima and Yanagida, 2000; Pearson et al., 2001). Chromatin provides an inward force opposing the outward-directed microtubule force (Bloom and Joglekar, 2010). However, the molecular basis of this chromatin inward force has not been well characterized.

In budding yeast the streamlined mitotic spindle provides an ideal model for biophysical studies. There are a limited number of microtubules (16 kinetochore microtubules and 4 interpolar microtubules from each pole, 40 microtubules per spindle; Winey et al., 1995). The centromeres are defined by DNA sequence (Fitzgerald-Hayes et al., 1982) and the 32 centromeres from 16 replicated chromosomes cluster into two foci upon biorientation in metaphase (Goshima and Yanagida, 2000; Pearson et al., 2004). Interpolar microtubules serve as tracks along which motor proteins move and act as struts to stabilize

the bipolar spindle. The major function of microtubule motors within the spindle is to slide anti-parallel microtubules apart generating an outward spindle elongation force (Saunders and Hoyt, 1992). The pericentric chromatin opposes the action of the microtubule-based motor proteins (Bouck and Bloom, 2007). The decompaction of chromatin upon reduction of one of the core histones (H3) leads to increased metaphase spindle length. The increase in spindle length is suppressed by loss of a microtubule-based motor protein, Kip1 or Cin8. The finding that pericentric chromatin length responds to the concentration of motor proteins led to the hypothesis that chromatin is an elastic spring.

The simplest form of an elastic spring is a Hookean spring in which applied force leads to a linear increase in length (see Figure 1.6 A). As chromatin is composed of approximately equal weight DNA and protein, the physical properties of both are likely to contribute to properties of the spring. DNA behaves as a charged polymer that adopts a random coil conformation *in vitro*. The random coil reflects the tendency of individual monomeric units within the polymer to adopt a conformation with the greatest number of available states (i.e. greatest entropy). A model that describes this behavior is a worm-like chain (WLC; see Figure 1.6 A; Bustamante et al., 1994; Peters and Maher, 2010). At low force regimes small changes in force result in large length changes since entropic force is exceedingly small. At high force regimes, where the polymer approaches its full contour length (~90%), large changes in force result in small changes in length due to the large force it takes to stretch covalent bonds. To understand how tension is distributed between sister chromatids and how the tension sensing spindle checkpoint functions, it is critical to determine whether chromatin springs behave with Hookean or worm-like chain properties or both.

Micromanipulation of mitotic chromosomes reveals that their elasticity is dictated by both DNA and protein components. The major classes of non-histone proteins that are likely to contribute to mitotic chromatin elasticity are topoisomerases, cohesin and condensin (Almagro et al., 2004; Kawamura et al., 2010). Cohesin's main function is to hold together sister chromatid strands while condensin's main function is to condense chromatin (Hirano, 2006; Nasmyth and Haering, 2009). Both cohesin and condensin are enriched in the pericentric chromatin by ChIP (Megee et al., 1999; Tanaka et al., 1999; Glynn et al., 2004; Weber et al., 2004; D'Ambrosio et al., 2008; Hu et al., 2011). The perturbation of pericentric cohesin or condensin results in the loss of proper tension sensing and error correction in metaphase (Yong-Gonzalez et al., 2007; Ng et al., 2009). Depletion of condensin leads to increased centromere stretching and dynamics in mammalian cells. This may indicate a role for a rigid spring in controlling chromosome dynamics and constant tension at the centromere (Samoshkin et al., 2009; Uchida et al., 2009; Ribeiro et al., 2009). Furthermore, cohesin has been demonstrated to set up kinetochore geometry (Sakuno et al., 2009) and experiments in *C. elegans* reveal that condensin is required for centromere resolution (Moore et al., 2005). Therefore, cohesin and condensin contribute to the architecture and elastic properties of the pericentric chromatin.

In this study we have used digital microscopy and live cell dynamics to deduce the spatial distribution of cohesin, condensin and DNA within the pericentric chromatin. Pericentric condensin is proximal to the spindle axis while pericentric cohesin is distal to the mitotic spindle axis. Analysis of spindle and pericentric chromatin dynamics in cohesin and condensin mutants reveal that the intramolecular loop of pericentric chromatin, cohesin and condensin behave as a molecular spring with WLC properties *in vivo*.

Results

Pericentric cohesin and condensin are spatially segregated

Cohesin and condensin are enriched in the pericentric region, but exhibit distinct patterns of localization. Cohesin (Smc3) exhibits a bi-lobed structure when viewed from the side (sagittal section of spindle; Figure 1.1 A ; Yeh et al., 2008). In contrast, condensin (Smc4) is enriched along the spindle axis as well as the nucleolus (white arrow, Figure 1.1 A). The fraction of Smc4-GFP between the spindle poles is heterogeneous and appears either as a single focus, two foci or a uniform distribution bounded by the spindle poles. These patterns occur in approximately equal frequencies (n = 80, Figure 1.1 A). Thus, cohesin and condensin are differentially localized in the metaphase spindle (Bachellier-Bassi et al., 2008).

We utilized line scan data from single cells (Figure 1.1, A and B) and ensemble averaged images (Figure 1.1 C) of cohesin and condensin to deduce the structures containing these protein complexes. Single plane images taken with both spindle pole bodies in focus (sagittal section) were aligned horizontally. Each image was individually scanned along the x and y axis through the brightest pixel to obtain the average distribution of Smc3 and Smc4 in the metaphase spindle. All single cell images were then compiled into an ensemble average image (Figure 1.1 C). Line scans of the Smc3-GFP cohesin barrel yielded a peak-to-peak width of 373 ± 63 nm and length of 560 ± 118 nm (n = 34, Figure 1.1 C). Transverse (end-on) images of cohesin display an area of low fluorescence signal and yielded a peak-to-peak measurement of 475 ± 62 nm (n = 22, Figure 1.1 B). Condensin is proximal to the spindle axis and shows no bi-lobed structure in sagittal images. In transverse images condensin

appears as a single focus with no resolvable area of reduced fluorescence (Figure 1.1 B). Line scans of single plane Smc4-GFP sagittal images yielded a single peak with a Gaussian distribution 303 ± 51 nm wide (full-width half-maximum, Figure 1.1 C) and 636 ± 198 nm in length (n = 51). Ensemble averaged images and line scan analysis reveal that cohesin and condensin occupy two separate sub domains within the pericentric chromatin.

To position pericentric cohesin and condensin relative to known structures in the spindle, we analyzed kinetochore proteins Nuf2 and Ndc80. Nuf2-GFP and Ndc80-GFP appear as two distinct foci, marking the plus-ends of kinetochore microtubules (Goshima and Yanagida, 2000; Pearson et al., 2004). Kinetochore microtubules emanate from the spindle pole body and lie within an approximately 250 nm diameter around the spindle pole bodies (Winey et al., 1995; Gardner et al., 2005). Line scans of Nuf2-GFP and Ndc80-GFP yielded a Gaussian distribution of 291 ± 14 nm and 288 ± 11 nm respectively (full-width half-maximum, n = 21 and 24, Figure 1.1 C). Line scans of condensin have the same peak position along the spindle axis as kinetochores (Figure 1.1 D). These data reveal that condensin resides along the spindle axis between the sister kinetochores. In contrast, line scans of cohesin reveal two peaks surrounding the spindle axis (Figure 1.1 D). Pericentric cohesin is radially displaced from pericentric condensin and the spindle microtubules.

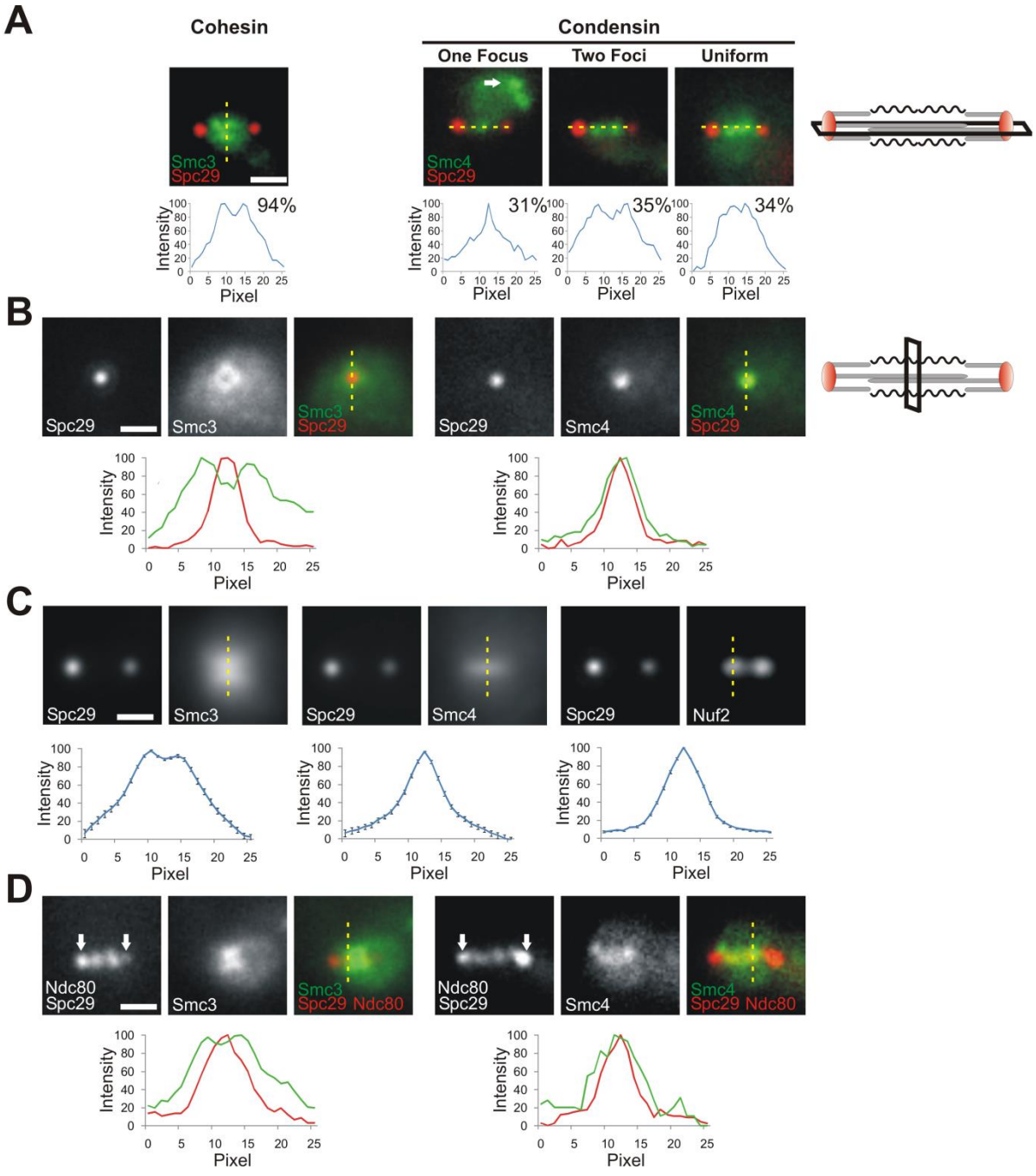
A
Cohesin
Condensin
One Focus
Two Foci
Uniform
Smc3
Spc29
Smc4
Spc29
94%
31%
35%
34%
Intensity
Pixel
B
Spc29
Smc3
Smc3
Spc29
Spc29
Smc4
Smc4
Spc29
C
Spc29
Smc3
Spc29
Smc4
Spc29
Nuf2
D
Ndc80
Spc29
Smc3
Smc3
Spc29 Ndc80
Ndc80
Spc29
Smc4
Smc4
Spc29 Ndc80

Figure 1.1 Localization of cohesin and condensin in the pericentric chromatin

(A) Smc3-GFP (cohesin) and Smc4-GFP (condensin) are enriched in the metaphase spindle between spindle pole bodies (Spc29-RFP). Line scan (yellow line) of Smc3-GFP perpendicular to the spindle axis shows cohesin has a bi-lobed enrichment. Line scans (yellow line) of Smc4-GFP taken along the spindle axis and between spindle pole bodies revealed three distinct classes of pericentric condensin enrichment: one focus, two foci and uniform distribution left to right (n = 80, with percentages listed). Condensin rDNA localization is labeled with a white arrow. (B) Transverse (end-on) images of Smc3-GFP display an area of low fluorescence and are displaced from the spindle pole. Smc4-GFP displays a diffraction limited spot in line with the spindle pole body. Vertical line scans (yellow line) are shown below. (C) Ensemble average images of Smc3-GFP, Smc4-GFP, and Nuf2-GFP (kinetochore protein) were generated by aligning and scaling multiple single plane images of each protein. Line scans (yellow line) of single plane images were averaged and graphed to quantify the distribution. The error bars represent SEM. (Smc3 n = 34, Smc4 n = 51, Nuf2 n = 30) (D) Images of Smc3 and Smc4 relative to the kinetochore (Ndc80) and spindle poles (Spc29, white arrows). Line scans (yellow line) are shown below. All line scan graphs display relative fluorescence intensity plotted vs. distance in pixels (65 nm/pixel). Scale bars = 1 μm.

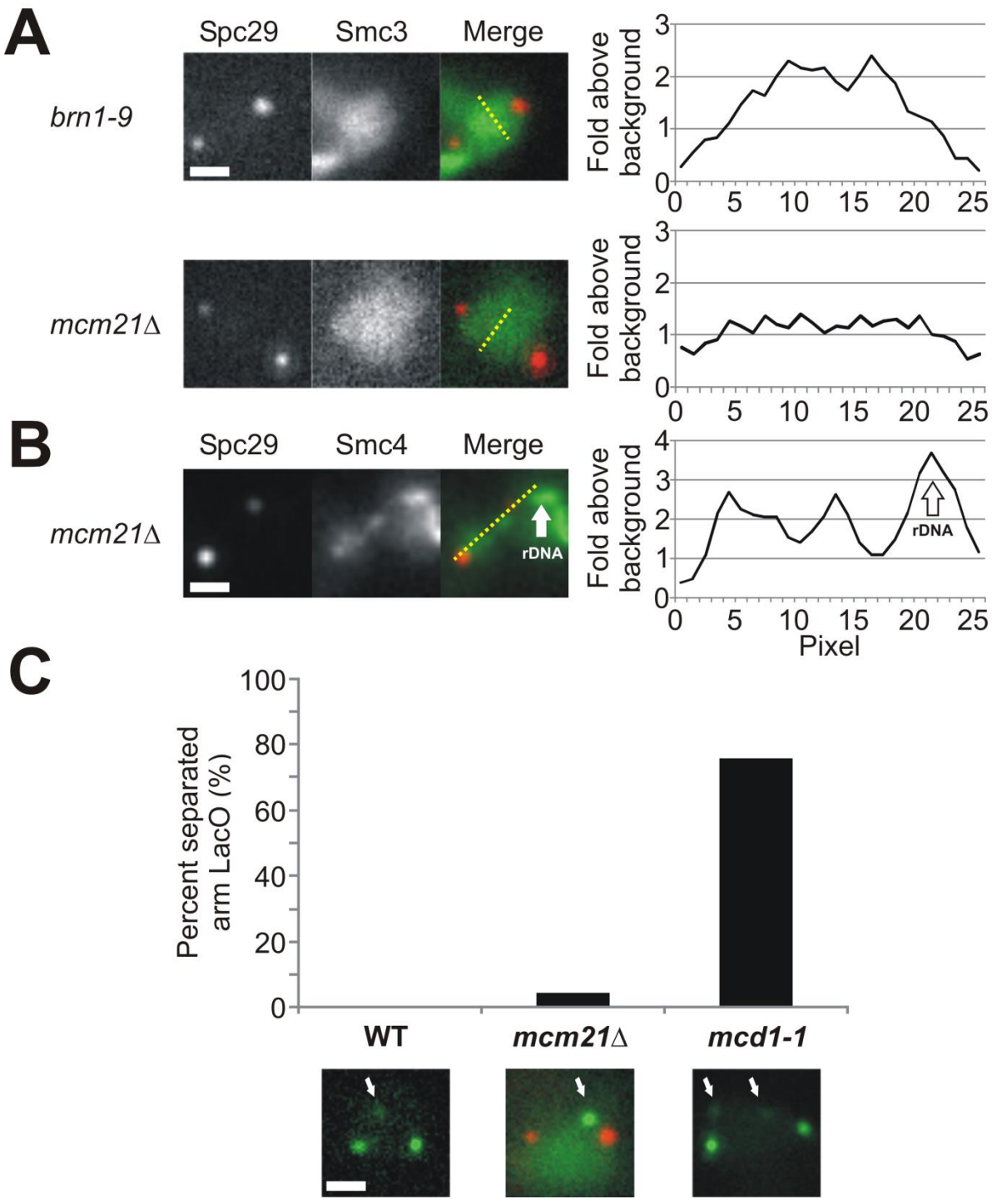
A
Spc29
Smc3
Merge
brn1-9
mcm21Δ
Fold above background
B
Spc29
Smc4
Merge
mcm21Δ
rDNA
Pixel
C
Percent separated arm LacO (%)
WT
mcm21Δ
mcd1-1

Figure 1.2 Deletion of *MCM21* specifically decreases pericentric cohesin

(A) Representative image of cohesin (Smc3-GFP) and spindle pole bodies (Spc29-RFP) in condensin mutant *brn1-9* and pericentric cohesin mutant *mcm21Δ*. Line scan (yellow dotted line) perpendicular to the spindle axis is graphed in relative fold intensity above background (nuclear background intensity = 1). (B) Representative image of condensin (Smc4-GFP) and spindle pole bodies (Spc29-RFP) in a pericentric cohesin mutant *mcm21Δ*. Line scan (yellow dotted line) along the spindle axis is graphed in relative fold intensity above background (nuclear background intensity = 1). (C) Graph of the percentage of total cells in which the *RAD16* arm loci LacO array is separated for wild-type and cohesin mutants *mcm21Δ* and *mcd1-1* (one experiment: wild-type $n = 14$, *mcm21Δ* $n = 23$, and *mcd1-1* $n = 45$) Scale bar = 1μm.

Cohesin and condensin contribute to metaphase spindle length and dynamics

To determine whether SMC protein complexes contribute to the physical properties of the spindle, we examined spindle dynamics in mutants that disrupt the organization of pericentric chromatin. We utilized temperature-sensitive alleles of cohesin *mcd1-1* (Guacci et al., 1997; Michaelis et al., 1997) and condensin *brn1-9* and *smc4-1* (Lavoie et al., 2000; Bachellier-Bassi et al., 2008), as well as deletion of the non-essential kinetochore protein Mcm21. Mcm21 is required for enrichment of pericentric cohesin leaving arm cohesin and pericentric condensin unimpaired (Figure 1.2; Eckert et al., 2007; Ng et al., 2009). To examine spindle length, we introduced markers for spindle pole bodies and measured the distance between them in metaphase. Metaphase spindles were defined by the presence of separated kinetochores greater than 200 nm from the spindle poles and by the lack of persistent elongation (over a 12 minute period). Wild-type spindle lengths were on average 1.46 ± 0.18 μm (n = 54, Figure 1.3 A). *mcd1-1* mutants at restrictive temperature displayed the largest increase in spindle length to 2.96 ± 1.03 μm (n = 50). Reduction of cohesin from the pericentric chromatin in *mcm21Δ* cells resulted in an average spindle length increase to 2.07 ± 0.46 μm (n = 72). Condensin mutants *brn1-9* and *smc4-1* at restrictive temperatures displayed an increase in spindle length to 2.3 ± 0.4 μm (n = 80) and 2.04 ± 0.55 μm (n = 19) respectively. In comparison, repression of H3 histones (Gal-H3), which decreases nucleosome occupancy to approximately 50% (Bouck and Bloom, 2007), resulted in an average spindle length of 2.45 ± 0.34 μm (n = 41). Cells arrested in metaphase by Gal-CDC20 repression (Hartwell et al., 1973) displayed a small increase in spindle length (1.72 ± 0.27, n = 52), but significantly less than observed in the mutants. Therefore, cohesin, condensin and nucleosomes contribute to spindle length regulation.

To reveal if the increase in spindle length upon depletion of histones, cohesin or condensin altered spindle length stability, we analyzed spindle length variation over time. Variation in spindle length was calculated by the absolute value of the difference between spindle length at each time point and the mean spindle length over a 12 minute live single cell time-lapse. Variation represents the standard deviation of all single time points across multiple cells. In wild-type cells the spindle achieved a length of 1.46 μm with an average variation in length of 109 nm (*n* = 180, Figure 1.3 B). Upon histone repression, the spindle increased in length, but exhibited variation comparable in magnitude to wild-type, 105 nm (Gal-H3 *n* = 740, Figure 1.3, B and C). This indicates that variation is not a consequence of increased spindle length. Likewise, cells arrested in metaphase (Gal-CDC20) had similar spindle length variation as wild-type metaphase cells, 114 nm (*n* = 321), suggesting spindle length variation is not a consequence of metaphase arrest/delay.

Depletion of pericentric cohesin (*mcm21Δ*) or pericentric and arm cohesin (*mcd1-1*) resulted in a significant increase in spindle length variation (*mcm21Δ* 208 nm, *n* = 600; *mcd1-1* 439 nm, *n* = 859). Likewise, increased variation was observed upon depletion of condensin (*brn1-9* 217 nm, *n* = 541; *smc4-1* 214 nm, *n* = 706, Figure 1.3, B and C). The increased length variation results from the changing distance between kinetochores and not kinetochore microtubule length (Figure 1.4 B). These data indicate that changes in chromatin length and not kinetochore microtubules are the source of spindle length fluctuations. Furthermore, cohesin and condensin are necessary to maintain a steady state spindle length and thus serve a different mechanical function from nucleosomes.

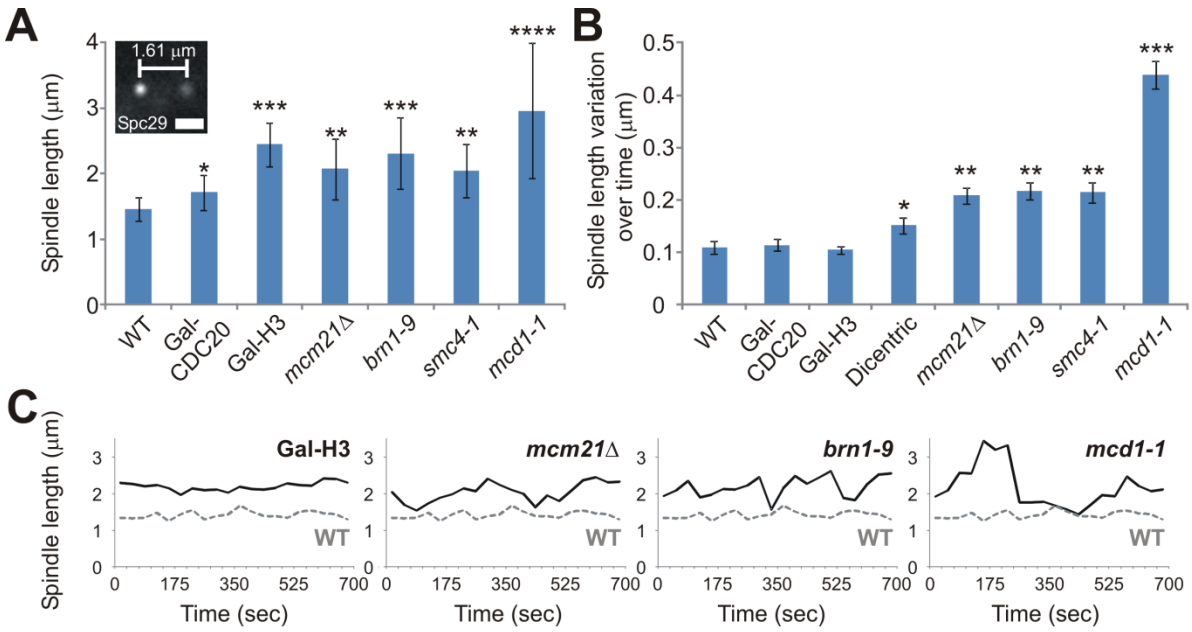
A
Spindle length (μm)
1.61 μm
Spc29
WT
Gal-CDC20
Gal-H3
mcm21Δ
brn1-9
smc4-1
mcd1-1
B
Spindle length variation over time (μm)
Dicentric
C
Gal-H3
mcm21Δ
brn1-9
mcd1-1
WT
Time (sec)

Figure 1.3 Spindle length and variation increase upon depletion of cohesin and condensin

(A) Spindle length was measured between the spindle pole bodies (Spc29-RFP) in metaphase cells of wild-type, Gal-CDC20, Gal-H3, cohesin mutants: *mcm21Δ* and *mcd1-1*, and condensin mutants: *brn1-9* and *smc4-1*. Cells were followed over time to ensure measurements were taken in metaphase and not in linearly increasing anaphase spindles. Error bars represent standard deviation. (B) Spindle length variation over time in metaphase is graphed for wild-type, Gal-CDC20, Gal-H3, cohesin mutants: *mcm21Δ* and *mcd1-1*, condensin mutants: *brn1-9* and *smc4-1*, and cells containing an active dicentric chromosome. Spindle pole bodies were filmed at 35 second intervals for 11.7 minutes. Variation in spindle length was calculated by the absolute value of the difference between spindle length at each time point and the mean spindle length over a time-lapse. Error bars represent 95% confidence. (A, B) Mutants that are statistically significant different ($P < 0.05$) from wild-type were marked with an asterisk (*). Mutants with the same number of asterisks are statistically similar ($P > 0.05$) while different number of asterisks are statistically different ($P < 0.05$). (C) Representative graphs of spindle length over time for Gal-H3, *mcm21Δ*, *brn1-9* and *mcd1-1*(black lines). Wild-type is graphed (gray line) for comparison.

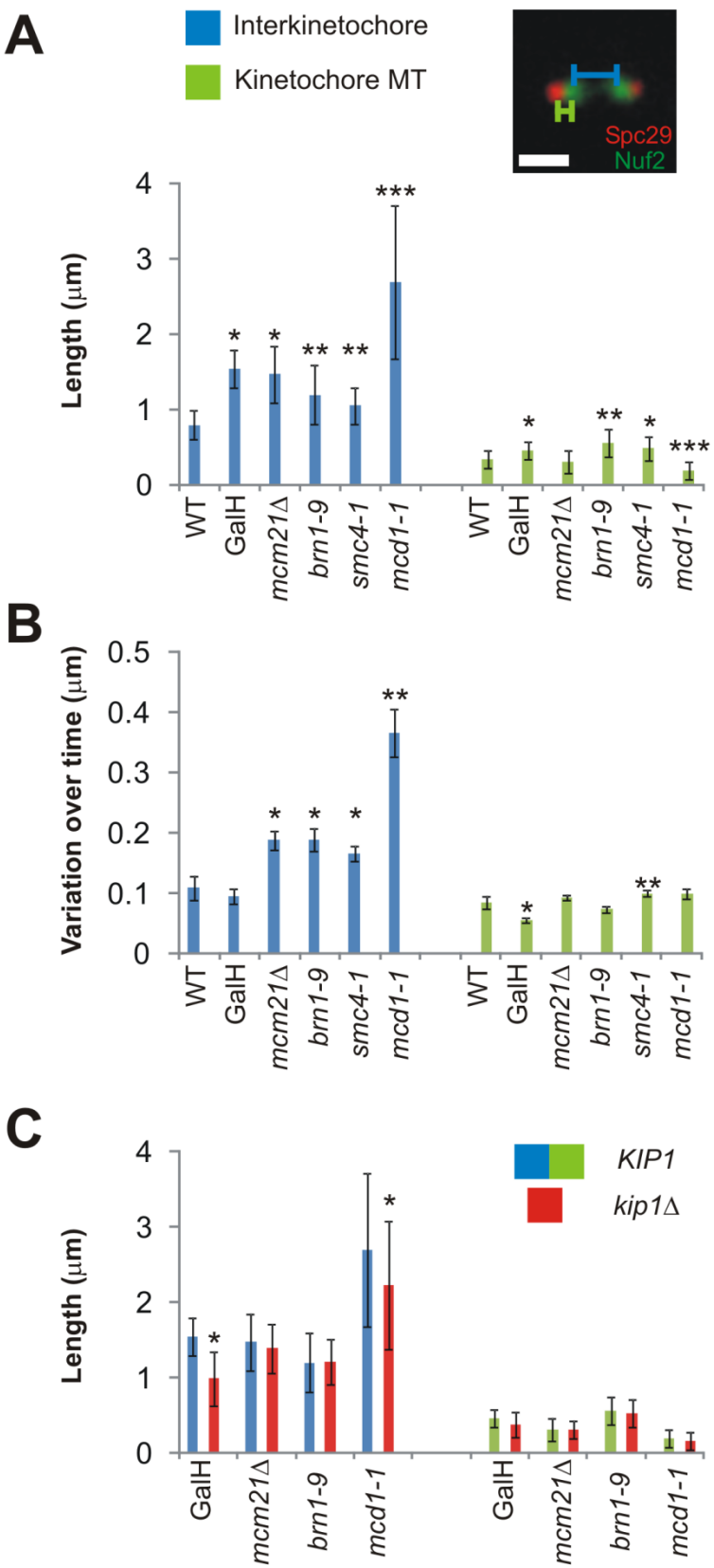
A
Interkinetochore
Kinetochore MT
H
Spc29
Nuf2
Length (μm)
0
1
2
3
4
*
*
**
**
***
*
**
*
***
WT
GalH
mcm21Δ
brn1-9
smc4-1
mcd1-1
WT
GalH
mcm21Δ
brn1-9
smc4-1
mcd1-1
B
Variation over time (μm)
0
0.1
0.2
0.3
0.4
0.5
*
*
*
**
*
**
WT
GalH
mcm21Δ
brn1-9
smc4-1
mcd1-1
WT
GalH
mcm21Δ
brn1-9
smc4-1
mcd1-1
C
KIP1
kip1Δ
Length (μm)
0
1
2
3
4
*
*
GalH
mcm21Δ
brn1-9
mcd1-1
GalH
mcm21Δ
brn1-9
mcd1-1

Figure 1.4 Interkinetochore and kinetochore microtubule length and variation

(A) Average interkinetochore (blue, distance between Nuf2-GFP foci) and kinetochore microtubule (green, distance between Spc29-RFP and adjacent Nuf2-GPF) length (wild-type *n* = 54, Gal-H3 *n* = 41, *mcm21Δ n* = 72, *brn1-9 n* = 80, *smc4-1 n* = 19 and *mcd1-1 n* = 50). Error bars represent standard deviation. Scale bar = 1 μm. (B) Average interkinetochore (blue) and kinetochore microtubule (green) length variation over time (wild-type *n* = 77, Gal-H3 *n* = 230, *mcm21Δ n* = 461, *brn1-9 n* = 234, *smc4-1 n* = 477 and *mcd1-1 n* = 274). Error bars represent 95% confidence. (A, B) Mutants that were statistically significant different ($P < 0.05$) from wild-type were marked with an asterisk (*). Mutants with the same number of asterisks were statistically similar ($P > 0.05$), while different number of asterisks were statistically significantly different ($P < 0.05$). (C) Interkinetochore and kinetochore microtubule lengths for single mutants (*KIP1*, blue and green) Gal-H3, *mcm21Δ*, *brn1-9* and *mcd1-1* and double mutants (*kip1Δ*, red; Gal-H3 *n* = 70, *mcm21Δ n* = 74, *brn1-9 n* = 69, and *mcd1-1 n* = 60). Statistically different ($P < 0.05$) *KIP1* vs. *kip1Δ* lengths are marked by an asterisks (*).

Intra- vs. Intermolecular cohesin function

The predominant function of cohesin in metaphase is to hold sister chromatids together. To distinguish the contribution to spindle dynamics of intermolecular cohesin function from the intramolecular centromere DNA loop, we have employed a dicentric chromosome in which cells initiate anaphase, but delay cell cycle progression in mid-anaphase with a single dicentric chromosome bridge (Figure 1.5 B; Yang et al., 1997). Mid-anaphase is defined by kinetochore to pole movement, shortening of kinetochore microtubules and spindle elongation (Yang et al., 1997; Gardner et al., 2008). Pericentric cohesin is destroyed within 3-5 minutes of anaphase onset (Yeh et al., 2008). If spindle dynamics requires intermolecular sister chromatid cohesion, then spindle length variation will be reduced (Figure 1.5 right). In contrast, if intramolecular force contributes to spindle dynamics, then the mid-anaphase spindle will exhibit length variation (Figure 1.5 left). There was a significant increase in spindle length variation to 151 nm (n = 303, from 109 nm in WT), but less than observed with loss of pericentric cohesin (*mcm21Δ*, 208 nm) or condensin (*brn1-9*, 217 nm; Figure 1.3 B and 1.5 C). Condensin could be contributing to the intramolecular chromatin spring properties because its function is independent of cohesin in anaphase (Lavoie et al., 2004). The elastic properties of chromatin are evident in a single chromosome bridge and therefore the chromatin spring does not require intermolecular cohesion between sister chromatids.

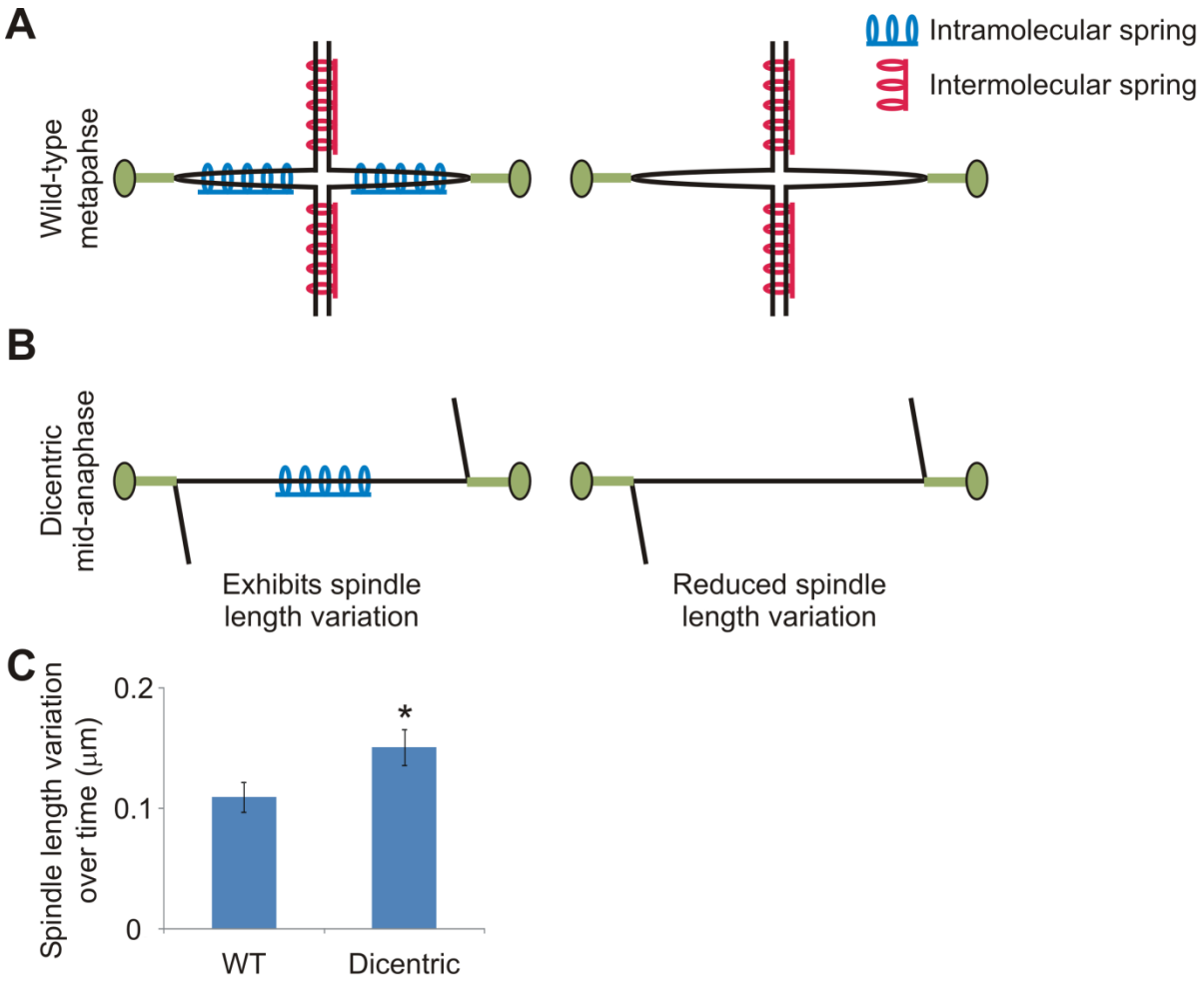
A
Intramolecular spring
Intermolecular spring
Wild-type metapahse
B
Dicentric mid-anaphase
Exhibits spindle length variation
Reduced spindle length variation
C
Spindle length variation over time (μm)
0.2
0.1
0
*
WT
Dicentric

Figure 1.5 Intra- and intermolecular chromatin springs

(A) A bioriented sister chromatid pair under tension in metaphase is shown as containing both intramolecular springs (pericentromere loop in blue) and intermolecular springs (sister cohesion in red; left) or only intermolecular springs (right). (B) Mid-anaphase spindle with a dicentric chromosome bridge. Cohesin is cleaved and monocentric chromosomes move to the spindle poles. The two centromeres on the same chromatid attach to opposite spindle poles, thereby creating a double-strand DNA chromosome bridge. Cell cycle progression is delayed in mid-anaphase for approximately 45 minutes (Yang et al., 1997). (C) Variation in spindle length is graphed for wild-type and the active dicentric (data replotted from Figure 1.3 B). The asterisk (*) denotes they are statistically different ($P < 0.05$). Error bars represent 95% confidence.

Physical properties of the intramolecular chromatin spring

To determine the physical properties of the chromatin spring, we introduced a mutation to reduce the magnitude of the outward-directed microtubule-based spindle force (Saunders and Hoyt, 1992; Straight et al., 1998). If pericentric chromatin behaves as a simple Hookean spring, then decreasing the outward force should cause the chromatin spring to recoil and decrease spindle length (Figure 1.6 A, black line). Alternatively, if the spring has worm-like chain properties, recoil is not linearly related to force (Figure 1.6 A, gray line). Upon deletion of the microtubule-based motor protein Kip1, spindles in wild-type (Saunders and Hoyt, 1992; Straight et al., 1998) and cells with reduced nucleosome occupancy (Bouck and Bloom, 2007) display an elastic response (Figure 1.6 B). In contrast, *mcm21Δ; kip1Δ* and *brn1-9; kip1Δ* double mutant cells showed no significant change in spindle length (*mcm21Δ* 1.97 ± 0.33 μm, n = 70; *brn1-9* 2.26 ± 0.51 μm, n = 74; Figure 1.6 B). Spindle length in *mcd1-1*; *kip1Δ* was reduced from 2.96 ± 1.03 μm to 2.42 ± 0.84 μm (n = 60), but not to the same extent as histone repression. Likewise, variation in spindle length was not rescued upon deletion of *KIP1* (Figure 1.6 C). Spindles lacking pericentric cohesin or condensin do not recoil as predicted for a simple Hookean spring (Figure 1.6, A and B). Either pericentric cohesin or condensin act as springs in the spindle, or the pericentric chromatin behaves as a worm-like chain approaching its full extension upon loss of cohesin or condensin (Figure 1.6, A and B).

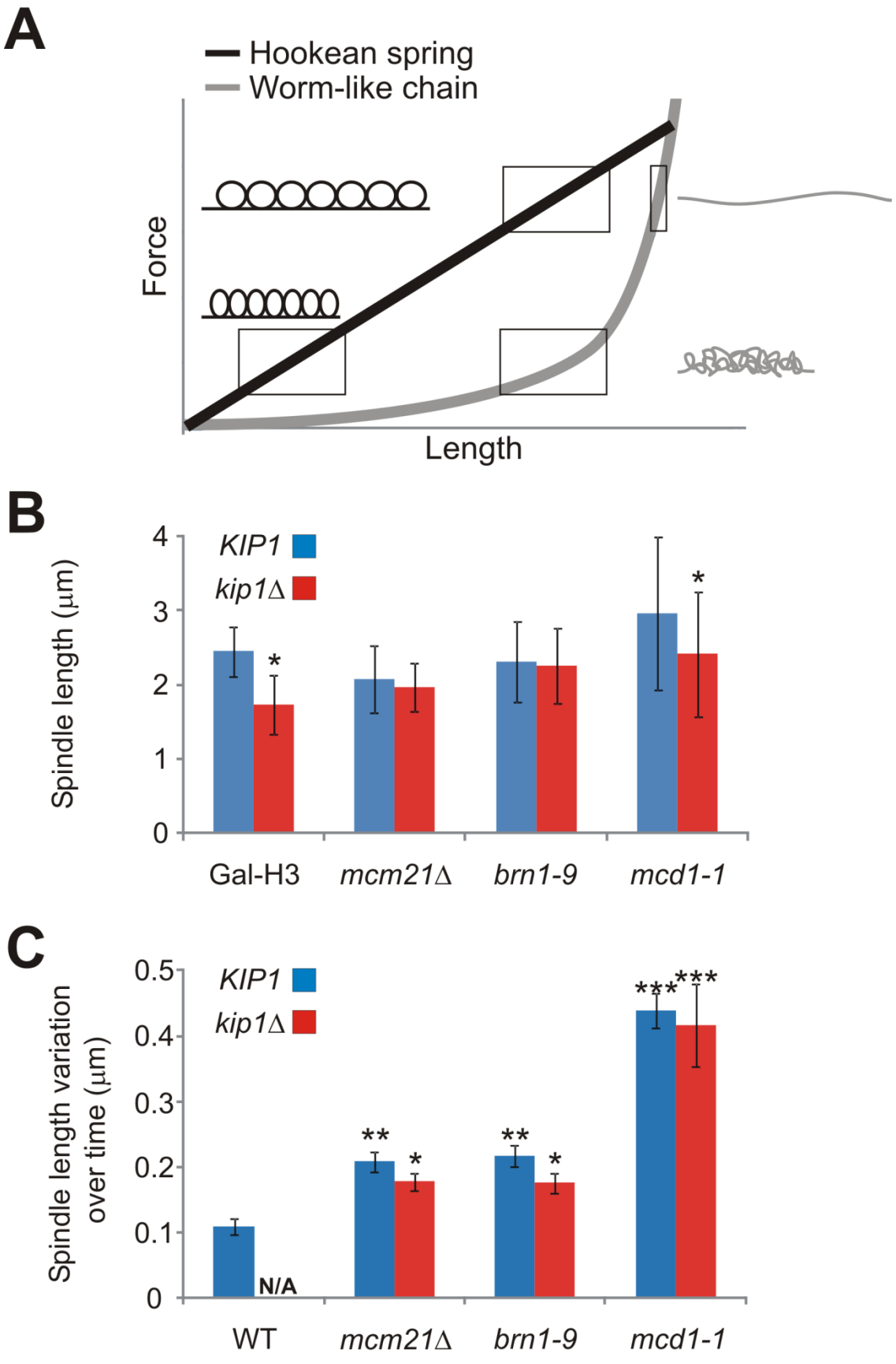
A
Hookean spring
Worm-like chain
Force
Length
B
Spindle length (μm)
KIP1
kip1Δ
0
1
2
3
4
*
*
Gal-H3
mcm21Δ
brn1-9
mcd1-1
C
Spindle length variation over time (μm)
KIP1
kip1Δ
0
0.1
0.2
0.3
0.4
0.5
N/A
**
*
**
*
***
***
WT
mcm21Δ
brn1-9
mcd1-1

Figure 1.6 Depletion of cohesin or condensin alters the elastic response of pericentric chromatin in cells deleted of KIP1

(A) A Hookean spring (black) has a linear force vs. extension curve where the force applied is proportional to length ($F= -k(x-x_0)$; F = force, k = spring constant, x_0 = rest length, x = extended length). Circles to left of force extension curve denote the structure of the spring at different values of force. A worm-like chain (WLC, gray) has an exponential force vs. extension curve ($F= (k_BT/P) [1/4(1 – x/L)^{-2} –1/4 + x/L]$; F = force, k_B = Boltzmann constant, T = temperature, P = persistence length, L = contour length, x = extended length). Gray lines to the right of the force extension curve denote the structure of the WLC at low force (random coil) and an extended chain (wavy line) at higher force. Large rectangles denote linear force vs. extension while the slim rectangle denotes non-linear portions. (B) Metaphase spindle length was measured between the spindle pole bodies (Spc29-RFP) in Gal-H3, *mcm21Δ*, *brn1-9*, and *mcd1-1* single mutants with *KIP1* (blue) and double mutants with *kip1Δ* (red). Error bars represent standard deviation. Statistically different ($P < 0.05$) *KIP1* vs. *kip1Δ* spindle lengths are marked by an asterisk (*). (C) Spindle length variation was measured by tracking the spindle pole bodies every 35 seconds for 11.7 minutes in Gal-H3, *mcm21Δ*, *brn1-9*, and *mcd1-1* single mutants with *KIP1* (blue) and double mutants with *kip1Δ* (red). Error bars represent 95% confidence. Statistically different ($P < 0.05$) spindle length variation than wild-type is marked with an asterisk (*). Mutants with the same number of asterisks are statistically similar ($P > 0.05$) while different number of asterisks are statistically different ($P < 0.05$).

Spring length versus extension

The increase in spindle length could arise from an increase in chromatin spring length or the degree of chromatin extension. To distinguish these possibilities, we examined the compaction of pericentric LacO arrays in wild-type and mutant cells. In wild-type cells pericentric-linked LacO arrays are dynamic and transiently separated in metaphase (Figure 1.7 A, wild-type; Tanaka et al., 2000; Goshima and Yanagida, 2000; Pearson et al., 2001). LacO arrays appear as spots or filaments indicative of chromatin decompaction and stretching (Figure 1.7 A; Bachant et al., 2002; Warsi et al., 2008). Stretching of a LacO array 6.8 kb from the centromere occurs in ~10% of wild-type cells (n = 167). Upon histone repression, LacO spot dynamics are indistinguishable from wild-type (n = 89, Figure 1.7 A; Bouck and Bloom, 2007). In contrast, stretching of the pericentric LacO arrays was observed in > 50% of cells depleted of pericentric cohesin or condensin (*mcm21Δ* n = 83 and *brn1-9* n = 106, Figure 1.7 A). In these cells the occurrence of stretched pericentric LacO spots was positively correlated with longer spindles (Figure 1.7 B). Time-lapse analysis of pericentric LacO in *mcm21Δ* and *brn1-9* cells revealed multiple stretching and recoil events occur with a similar time constant as spindle growth and shortening (Figure 1.8). The increased frequency of stretching reveals that the LacO arrays are more likely to adopt a linear conformation in the absence of condensin or cohesin. In contrast, the lack of stretching upon histone depletion reveals that the LacO arrays remain in their compact state. These data indicate that the pericentric chromatin spring approaches its full extent in the absence of pericentric cohesin or condensin, and behaves as a worm-like chain upon reduction of outward force (Figure 1.6).

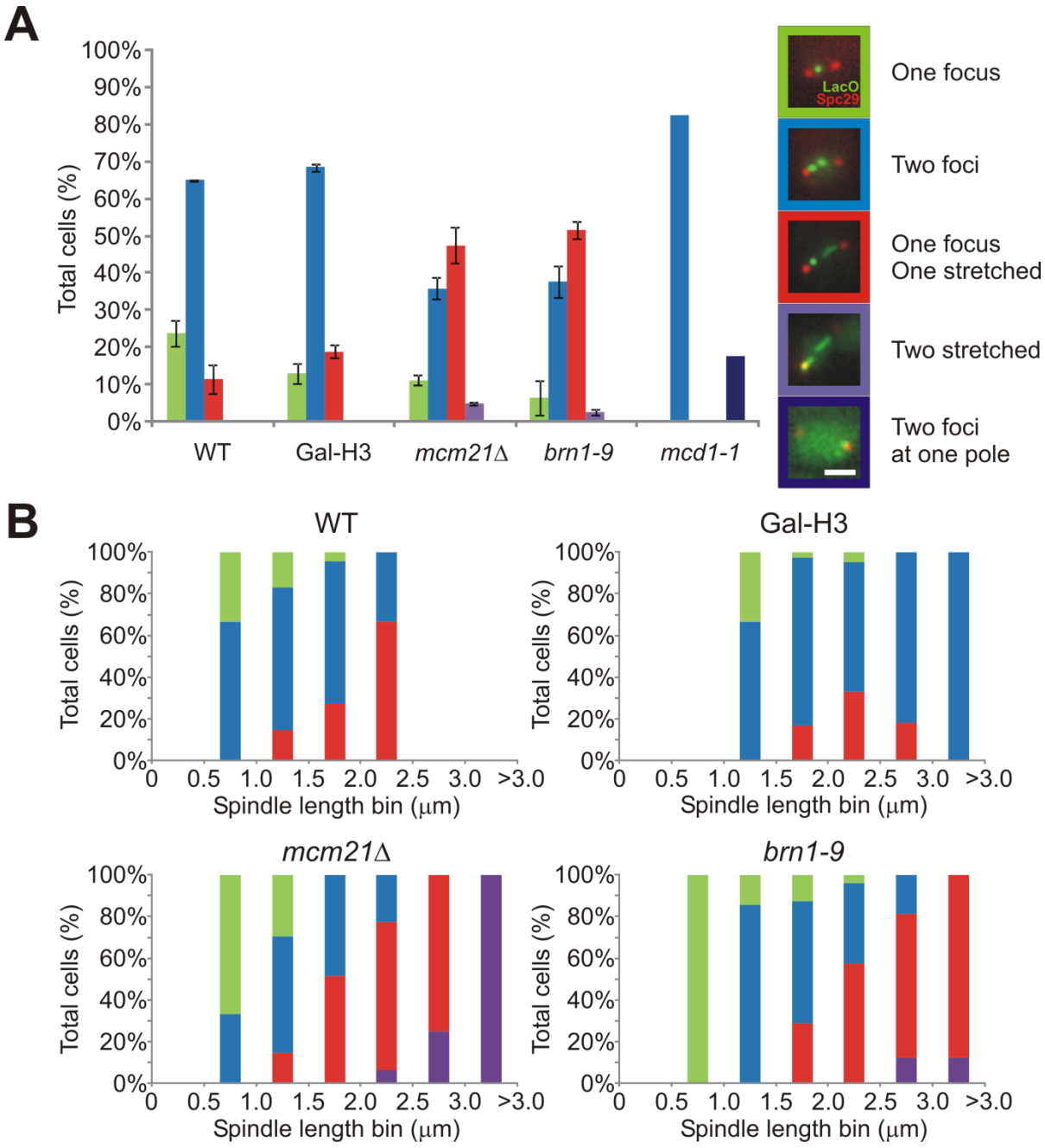
A
100%
90%
80%
70%
60%
50%
40%
30%
20%
10%
0%
Total cells (%)
WT
Gal-H3
mcm21Δ
brn1-9
mcd1-1
LacO
Spc29
One focus
Two foci
One focus
One stretched
Two stretched
Two foci
at one pole
B
WT
Gal-H3
mcm21Δ
brn1-9
Total cells (%)
0 0.5 1.0 1.5 2.0 2.5 3.0 >3.0
Spindle length bin (μm)

Figure 1.7 Increased stretching of pericentric chromatin LacO spots in pericentric cohesin and condensin mutants

(A) Pericentric LacO 6.8 kb from CEN 15 images were classified as one focus, two foci, one focus and one stretched, two stretched and two foci at one pole. The percentages of cells displaying each class of LacO fluorescence for each strain background is graphed with representative images of each class to the right. (WT: 24 ± 4% single focus, 65 ± 0% two foci, 11 ± 4% one stretched, 3 experiments *n* =167; Gal-H3: 13 ± 3% single focus, 68 ± 1% two foci, 19 ± 2% one stretched, 2 experiments *n* = 89; *mcm21Δ*: 11 ± 1 single focus, 36 ± 3% two foci, 47 ± 5% one stretched, 5 ± 0% two stretched, experiments *n* = 106; *brn1-9*: 6 ± 5% single focus, 38 ± 2% two foci, 52 ± 2% one stretched, 3 ± 1% two stretched, 2 experiments *n* = 83; *mcd1-1*: 82% two foci, 18% two foci at one pole, 1 experiment *n* = 17; scale bar = 2 μm). Error bars represent standard deviation. (B) The percentage of total cells compiled from all experiments displaying each class of LacO fluorescence is binned by spindle length into bins of 0.5 μm and graphed for WT, Gal-H3, *mcm21Δ*, and *brn1-9*.

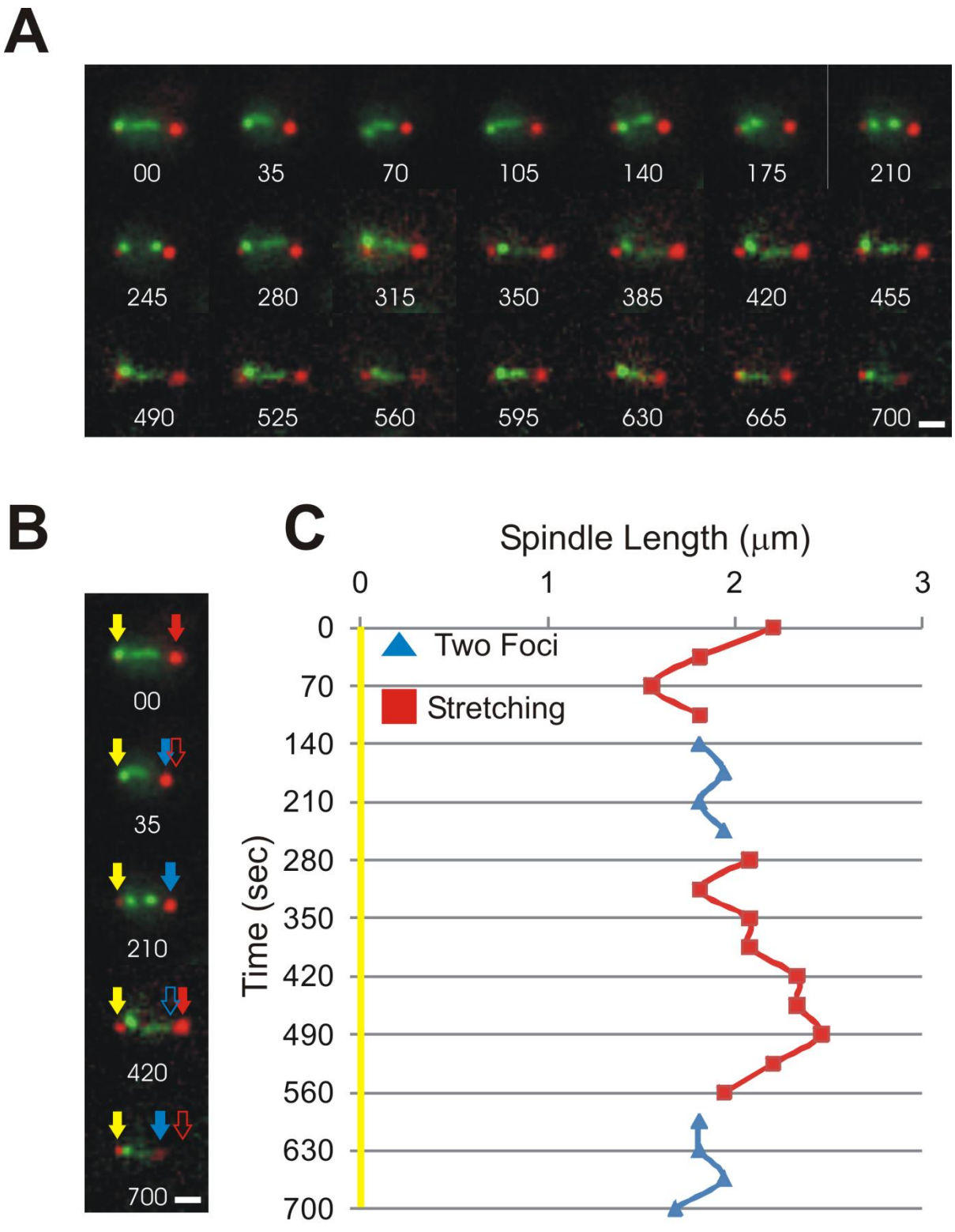
A
00
35
70
105
140
175
210
245
280
315
350
385
420
455
490
525
560
595
630
665
700
B
00
35
210
420
700
C
Spindle Length (μm)
0
1
2
3
Two Foci
Stretching
Time (sec)
0
70
140
210
280
350
420
490
560
630
700

Figure 1.8 Dynamics of pericentric 6.8 kb LacO stretching correlate with spindle length changes

(A) Time-lapse microscopy of spindle pole marker Spc29-RFP (red) and sister pericentric 6.8 kb LacO arrays (green) in a *mcm21Δ* spindle. Images were taken every 35 seconds for 700 seconds. The time-lapse shows stretching (line signal) and compaction (foci) of the right LacO array over time. (B) Selected frames of the movie tracking changes in spindle length when the right sister LacO is stretched or a focus. The left spindle pole is fixed (yellow arrow) and the right spindle pole body is highlighted by a solid red arrow when the LacO is stretching and a solid blue arrow when the LacO is a focus. The relative position change of the spindle pole when the LacO switches from stretching to focus, or vice-versa, is marked by a hollow arrow to denote its previous position. (C) Graph of spindle length over the time course of the movie. Each time point is classified as the LacO arrays being two foci (blue triangles) or stretching of the right sister LacO array (red squares). Scale bars in A and B = 1 μm.

Contribution of histone, cohesin and condensin to the organization of pericentric chromatin

To determine how cohesin and condensin contribute to the organization of the pericentric chromatin, we mapped the distribution of pericentric LacO arrays in wild-type cells. LacO arrays were inserted at 1.1, 1.8 and 3.8 kb from the centromere. The centroid of the LacO array in these strains is 1.7, 6.8 and 8.8 kb from the centromere respectively (see Materials and methods). Spatial probability maps were generated by taking the peak intensity of LacI-GFP bound to the LacO array and plotting the position relative to the spindle pole body (Spc29-RFP). The Cartesian coordinates (x, y) from multiple cells (1.7 kb n = 39; 6.8 kb n = 81; 8.8 kb n = 76) were used to generate a heat map that represents the distribution of the pericentric LacO relative to the spindle pole (Figure 1.9 A). Since the rotation of the spindle is random in individual cells, the Cartesian quadrant we obtain is actually one slice of the cylindrical arrangement of pericentric chromatin around the spindle. To illustrate the three-dimensional geometry, we mirrored the heat map about the spindle axis as it would be viewed from a single plane through the middle of the spindle (Figure 1.9 A).

LacO arrays 1.7 kb from the centromere exhibit a distribution 285 ± 124 nm in diameter and 355 ± 69 nm from the spindle pole (n = 39, Figure 1.9 A, Table 1.1). The distance from the spindle pole body is consistent with the estimated length of kinetochore microtubules (350 nm) obtained from tomography and model convolution microscopy (Winey et al., 1995; Gardner et al., 2005). LacO arrays 6.8 kb from the centromere reside 250 ± 172 nm in diameter and 405 ± 136 nm from the spindle pole (n = 81, Figure 1.9 A). LacO arrays at 8.8 kb from the centromere reside 326 ± 220 nm in diameter and 432 ± 175 nm from the spindle pole (n = 76, Figure 1.9 A, Table 1.1). 95% of all wild-type LacO arrays fall within a diameter 520 nm around the spindle axis. The distance of the centroid of the LacO

array in base pairs from the centromere vs. average distance from the spindle pole is an estimate of the packing ratio (Figure 1.9 D). The pericentric DNA (1.7 - 8.8 kb) is compacted an average of 107 bp/nm (Figure 1.9, D black line), or fivefold greater than a nucleosome fiber (21 bp/nm).

If the LacO stretching is a mechanical response to increased force, then the chromatin fiber would be expected to stretch along the spindle axis. Mapping the probability distribution of stretched wild-type 6.8 kb LacO revealed that stretched pericentric chromatin lies closer to the spindle axis 165 ± 115 nm and further from the spindle pole body 544 ± 262 nm (*n* = 87, Figure 1.9 B, Table 1.1). Interestingly, the average distance of the stretched 6.8 kb array relative to the position of the 1.7 kb array reveals that the packing ratio decreased from 107 to 27 bp/nm (Figure 1.9 D, gray line). This is comparable to nucleosome chromatin compaction. The stretching events observed in wild-type cells confirm that force along the spindle axis is mechanically opposed by cohesin and condensin, and that stretched chromatin is a linearly extended nucleosome fiber.

Histone repression (Gal-H3) and loss of condensin (*brn1-9*) resulted in a significant increase in the average distance of the 6.8 kb LacO foci from the spindle pole, 405 nm (WT) to 445 ± 186 nm (*n* = 95) and 455 ± 185 nm (*n* = 72, Figure 1.9 C and Table 1.1). This increase in length corresponds to a twofold decompaction compared to wild-type (53 bp/nm vs. 107 bp/nm WT). This value is similar to the twofold compaction observed upon cell cycle progression from G1 to M phase (Guacci et al., 1994). The Gal-H3 6.8 kb LacO probability distribution map becomes broader as well (Figure 1.9 C). Loss of pericentric cohesin

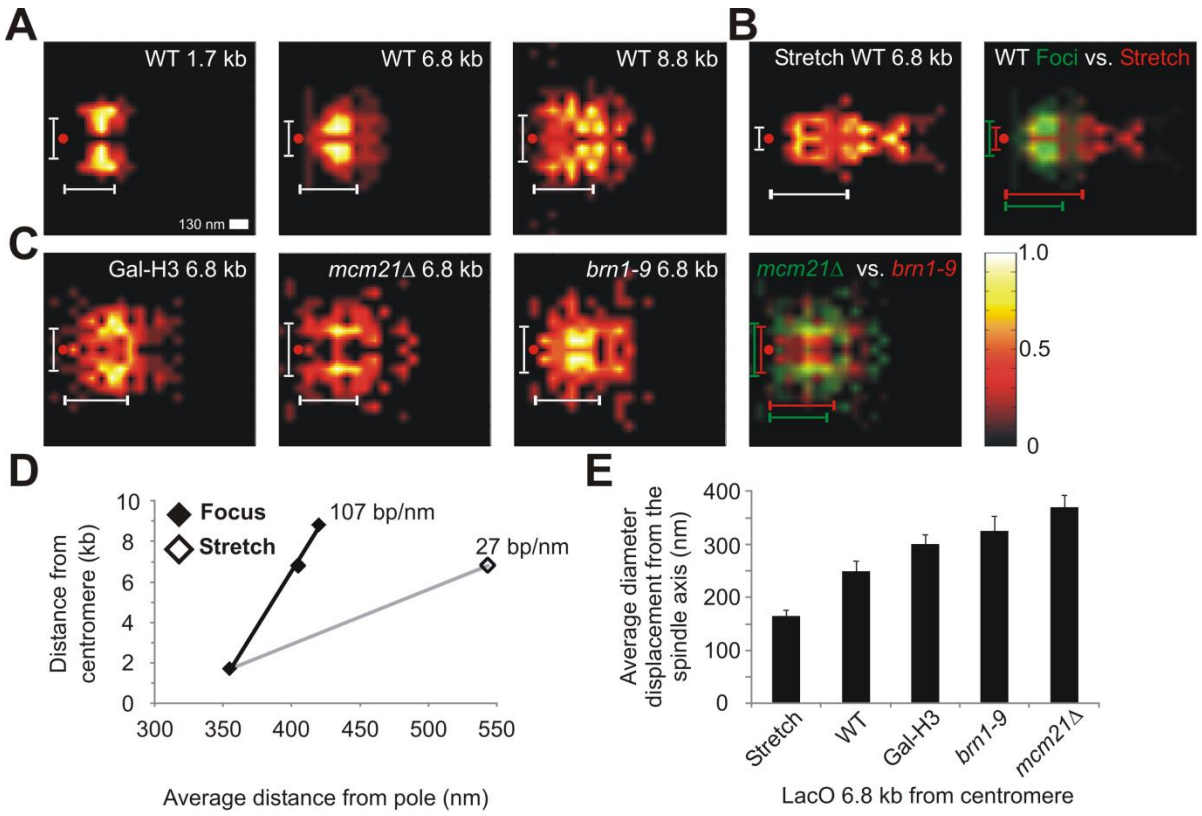
A
WT 1.7 kb
130 nm
WT 6.8 kb
WT 8.8 kb
B
Stretch WT 6.8 kb
WT Foci vs. Stretch
C
Gal-H3 6.8 kb
mcm21Δ 6.8 kb
brn1-9 6.8 kb
mcm21Δ vs. brn1-9
1.0
0.5
0
D
Focus
Stretch
107 bp/nm
27 bp/nm
Distance from centromere (kb)
Average distance from pole (nm)
E
Average diameter displacement from the spindle axis (nm)
Stretch
WT
Gal-H3
brn1-9
mcm21Δ
LacO 6.8 kb from centromere

Figure 1.9 Density maps of pericentric LacO show differences in the position probability

(A) The average position of wild-type pericentric LacO 1.7 kb from CEN 3, LacO 6.8 kb from CEN 15, and 8.8kb from CEN 3 was determined in metaphase spindles by mapping the peak intensity of the LacO relative to the spindle pole body (red circle). The number and position of peak LacO intensity was used to generate a color coded heat map of pericentric chromatin position in the spindle. (B) Position probability of wild-type pericentric LacO 6.8 kb displaying a stretched line signal. An overlay of WT foci 6.8 kb (green) and WT 6.8 kb stretching (red) heat maps allows for comparison. (C) Position probability of pericentric LacO 6.8 kb is altered distinctly in Gal-H3, *mcm21Δ*, and *brn1-9*. An overlay of *mcm21Δ* (green) and *brn1-9* (red) heat maps allows for comparison. (A, B, C) Vertical white lines represent average diameter and horizontal white lines represent the average distance from the spindle pole (values in Table 1.1). (D) Graph of LacO distance from centromere in base pairs vs. distance from pole in nanometers wild-type LacO 1.7, 6.8 and 8.8 kb (♦ black line) and wild-type stretched 6.8 kb (◊ gray line). (E) Bar graph of average diameter displacement perpendicular to the spindle axis for the LacO array 6.8 kb from the centromere in stretched, wild-type, Gal-H3, *brn1-9*, and *mcm21Δ*. Error bars represent SEM.

Table 1.1 Average position of CEN proximal LacO spots in wild-type and mutants

Strain		Distance from spindle pole (nm)		Diameter around spindle axis (nm)		Percent proximal
	n	Average	SD	Average	SD	
Wild-type 1.7 kb	39	355	69	285	124	20 %
Wild-type 6.8 kb	81	405	136	250	172	45 %
WT stretch 6.8 kb	87	544	262	165	115	62 %
Wild-type 8.8 kb	76	420	175	326	220	34 %
Gal-H3 6.8 kb	95	445	186	300	177	30 %
mcm21Δ 6.8 kb	85	408	227	370	218	18 %
brn1-9 6.8 kb	72	455	185	325	237	39 %

Percent proximal = LacO centroids fall within a 130 nm diameter around the spindle axis
.

(*mcm21Δ*) did not alter average distance of the 6.8 kb LacO foci from the spindle pole (408 ± 227 nm, n = 85). In contrast, the average diameter of the pericentric chromatin that encircles the spindle increased from 250 nm (WT) to 370 ± 218 nm (*mcm21Δ* Figure 1.9, C and E, and Table 1.1). In addition, there was a decrease in the distribution of LacO spots proximal to the spindle axis (Figure 1.9 C and Table 1.1). Histone and condensin compact the pericentric chromatin axially while cohesin contributes to radial compaction. These data are consistent with the location of condensin along the spindle axis vs. cohesin which is radially displaced. Therefore, the distribution of cohesin and condensin reflect their distinct functional roles in organizing the pericentric chromatin.

Discussion

The SMC-containing complexes, cohesin and condensin are responsible for chromosome pairing and condensation in mitosis. They are enriched in the pericentric region surrounding the centromere in metaphase and form a novel bipartite cylinder that encircles the spindle microtubules. This cylindrical arrangement of pericentric chromatin functions as a molecular spring that opposes the largely outward directed microtubule-based force.

The geometric arrangement of cohesin surrounding the spindle microtubules raises several questions. There are inconsistencies in the simple C-loop model (Figure 1.10 A; Yeh et al., 2008) with the distribution of cohesin based upon chromatin immunoprecipitation and the position of cohesin barrel (see Figure 1.1). Loops of 40-50 kb organized into a canonical nucleosomal beads-on-a-string extend ~1000-1200 nm from the chromosome axis (Figure 1.10 A). This length (1200 x 2 = ~2400 nm) is 3X the distance between kinetochore microtubules from each spindle pole (~800 nm). Secondly, if the DNA loops extend linearly

between kinetochore microtubule plus-ends, fluorescence from cohesin and condensin should overlap with the mitotic spindle. In contrast, cohesin and condensin are largely non-overlapping with cohesin radially displaced relative to the diameter of condensin and the kinetochores (Figure 1.1).

We have considered two alternative models that are consistent with both the localization of cohesin, condensin and the position of centromere-linked LacO arrays. One model is that 40-50 kb of pericentric chromatin is organized into a 30 nm fiber (Figure 1.10 B). Alternatively, the centromere DNA loop adopts a random coiled or branched conformation reminiscent of DNA loops observed in regions of very active transcription, such as the ribosomal DNA locus and mammalian kinetochores, reviewed in (Bloom and Joglekar, 2010; Figure 1.10 C). In both models thermal or active fluctuation of the fiber/loops could account for the observed radial displacement of DNA and cohesin. To estimate the packing ratio of pericentric chromatin, we mapped the position of centroids of LacO arrays at increasing distances from the centromere (Figure 1.9). We found that the pericentric chromatin 1.7 to 8.8 kb has a packing ratio of 107 bp/nm, equivalent to the predicted packing ratio of a 30 nm fiber (Finch and Klug, 1976; Tremethick, 2007). If the pericentric chromatin is organized into a 30 nm fiber, then loss of nucleosomes would have a disproportional contribution to spindle length since there would be a ~45 nm increase in length for each lost nucleosome (50 nm, b-form - 5 nm nucleosome). Since there is only a 50% increase in length observed upon histone repression, it is unlikely that 40-50 kb of 30 nm chromatin fiber contributes to spindle length regulation. Likewise, the packing of the 30 nm fiber would not be expected to depend upon cohesin and condensin, inconsistent with the increase in spindle length observed upon depletion of these complexes.

In the random or thermal loop model (Figure 1.10 C) cohesin and condensin contribute to spindle length via their function in condensing or bridging loops. Condensin has been hypothesized to compact chromatin into loops (Kimura and Hirano, 1997; Yoshimura et al., 2002; Strick et al., 2004; Hirano, 2006) while cohesin may function to stabilize or bridge neighboring loops that are displaced from the spindle axis. Cohesin's looping function has recently emerged from studies on transcriptional regulation at a distance (Mishiro et al., 2009; Nativio et al., 2009; Guillou et al., 2010; Hou et al., 2010; Kagey et al., 2010). The tendency of cohesin to be displaced from the spindle may reflect its mobility following loading (Lengronne et al., 2004; Glynn et al., 2004; Hu et al., 2011). Alternatively, condensin may aid in displacing cohesin from the core centromere as it does in *C. elegans* to facilitate centromere resolution (Moore et al., 2005). The spatial distributions and/or functional interdependency between the two complexes may contribute to their similar effects on spindle length (Guacci et al., 1997; Lavoie et al., 2002; Lavoie et al., 2004; Lam et al., 2006; Heidinger-Pauli et al., 2010).

There are several different mechanisms in which the DNA and/or SMC complexes may contribute to the chromatin spring. One, condensin and/or cohesin are protein springs and DNA provides a mechanism to link multiple condensins/cohesins in series (protein spring, Figure 1.10 C i). Upon depletion of pericentric cohesin or condensin, there is a loss of chromatin elasticity as evidenced by increased pericentric LacO extension and spindle length variation. HEAT repeats that are present in the auxiliary subunits of SMC protein complexes (Panizza et al., 2000; Neuwald and Hirano, 2000) have been shown to be elastic elements that link force to catalysis in protein phosphatase PP2A (Grinthal et al., 2010). Second, the DNA worm-like chain (WLC) constitutes the spring (DNA spring, Figure 1.10 C ii). The

worm-like chain is a non-linear entropic spring that reflects the tendency of a long-chain polymer to adopt a random coil. It takes very low force to significantly extend the random coil since the applied force is working against entropy. When the chain reaches about 90% of its overall length (contour length) the force extension curve increases exponentially as the applied force works against covalent bonds. In a WLC mechanism, we propose that nucleosome depletion results in an increase in overall spring length. The spring remains in the linear region of the WLC curve (Figure 1.6) and chromatin recoils upon deletion of *KIP1*. Depletion of pericentric cohesin or condensin results in full extension of the WLC (pericentric LacO stretching Figure 1.7). In this realm of the force extension curve, changes in force have little effect on length (Figure 1.6), consistent with the lack of recoil upon deletion of *KIP1*. A third mechanism is that condensin/cohesin protein springs limit the length of DNA under tension thereby increasing the entropic DNA spring constant (axial DNA/protein spring, Figure 1.10 C iii). The spring constant of a polymer like DNA is inversely proportional to its chain length (Grosberg and Khokhlov, 1997), thus restricting the length of DNA axially will increase spring constant. The pericentric chromatin spring consists of elastic proteins as well as a long chain DNA polymer. The spring exhibits properties of a Hookean spring or a worm-like chain depending on the geometry and composition of proteins, and the percent extension and/or overall length of the entropic DNA spring.

Spindle length fluctuation is a read-out of the stiffness of the chromatin spring. By mutation of one component, we can estimate a minimal spring constant from thermal fluctuations. Thermal fluctuations acting on an object are given by the equipartition theorem, $\sigma^2 = k_BT / k$, (σ^2 = variation^2; k_BT = Boltzmann's constant, 4 pN·nm; k = spring constant).

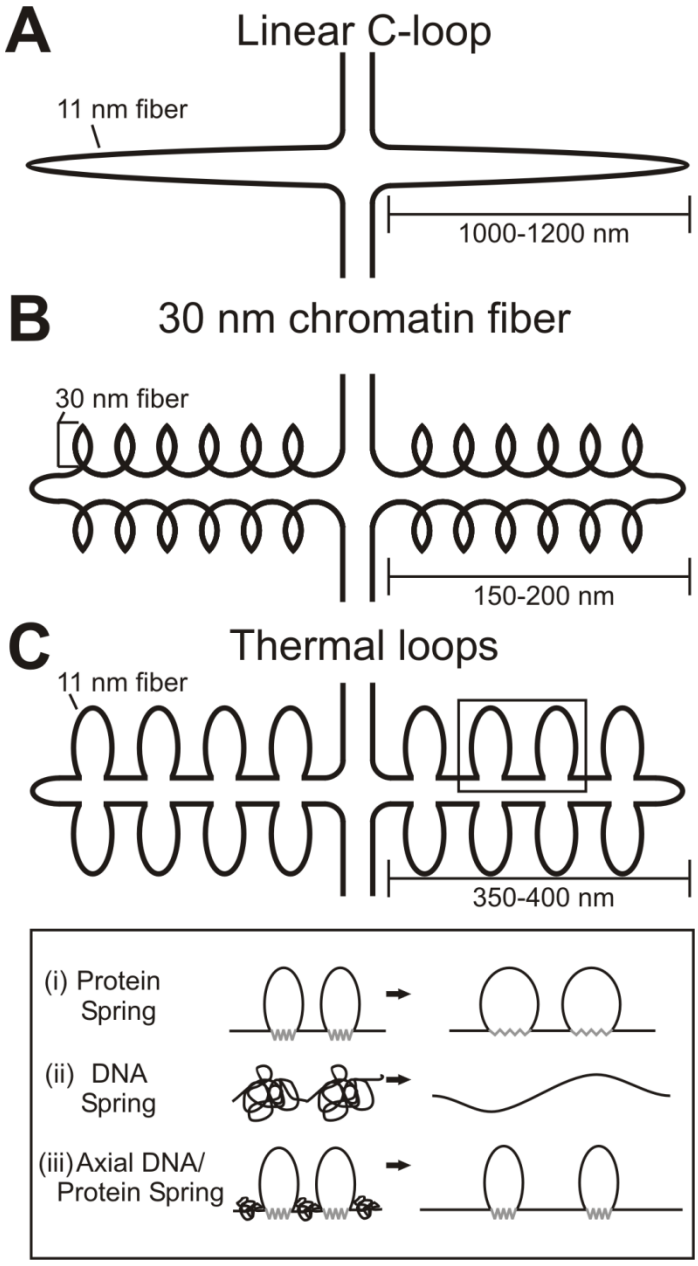
A
Linear C-loop
11 nm fiber
1000-1200 nm
B
30 nm chromatin fiber
30 nm fiber
150-200 nm
C
Thermal loops
11 nm fiber
350-400 nm
(i) Protein Spring
(ii) DNA Spring
(iii) Axial DNA/ Protein Spring

Figure 1.10 Models of the pericentric chromatin spring

The pericentric chromatin (40-50 kb) is modeled as a (A) linear loop, (B) 30 nm chromatin fiber or (C) a network of thermally fluctuating loops, denoted as thermal loops. The inset details three spring models. (i) Protein spring – cohesin and/or condensin (gray), linked via DNA are the elastic elements. (ii) DNA spring – the DNA worm-like chain adopts a random coil that expands and contracts in response to force. (iii) Axial DNA/protein spring – Protein springs limit the amount of DNA under tension, which in turn increases the spring constant. Elastic proteins and the DNA worm-like chain expand and contract in response to force.

.

Since other parameters are held constant (i.e. cells differ only in the mutation of interest), the equipartition theorem allows us to convert spindle length variation into an estimated spring constant. The spring constant was calculated using k_BT at 300 Kelvin divided by the experimentally measured spindle length variation squared (σ^2). The wild-type spring constant was calculated to be 0.345 pN/μm ($k = 4.1$ pN·nm /$(109\text{ nm})^2$). Repression of nucleosomes increased spindle length, but did not significantly alter spindle variation or spring constant (0.372 pN/μm Gal-H3 vs. 0.345 pN/μm WT). Therefore, histones dictate the rest or contour length of the chromatin spring rather than the spring constant. Interestingly, this calculated spring constant is comparable to the estimated force the anaphase spindle exerts on a single DNA molecule in living cells (0.2-0.42 pN/μm; Fisher et al., 2009).

Upon depletion of pericentric cohesin or condensin, the spring constant decreased to 25% that of wild-type (0.095 pN/μm *mcm21Δ*, 0.087 pN/μm *brn1-9*). Thus, pericentric cohesin and condensin contribute to the spring constant of pericentric chromatin (intramolecular spring). Loss of pericentric and arm cohesin in *mcd1-1* mutants at restrictive temperature decreased the spring constant to 6% (0.021 pN/μm) of wild-type, indicating arm cohesion (intermolecular spring) contributes to the chromatin spring constant as well.

These data provide the first structural basis for chromatin springs in the spindle. The DNA packaging function of histones is translated into the spring length rather than spring constant. Condensin is concentrated along the spindle axis and contributes to the chromatin spring by resisting the outward force of the spindle. Cohesin contributes to the chromatin spring from a distal position. In addition, cohesin functions to confine and compress the pericentric chromatin to a position along the spindle axis. Human cells that are pRB-depleted have decreased levels of pericentric cohesin and condensin and an increased pericentric

chromatin length (Manning et al., 2010). The loss of checkpoint tension sensing reported in yeast pericentric cohesin, *mcm21Δ* (Ng et al., 2009), and condensin mutants (Yong-Gonzalez et al., 2007) underscores the importance of the chromatin spring. Mammalian cells depleted of condensin also show a decreased ability to properly sense tension at the kinetochore (Samoshkin et al., 2009; Uchida et al., 2009; Ribeiro et al., 2009). We propose that cohesin and condensin contribute to the structure and function of the pericentric chromatin spring that is conserved from yeast to higher eukaryotes to facilitate the faithful segregation of the genome in mitosis.

Materials and methods

Cell Preparation and Imaging

Cells were incubated in YPD (2% glucose, 2% peptone, and 1% yeast extract) at 32°C for wild-type strains. Temperature-sensitive strains containing *mcd1-1*, *brn1-9*, and *smc4-1* were grown at 24°C. Temperature-sensitive strains were grown into early log phase at 24°C then shifted to restrictive temperature at 37°C for three hours before filming. Temperature-sensitive stains were then viewed at room temperature for no longer than 45 minutes. Gal-H3 strains were alpha factor arrested in YPG (2% galactose), washed and then released into YPD (2 % glucose) for 3-4 hours before viewing, as outlined in (Bouck and Bloom, 2007). Gal-CDC20 strains were grown into logarithmic phase in YPG, washed and then grown in YPD for 3 hours before imaging. Dicentric strains were grown in YPG to maintain a monocentric chromosome III to logarithmic phase, washed and then grown in YPD to activate the dicentric for 1 – 2 hours before imaging as outlined in (Yang et al., 1997).

Wide field microscope images were acquired at room temperature (25°C) using a Nikon Eclipse TE2000-U (Nikon, East Rutherford, NJ, USA) microscope stand with a 100X Plan Apo 1.4 NA digital interference contrast (DIC) oil emersion lens with a Orca ER Camera (Hamamatsu Photonics K.K., Hamamatsu City, Japan). MetaMorph 6.1 (Molecular Devices, Downington, PA, USA) was used to acquire un-binned z-series image stacks with z-step size of 300 nm. Imaging of Smc3/Smc4-GFP was carried out in water on ConA coated cover slips. Live-imaging of cells was carried out on 25% gelatin slab with yeast complete (YC) 2% glucose media. Image exposure times were between 300-700 ms.

Analyzing Smc3 and Smc4 fluorescence

MATLAB (The Mathworks, Inc., Natick, MA, USA) was used to rotate the spindle axis of MetaMorph images horizontally using Spc29-RFP as markers of spindle ends. Horizontally rotated images could then be analyzed in MetaMorph with both spindle pole bodies brightest pixel along the same y coordinates. Line scans one pixel in width and the length of the spindle were drawn along the spindle axis of images containing Smc4-GFP and Spc29-RFP in MetaMorph. Data of pixel position and intensity of Smc4-GFP were transferred to Excel (Microsoft Corporation, Redmond, WA, USA) and graphed to determine the classification (one focus, two foci, or uniform signal) of condensin enrichment between spindle poles.

Only single plane images from z-series acquisitions containing both Spc29-RFP spindle pole bodies in focus with metaphase length spindles 1.3-1.7 μm were used for analyzing Smc3, Smc4, or Nuf2-GFP. Each single plane image was rotated using MATLAB to align all spindles axis horizontally along the same y coordinate. Using MetaMorph, line scans of each single plane image were taken perpendicular and parallel to the spindle axis

and through the maximum pixel intensity. These line scans were averaged and graphed using Excel to show the average distribution of both Smc3 and Smc4 perpendicular (width/diameter around the spindle axis) and parallel (length along the spindle axis) to the spindle axis. Smc3 width was measured by the inclusive pixel coordinates from peak-to-peak of the bi-lobed enrichment. Smc4 and Nuf2 width was measured in MATLAB by fitting a Gaussian distribution to the line scan through the brightest pixel to obtain a full-width half-maximum measurement. Lengths of Smc3 and Smc4 enrichment were measured along the x axis by using the distance between pixel coordinates at half-maximum above nuclear background using MetaMorph.

Average distribution pictures were generated using already rotated images of cohesin, condensin, or kinetochore proteins with spindle poles. Rotated images were then color combined, Spc29-RFP and Smc3/4-GFP of Nuf2-GFP, in MetaMorph and saved. The color combined stacks were separated into single plane color combined sequential images by ImageJ. The sequential series of single plane color combined pictures were loaded into Video Optimizer (CISMM UNC-Chapel Hill; http://cismm.cs.unc.edu/downloads) to be scaled to the average spindle length and generated an average Smc3, Smc4, and Nuf2 GFP fluorescence signal between spindle pole bodies.

Spindle length and variation

Spindle lengths were measured by logging the coordinates of the brightest pixel of each spindle pole body, marked by Spc29-RFP, using MetaMorph. Coordinates of pixel position were measured in triplicate. The coordinates of sister spindle poles were transferred to Excel and converted into μm distance spindle length. Spindle lengths were measured in two dimensions and three dimensions using the Pythagorean Theorem. Time-lapse movies

were carried out on single cells using Acquire Time-lapse in MetaMorph to take a z-series every 35 seconds for 20 time points, equaling 11 2/3 minutes. Change in spindle length, denoted as variation, was calculated by the absolute value of the difference between spindle length at each time point and the mean spindle length of the time-lapse. All metaphase spindle lengths and time-lapses were taken in spindles at least 1.1 μm, with separated Nuf2 kinetochore foci and spindles not exhibiting linearly increasing anaphase spindle behavior.

Analyzing pericentric LacO array stretching and position

LacO/lacI-GFP strains were grown in SD-His media to induce LacI-GFP under the *HIS* promoter as outlined by (Goshima and Yanagida, 2000; Pearson et al., 2001). LacO array strains were KBY 8088 1.7 kb centroid from CEN 3 (1.2 kb array inserted at 1.1 kb from CEN 3), KBY 8065 LacO 6.8 kb centroid from CEN 15 (10 kb array inserted at 1.8 kb from CEN 15), KBY 8087 8.8 kb centroid from CEN 3 (10 kb array inserted at 3.8 kb from CEN 3). Images were captured using un-binned and 2X2 binning acquisitions and were analyzed in MetaMorph using line scans to determine focus vs. stretching LacO spots. Focus LacO spots were determined by a Gaussian distribution line scan through the brightest pixel. Stretched LacO was determined by a non-Gaussian distribution or broadening of the line scan with ~1/2 decrease in brightest pixel fluorescence signal compared to a focus.

Two-dimensional density maps were generated of LacO/lacI-GFP spots relative to the spindle pole body (Spc29-RFP) as outlined in (Anderson et al., 2009). Single plane images were rotated using MATLAB to align all spindles' axis horizontally along the same y coordinate. The distance in pixels from each LacO/LacI-GFP brightest pixel to its respective spindle pole body brightest pixel was recorded in Excel. The frequency of a LacO position relative to the spindle pole was compiled for a single quadrant of the spindle and then

mirrored about the spindle axis. The frequency of LacO position relative to the spindle pole was transferred to MATLAB to generate a two-dimensional probability map using black body radiation spectrum (black represents zero probability, red and orange represents low probability, yellow and white represent high probability). Heat maps were interpolated twice using this MATLAB code. The distance in pixels from the spindle pole body to the LacO in the x and y planes for each LacO was averaged to yield a distance from the spindle pole (x) and radial displacement from the spindle axis (y).

Strains

KBY 8088 MATa ade1, met14, ura3-52, leu2-3,112 his3-11,15 lys2Δ::lacI-GFP-NLS-NAT, 1.1kbCEN3::LacO-KAN(1.2kb array), Spc29RFP:Hb

KBY 8065 MATa ade2-1, his3-11, trp1-1, ura3-1, leu2-3,112 can1-100 LacINLSGFP:HIS3, LacO::URA3(1.8kb from CEN15, 10kb array) Spc29RFP:Hb

KBY 8087 MATa ade2-1, his3-11, trp1-1, ura3-1, leu2-3,112 can1-100 LacINLSGFP:HIS3, LacO::URA3(3.8kb from CEN15, 10kb array), Spc29CFP:Hb

KBY 8062 MATa ade2-1, his3-11, trp1-1, ura3-1, leu2-3,112 can1-100 LacINLSGFP:HIS3, LacO::URA3(1.8kb from CEN15, 10kb array) Spc29RFP:Hb, HHT1::TRP, KAN-GAL-HHT2

KBY 9039 MATa ade2-1, his3-11, trp1-1, ura3-1, leu2-3,112 can1-100 LacINLSGFP:HIS3, LacO::URA3(1.8kb from CEN15, 10kb array) Spc29RFP:Hb, *brn1-9*-Nat

KBY 9040 MATa ade2-1, his3-11, trp1-1, ura3-1, leu2-3,112 can1-100 LacINLSGFP:HIS3, LacO::URA3(1.8kb from CEN15, 10kb array) Spc29RFP:Hb, *mcd1-1*

KBY 9059 MATa ade2-1, his3-11, trp1-1, ura3-1, leu2-3,112 can1-100 LacINLSGFP:HIS3, LacO::URA3(1.8kb from CEN15, 10kb array) Spc29RFP:Hb, *mcm21Δ*::Nat

KBY 407 *mcd1-1*, MATalpha, ade5-1, trp1-289, ura3del, leu2-3, 112, lys2::insI-Sce1 (LacO array next to RAD16 promoter, tetO array next to LYS2 promoter (pRS305tetO), arg4::hisG Gal1/10 I-Sce1, thr1::HISpLacI-GFP:Nat, ade1::URAptetR-CFP:Hyg, Spc29-RFP:Bsd, Nuf2-GFP-URA

YSB 9025 (alpha) *smc4-1*, *ade2*, *ade3Δ*, *his3*, *leu2*, *trp-1*, Spc29-RFP:Hb, Nuf2-GFP-URA (Bachellier-Bassi lab)

YEF473 *MATa trp1-63 leu2Δ1 ura3-52*, *his2-200*, *lys 2-801* (Pringle lab)

MAY 8526 (YEF473A) Nuf2-GFP:Kan, Spc29-RFP-Hb

DCB 204 (YEF473A) HHT1::TRP1, KAN-GALp-HHT2, SPC29-RFP-Hb, NUF2-GFP-URA

KBY 9053 (YEF473A) *brn1-9*-NAT, Spc29-RFP-Hb, Nuf2-GFP-URA

KBY 9070 (YEF 473A) *mcm21*::Nat, Spc29-RFP-Hb, Nuf2-GFP-URA

WLY 8912 (YEF 473A) pLF639 (URA3 Smc3-GFP), Spc29-RFP-Hb

KBY 9035 (YEF 473A) Smc4-GFP-Kan, Spc29-RFP-Hb

KBY 9131 (YEF 473A)) *brn1-9*-NAT, Spc29-RFP-Hb, Nuf2-GFP-URA, *kip1Δ*::HIS3

KBY 9122 (YEF 473A) *mcm21*::Nat, Spc29-RFP-Hb, Nuf2-GFP-URA, *kip1Δ*::HIS3

KBY 9117 (YEF 473A) *mcd1-1*, Spc29-RFP-Hb, Nuf2-GFP-URA, *kip1Δ*::HIS3

KBY 9357 (YEF 473A) pJB2#4 Spc29-RFP-Hb

KBY 9169 (YEF 473A) gal2::HIS3, pGALS-CDC20-Nat, Spc29-RFP-Hb

Plasmids

pSO1 brn1-9-NAT (Lavoie lab)

pLF639 (URA3 Smc3-GFP) (Strunnikov lab)

References

Almagro, S., D. Riveline, T. Hirano, B. Houchmandzadeh, and S. Dimitrov. 2004. The mitotic chromosome is an assembly of rigid elastic axes organized by structural maintenance of chromosomes (SMC) proteins and surrounded by a soft chromatin envelope. *J Biol Chem*. 279:5118-26.

Anderson, M., J. Haase, E. Yeh, and K. Bloom. 2009. Function and assembly of DNA looping, clustering, and microtubule attachment complexes within a eukaryotic kinetochore. *Mol Biol Cell*. 20:4131-9.

Bachant, J., A. Alcasabas, Y. Blat, N. Kleckner, and S.J. Elledge. 2002. The SUMO-1 isopeptidase Smt4 is linked to centromeric cohesion through SUMO-1 modification of DNA topoisomerase II. *Mol Cell*. 9:1169-82.

Bachellier-Bassi, S., O. Gadal, G. Bourout, and U. Nehrbass. 2008. Cell cycle-dependent kinetochore localization of condensin complex in Saccharomyces cerevisiae. *J Struct Biol*. 162:248-59.

Bloom, K., and A. Joglekar. 2010. Towards building a chromosome segregation machine. *Nature*. 463:446-56.

Bouck, D.C., and K. Bloom. 2007. Pericentric chromatin is an elastic component of the mitotic spindle. *Curr Biol*. 17:741-8.

Bouck, D.C., A.P. Joglekar, and K.S. Bloom. 2008. Design features of a mitotic spindle: balancing tension and compression at a single microtubule kinetochore interface in budding yeast. *Annu Rev Genet*. 42:335-59.

Bustamante, C., J.F. Marko, E.D. Siggia, and S. Smith. 1994. Entropic elasticity of lambda-phage DNA. *Science*. 265:1599-600.

Cheeseman, I.M., and A. Desai. 2008. Molecular architecture of the kinetochore-microtubule interface. *Nat Rev Mol Cell Biol*. 9:33-46.

D'Ambrosio, C., C.K. Schmidt, Y. Katou, G. Kelly, T. Itoh, K. Shirahige, and F. Uhlmann. 2008. Identification of cis-acting sites for condensin loading onto budding yeast chromosomes. *Genes Dev*. 22:2215-27.

Eckert, C.A., D.J. Gravdahl, and P.C. Megee. 2007. The enhancement of pericentromeric cohesin association by conserved kinetochore components promotes high-fidelity chromosome segregation and is sensitive to microtubule-based tension. *Genes Dev*. 21:278-91.

Finch, J.T., and A. Klug. 1976. Solenoidal model for superstructure in chromatin. *Proc Natl Acad Sci U S A*. 73:1897-901.

Fisher, J.K., M. Ballenger, E.T. O'Brien, J. Haase, R. Superfine, and K. Bloom. 2009. DNA relaxation dynamics as a probe for the intracellular environment. *Proc Natl Acad Sci U S A*. 106:9250-5.

Fitzgerald-Hayes, M., L. Clarke, and J. Carbon. 1982. Nucleotide sequence comparisons and functional analysis of yeast centromere DNAs. *Cell*. 29:235-44.

Gardner, M.K., J. Haase, K. Mythreye, J.N. Molk, M. Anderson, A.P. Joglekar, E.T. O'Toole, M. Winey, E.D. Salmon, D.J. Odde, and K. Bloom. 2008. The microtubule-based motor Kar3 and plus end-binding protein Bim1 provide structural support for the anaphase spindle. *J Cell Biol*. 180:91-100.

Gardner, M.K., C.G. Pearson, B.L. Sprague, T.R. Zarzar, K. Bloom, E.D. Salmon, and D.J. Odde. 2005. Tension-dependent regulation of microtubule dynamics at kinetochores can explain metaphase congression in yeast. *Mol Biol Cell*. 16:3764-75.

Glynn, E.F., P.C. Megee, H.G. Yu, C. Mistrot, E. Unal, D.E. Koshland, J.L. DeRisi, and J.L. Gerton. 2004. Genome-wide mapping of the cohesin complex in the yeast Saccharomyces cerevisiae. *PLoS Biol*. 2:E259.

Goshima, G., and M. Yanagida. 2000. Establishing biorientation occurs with precocious separation of the sister kinetochores, but not the arms, in the early spindle of budding yeast. *Cell*. 100:619-33.

Grinthal, A., I. Adamovic, B. Weiner, M. Karplus, and N. Kleckner. 2010. PR65, the HEAT-repeat scaffold of phosphatase PP2A, is an elastic connector that links force and catalysis. *Proc Natl Acad Sci U S A*. 107:2467-72.

Grosberg, A.Y., and A.R. Khokhlov. 1997. Giant Molecules Here, There, and Everywhere... Academic Press, INC., San Diego. 1-244 pp.

Guacci, V., E. Hogan, and D. Koshland. 1994. Chromosome condensation and sister chromatid pairing in budding yeast. *J Cell Biol*. 125:517-30.

Guacci, V., D. Koshland, and A. Strunnikov. 1997. A direct link between sister chromatid cohesion and chromosome condensation revealed through the analysis of MCD1 in S. cerevisiae. *Cell*. 91:47-57.

Guillou, E., A. Ibarra, V. Coulon, J. Casado-Vela, D. Rico, I. Casal, E. Schwob, A. Losada, and J. Mendez. 2010. Cohesin organizes chromatin loops at DNA replication factories. *Genes Dev*. 24:2812-22.

Hartwell, L.H., R.K. Mortimer, J. Culotti, and M. Culotti. 1973. Genetic Control of the Cell Division Cycle in Yeast: V. Genetic Analysis of cdc Mutants. *Genetics*. 74:267-86.

Heidinger-Pauli, J.M., O. Mert, C. Davenport, V. Guacci, and D. Koshland. 2010. Systematic reduction of cohesin differentially affects chromosome segregation, condensation, and DNA repair. *Curr Biol*. 20:957-63.

Hirano, T. 2006. At the heart of the chromosome: SMC proteins in action. *Nat Rev Mol Cell Biol*. 7:311-22.

Hou, C., R. Dale, and A. Dean. 2010. Cell type specificity of chromatin organization mediated by CTCF and cohesin. *Proc Natl Acad Sci U S A*. 107:3651-6.

Hu, B., T. Itoh, A. Mishra, Y. Katoh, K.L. Chan, W. Upcher, C. Godlee, M.B. Roig, K. Shirahige, and K. Nasmyth. 2011. ATP hydrolysis is required for relocating cohesin from sites occupied by its Scc2/4 loading complex. *Curr Biol*. 21:12-24.

Kagey, M.H., J.J. Newman, S. Bilodeau, Y. Zhan, D.A. Orlando, N.L. van Berkum, C.C. Ebmeier, J. Goossens, P.B. Rahl, S.S. Levine, D.J. Taatjes, J. Dekker, and R.A. Young. 2010. Mediator and cohesin connect gene expression and chromatin architecture. *Nature*. 467:430-5.

Kawamura, R., L.H. Pope, M.O. Christensen, M. Sun, K. Terekhova, F. Boege, C. Mielke, A.H. Andersen, and J.F. Marko. 2010. Mitotic chromosomes are constrained by topoisomerase II-sensitive DNA entanglements. *J Cell Biol*. 188:653-63.

Kimura, K., and T. Hirano. 1997. ATP-dependent positive supercoiling of DNA by 13S condensin: a biochemical implication for chromosome condensation. *Cell*. 90:625-34.

Lam, W.W., E.A. Peterson, M. Yeung, and B.D. Lavoie. 2006. Condensin is required for chromosome arm cohesion during mitosis. *Genes Dev*. 20:2973-84.

Lavoie, B.D., E. Hogan, and D. Koshland. 2002. In vivo dissection of the chromosome condensation machinery: reversibility of condensation distinguishes contributions of condensin and cohesin. *J Cell Biol*. 156:805-15.

Lavoie, B.D., E. Hogan, and D. Koshland. 2004. In vivo requirements for rDNA chromosome condensation reveal two cell-cycle-regulated pathways for mitotic chromosome folding. *Genes Dev*. 18:76-87.

Lavoie, B.D., K.M. Tuffo, S. Oh, D. Koshland, and C. Holm. 2000. Mitotic chromosome condensation requires Brn1p, the yeast homologue of Barren. *Mol Biol Cell*. 11:1293-304.

Lengronne, A., Y. Katou, S. Mori, S. Yokobayashi, G.P. Kelly, T. Itoh, Y. Watanabe, K. Shirahige, and F. Uhlmann. 2004. Cohesin relocation from sites of chromosomal loading to places of convergent transcription. *Nature*. 430:573-8.

Manning, A.L., M.S. Longworth, and N.J. Dyson. 2010. Loss of pRB causes centromere dysfunction and chromosomal instability. *Genes Dev*. 24:1364-76.

Megee, P.C., C. Mistrot, V. Guacci, and D. Koshland. 1999. The centromeric sister chromatid cohesion site directs Mcd1p binding to adjacent sequences. *Mol Cell*. 4:445-50.

Michaelis, C., R. Ciosk, and K. Nasmyth. 1997. Cohesins: chromosomal proteins that prevent premature separation of sister chromatids. *Cell*. 91:35-45.

Mishiro, T., K. Ishihara, S. Hino, S. Tsutsumi, H. Aburatani, K. Shirahige, Y. Kinoshita, and M. Nakao. 2009. Architectural roles of multiple chromatin insulators at the human apolipoprotein gene cluster. *EMBO J*. 28:1234-45.

Moore, L.L., G. Stanvitch, M.B. Roth, and D. Rosen. 2005. HCP-4/CENP-C promotes the prophase timing of centromere resolution by enabling the centromere association of HCP-6 in Caenorhabditis elegans. *Mol Cell Biol*. 25:2583-92.

Nasmyth, K., and C.H. Haering. 2009. Cohesin: its roles and mechanisms. *Annu Rev Genet*. 43:525-58.

Nativio, R., K.S. Wendt, Y. Ito, J.E. Huddleston, S. Uribe-Lewis, K. Woodfine, C. Krueger, W. Reik, J.M. Peters, and A. Murrell. 2009. Cohesin is required for higher-order chromatin conformation at the imprinted IGF2-H19 locus. *PLoS Genet*. 5:e1000739.

Neuwald, A.F., and T. Hirano. 2000. HEAT repeats associated with condensins, cohesins, and other complexes involved in chromosome-related functions. *Genome Res*. 10:1445-52.

Ng, T.M., W.G. Waples, B.D. Lavoie, and S. Biggins. 2009. Pericentromeric sister chromatid cohesion promotes kinetochore biorientation. *Mol Biol Cell*. 20:3818-27.

Panizza, S., T. Tanaka, A. Hochwagen, F. Eisenhaber, and K. Nasmyth. 2000. Pds5 cooperates with cohesin in maintaining sister chromatid cohesion. *Curr Biol*. 10:1557-64.

Pearson, C.G., P.S. Maddox, E.D. Salmon, and K. Bloom. 2001. Budding yeast chromosome structure and dynamics during mitosis. *J Cell Biol*. 152:1255-66.

Pearson, C.G., E. Yeh, M. Gardner, D. Odde, E.D. Salmon, and K. Bloom. 2004. Stable kinetochore-microtubule attachment constrains centromere positioning in metaphase. *Curr Biol*. 14:1962-7.

Peters, J.P., 3rd, and L.J. Maher. 2010. DNA curvature and flexibility in vitro and in vivo. *Q Rev Biophys*. 43:23-63.

Ribeiro, S.A., J.C. Gatlin, Y. Dong, A. Joglekar, L. Cameron, D.F. Hudson, C.J. Farr, B.F. McEwen, E.D. Salmon, W.C. Earnshaw, and P. Vagnarelli. 2009. Condensin regulates the stiffness of vertebrate centromeres. *Mol Biol Cell*. 20:2371-80.

Sakuno, T., K. Tada, and Y. Watanabe. 2009. Kinetochore geometry defined by cohesion within the centromere. *Nature*. 458:852-8.

Samoshkin, A., A. Arnaoutov, L.E. Jansen, I. Ouspenski, L. Dye, T. Karpova, J. McNally, M. Dasso, D.W. Cleveland, and A. Strunnikov. 2009. Human condensin function is essential for centromeric chromatin assembly and proper sister kinetochore orientation. *PLoS One*. 4:e6831.

Saunders, W.S., and M.A. Hoyt. 1992. Kinesin-related proteins required for structural integrity of the mitotic spindle. *Cell*. 70:451-8.

Straight, A.F., J.W. Sedat, and A.W. Murray. 1998. Time-lapse microscopy reveals unique roles for kinesins during anaphase in budding yeast. *J Cell Biol*. 143:687-94.

Strick, T.R., T. Kawaguchi, and T. Hirano. 2004. Real-time detection of single-molecule DNA compaction by condensin I. *Curr Biol*. 14:874-80.

Tanaka, T., M.P. Cosma, K. Wirth, and K. Nasmyth. 1999. Identification of cohesin association sites at centromeres and along chromosome arms. *Cell*. 98:847-58.

Tanaka, T., J. Fuchs, J. Loidl, and K. Nasmyth. 2000. Cohesin ensures bipolar attachment of microtubules to sister centromeres and resists their precocious separation. *Nat Cell Biol*. 2:492-9.

Tremethick, D.J. 2007. Higher-order structures of chromatin: the elusive 30 nm fiber. *Cell*. 128:651-4.

Uchida, K.S., K. Takagaki, K. Kumada, Y. Hirayama, T. Noda, and T. Hirota. 2009. Kinetochore stretching inactivates the spindle assembly checkpoint. *J Cell Biol*. 184:383-90.

Warsi, T.H., M.S. Navarro, and J. Bachant. 2008. DNA topoisomerase II is a determinant of the tensile properties of yeast centromeric chromatin and the tension checkpoint. *Mol Biol Cell*. 19:4421-33.

Weber, S.A., J.L. Gerton, J.E. Polancic, J.L. DeRisi, D. Koshland, and P.C. Megee. 2004. The kinetochore is an enhancer of pericentric cohesin binding. *PLoS Biol*. 2:E260.

Winey, M., C.L. Mamay, E.T. O'Toole, D.N. Mastronarde, T.H. Giddings, Jr., K.L. McDonald, and J.R. McIntosh. 1995. Three-dimensional ultrastructural analysis of the Saccharomyces cerevisiae mitotic spindle. *J Cell Biol*. 129:1601-15.

Yang, S.S., E. Yeh, E.D. Salmon, and K. Bloom. 1997. Identification of a mid-anaphase checkpoint in budding yeast. *J Cell Biol*. 136:345-54.

Yeh, E., J. Haase, L.V. Paliulis, A. Joglekar, L. Bond, D. Bouck, E.D. Salmon, and K.S. Bloom. 2008. Pericentric chromatin is organized into an intramolecular loop in mitosis. *Curr Biol*. 18:81-90.

Yong-Gonzalez, V., B.D. Wang, P. Butylin, I. Ouspenski, and A. Strunnikov. 2007. Condensin function at centromere chromatin facilitates proper kinetochore tension and ensures correct mitotic segregation of sister chromatids. *Genes Cells*. 12:1075-90.

Yoshimura, S.H., K. Hizume, A. Murakami, T. Sutani, K. Takeyasu, and M. Yanagida. 2002. Condensin architecture and interaction with DNA: regulatory non-SMC subunits bind to the head of SMC heterodimer. *Curr Biol*. 12:508-13..

CHAPTER 2

PERICENTRIC CHROMATIN LOOPS FUNCTION AS A NONLINEAR SPRING IN MITOTIC FORCE BALANCE

This chapter is adapted from a publication in The Journal of Cell Biology (Stephens et al., 2013). Rachel A. Haggerty, Paula A. Vasquez, Leandra Vicci, Chloe E. Snider, Fu Shi, Cory Quammen, Christopher Mullins, Julian Haase, Russell M. Taylor II., Jolien S. Verdaasdonk, Michael R. Falvo, Yuan Jin, M. Gregory Forest, and Kerry Bloom aided in experiments, analysis of data, and writing.

Summary

The mechanisms by which sister chromatids maintain bi-orientation on the metaphase spindle are critical to the fidelity of chromosome segregation. Active force interplay exists between predominantly extensional microtubule-based spindle forces and restoring forces from chromatin. These forces regulate tension at the kinetochore that silences the spindle assembly checkpoint to ensure faithful chromosome segregation. Depletion of pericentric cohesin or condensin has been shown to increase the mean and variance of spindle length that have been attributed to a softening of the linear chromatin spring. Models of the spindle apparatus with linear chromatin springs that match spindle dynamics fail to predict the behavior of pericentromeric chromatin in wild-type and mutant spindles. We demonstrate

that a non-linear spring with a threshold extension to switch between spring states, predicts asymmetric chromatin stretching observed *in vivo*. Addition of cross-links between adjacent springs recapitulates coordination between pericentromeres of neighboring chromosomes.

Introduction

The mitotic spindle ensures the equal distribution of chromosomes during cell division. Sister chromatids are bioriented through binding via the kinetochore, to microtubules emanating from opposite spindle poles (Figure 2.1 A). The kinetochore is a specialized protein/DNA structure built on centromere DNA that binds to the plus-end of dynamically growing and shortening kinetochore microtubules (kMT). In yeast, each chromosome is tethered to the spindle via a single kMT (Peterson and Ris, 1976; O'Toole et al., 1999). The kinetochore promotes the formation of a pericentric chromatin loop (Yeh et al., 2008), predisposing the kinetochore to protrude from the surface of the chromosome. Cohesin and condensin complexes are enriched in approximately 50kb of the pericentric chromatin (Blat and Kleckner, 1999; Megee et al., 1999; Tanaka et al., 1999; Hagstrom et al., 2002; Wang et al., 2005) that together with DNA constitute the "chromatin spring" to counter microtubule-based forces (Bouck and Bloom, 2007; Stephens et al., 2011). Interpolar microtubules (ipMT) from opposite spindle poles overlap and are cross-linked by microtubule motor proteins and microtubule associated proteins. Kinesins act as force production machines that slide the ipMTs apart generating an extensional force on the spindle pole bodies (Saunders and Hoyt, 1992; Saunders et al., 1997). The balance of microtubule based extensional force and a chromatin spring contractile force is necessary to

produce a steady state spindle length and tension at the kinetochore that satisfies the spindle checkpoint (Bloom and Yeh, 2010).

The microtubules, microtubule-based motor proteins and kinetochore components of the segregation apparatus have been explored with biophysical techniques, leading to a detailed understanding of their function (Mogilner and Craig, 2010; Alushin and Nogales, 2011; McIntosh et al., 2012; Umbreit and Davis, 2012; Watanabe, 2012). Mathematical models of the metaphase spindle in a number of systems aim to account for the distribution and dynamics of spindle microtubules (Sprague et al., 2003; Cytrynbaum et al., 2005; Gardner et al., 2005; Wollman et al., 2005; Civelekoglu-Scholey et al., 2006; Gay et al., 2012). We and others have developed stochastic models of kMT plus-end dynamics in the metaphase spindle that were evaluated by statistical measures of how well simulations predicted experimentally observed distributions of fluorescent kinetochore proteins (Sprague et al., 2003; Gardner et al., 2005; Gardner et al., 2007; Gardner et al., 2010). In these models, introduction of spatial gradients in dynamic instability across the spindle, as well as tension-mediated regulation of kMT plus-end dynamics, were required to fit experimental data (Gardner et al., 2005). A stochastic model that includes kinetochore attachment and detachment accurately recapitulates chromosome dynamics during metaphase and anaphase as well as the time-scale for correction of erroneous attachments in *S. pombe* (Gay et al., 2012). Although, microtubule dynamics were not explicitly modeled, the Gay et al. (Gay et al., 2012) model incorporated a spatial gradient in kMT detachment rate (inspired by the Aurora B spatial gradient in vertebrate cells; Liu et al., 2009; Welburn et al., 2010) that is analogous to the spatial gradients of Gardner and colleagues (Gardner et al., 2005). Overall, with appropriate tuning of the spatial gradients, these models were able to recapitulate

experimentally observed features of microtubule plus-end fluorescence (Gardner et al., 2005), kinetochore separation, and laser ablation (Gay et al., 2012). However, none of the models explicitly consider the physical properties of the chromatin spring (reviewed in Mogilner and Craig, 2010).

Simple models have assumed that chromatin behaves as a Hookean (i.e. linear force-extension relation) spring. This spring is presumed to be derived via cohesion between sister chromatids (Gay et al., 2012), cohesin and condensin-based chromatin loops (Ribeiro et al., 2009; Stephens et al., 2011), or an entropic worm-like chain (Greulich et al., 1987).

Here we developed models for the chromatin spring based on experimental observations in budding yeast. Several features of budding yeast make it particularly amenable for a quantitative analysis of the contributions of chromatin to spindle structure and dynamics. The mitotic spindle is streamlined and stereotypic (250 nm dia. x 1400-1600 nm length cylinder), providing the opportunity for statistical analysis of length and its variation with time (Winey and Bloom, 2012). Condensin and cohesin are enriched in the pericentric chromatin and occupy unique spatial positions relative to the spindle microtubules and kinetochore (Stephens et al., 2011). Condensin lies proximal to the spindle axis and is responsible for axial compaction by looping pericentric chromatin, while cohesin is radially displaced from the spindle axis and confines pericentric chromatin loops around the spindle apparatus (Figure 2.1 A; Stephens et al., 2011). Through the use of integrated LacO arrays and LacI-GFP we can visualize the chromatin at known distances (in base pairs) from the microtubule attachment site defined by a 125 bp DNA sequence. A linear spring in a predictive mathematical model fails to predict spindle length and chromatin dynamics. Cross-

linked chromatin loops with non-linear length changes provide a working model for the nature of the chromatin spring in mitosis.

Results

Force balance within the budding yeast mitotic spindle

The components contributing to force balance in the mitotic spindle are depicted in Figure 2.1 B. We consider three main force-generating processes: (i) an extensional force arising from motors sliding ipMT, F_{ip}; (ii) an opposing contractile force generated by the chromatin spring, F_k; and (iii) a viscous drag force, F_{drag}. Other forces acting on the spindle and not considered in the model are described in Materials and methods. At the low Reynolds numbers inside the cell, the F_{drag} is proportional to the velocity of the spindle length (denoted L_{ip}) given by Stokes law (Batchelor, 1967), $F_{drag} = -C_{drag}\, V_{ip}$ where $V_{ip} = dL_{ip}/dt$. Holding one spindle pole fixed and summing all forces acting along the primary spindle axis, we obtain the net force on the moveable spindle pole,

$$\sum F_{on\ spindle\ pole} = F_{ip} + F_k + F_{drag} = F_{net}. \qquad \text{Eqn. 1}$$

Based on a linear force-velocity relation, as explained in the supplemental material, we arrive at a dynamical equation for spindle length,

$$\frac{dL_{ip}(t)}{dt} = V_{ip}(t) = V_{max}\left(1 + \frac{F_k(t) + F_{drag}(t)}{F_{ip}(t)}\right), \qquad \text{Eqn. 2}$$

where V_{max} is the maximum velocity of the spindle motors (Table 2.6, Spindle velocity).

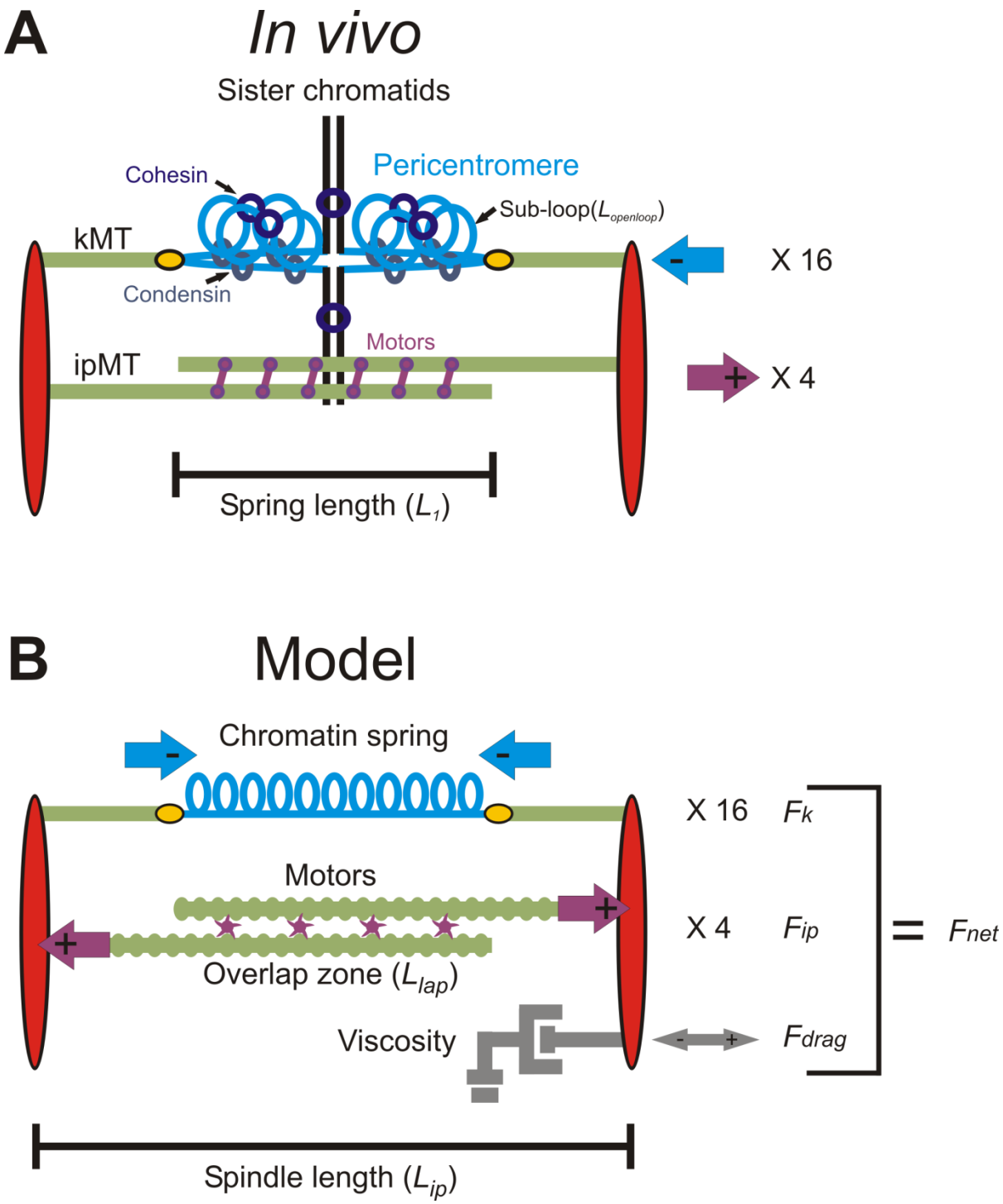
A
In vivo
Sister chromatids
Cohesin
Pericentromere
Sub-loop($L_{openloop}$)
kMT
Condensin
X 16
Motors
ipMT
X 4
Spring length (L_1)
B
Model
Chromatin spring
X 16
F_k
Motors
X 4
F_{ip}
=
F_{net}
Overlap zone (L_{lap})
Viscosity
F_{drag}
Spindle length (L_{ip})

Figure 2.1 Structure of the yeast mitotic spindle

(A) Microtubules (kinetochore microtubules, green) emanating from opposite spindle pole bodies (red) bind to the centromere via the kinetochore (yellow). Sister centromeres are spatially separated in metaphase and reside at the apex of a pericentric chromatin loop (C-loop, in blue) that extends perpendicularly from the chromosome axis (black; Yeh et al., 2008). The total contour length of the pericentric chromatin loop is split between an axial component (approximated by the distance between the two kinetochores, L_1) and sub-loops ($L_{openloop}$) that extend perpendicular to the spindle axis. Condensin is more proximal to the spindle axis than cohesin. Approximately 8 interpolar microtubules overlap (two shown) and are bound by kinesin 5 motor proteins (purple). While only one replicated chromosome is depicted with two kinetochore microtubules, there are 16 chromosomes (32 sister chromatids) in budding yeast and approximately 32 kinetochore microtubules. The 16 kinetochores from each pole are clustered in mitosis. The aggregate chromatin spring length is measured by the distance between the two clusters (L_1). (B)The model is written as a coupled system of stochastic and deterministic differential equations in which the sum of the forces applied to one spindle pole body is used to numerically solve for velocity at each time step. Spindle length is defined experimentally as the distance between the spindle pole bodies (red) in metaphase (L_{ip}). The pericentric chromatin functions as a spring (blue, F_k). Its length is the distance between two sister kinetochore microtubule plus-ends (L_{spring}). Kinesin motors (purple) bind to and couple ipMTs at the overlap zone (L_{lap}) and slide ipMTs apart generating an outward extensional force F_{ip}. The viscous properties of the nucleus are represented as a dashpot and resist movement of the spindle pole bodies in either direction (gray, F_{drag}).

This force balance model is written as a coupled system of stochastic and deterministic differential equations in which the sum of the forces applied to one spindle pole body yields the dynamics of the spindle length (L_{ip}), through integration of Eqn. 2.

The basis for a stable spindle length in our model is that a quasi-steady state is reached between inward and outward forces, with fluctuations about a mean spindle length arising from microtubule-based motor activity. This mean length is dictated by the mean number of force-producing motors in the overlap zone and the corresponding extension of the chromatin springs from their rest length, which give F_{ip} and F_k, respectively (Figure 2.1). The outward force (F_{ip}) arises from sliding of antiparallel ipMTs due to plus-end-directed motors bound in the overlap region (denoted double-bound motors, $D(t)$). The forces exerted by each motor, F_{m}, are additive, so F_{ip} is proportional to the total number of double bound motors,

$$F_{ip} = D(t) \times F_{\mathrm{m}} \qquad \text{Eqn. 3}$$

The number of productive motors $D(t)$ is given by rates of attachment and detachment, K_{on} and K_{off}, so that $D(t)$ fluctuates with a Poisson distribution. The length of the chromatin spring L_{sp} is total spindle length L_{ip} minus the length of each kinetochore microtubule ($L_{kMT}^{\mathrm{left}}, L_{kMT}^{\mathrm{right}}$), where L_{kMT}^{left} and L_{kMT}^{right}, are the length of the left and right kMT, respectively. Thus the chromatin restoring force is $F_k = -k_{sp}\left(L_{ip} - L_{kMT}^{\mathrm{left}} - L_{kMT}^{\mathrm{right}} - L_{rest}\right)$, where L_{rest} is the rest length of the spring in the absence of force. L_{rest} is estimated to be ~200 nm (Table 2.6), based on an upper bound given by the diffraction limit ~250 nm (as sister centromere-linked LacO arrays are not resolved following spindle collapse) and a lower bound given by the chromatin persistence length 170-220 nm (Bystricky et al., 2004). With these assumptions Eqn. 2 becomes,

$$V_{ip}(t) = \left(\frac{V_{max}}{F_M D(t) + V_{max} C_{drag}}\right) \times \left(F_M D(t) - k_{sp}\left(L_{ip}(t) - L_{kMT}^{\text{left}}(t) - L_{kMT}^{\text{right}}(t) - L_{rest}\right)\right), \quad \text{Eqn. 4}$$

A linear spring model recapitulates the increase in both the mean and variance of spindle length observed in mutant cells

We first perform numerical simulations with a minimal linear stochastic model (MLS), where L_{kMT}(t) and $D(t)$ are described, respectively, by Gaussian and Poisson distributions. The model predicts increases in mean and variance of spindle length upon decreasing the linear chromatin spring constant (Figure 2.2, E and F) consistent with experimental observations (Stephens et al., 2011). However the MLS model fails to capture features such as the spatial distribution of kinetochore microtubules (Gardner et al., 2005) and asymmetry in the behavior of the chromatin spring (Stephens et al., 2011). Therefore, unlike the situation in certain transcriptional networks (Munsky et al., 2012), or the bimodal response to extracellular signaling (Birtwistle et al., 2012; Kim and Sauro, 2012) our results demonstrate that noise is insufficient to enhance our understanding of mitotic spindle behavior.

We introduced a spatial catastrophe gradient and tension-dependent rescue of kMT plus-end dynamics (Materials and methods Eqn B6 and 7). This new model, termed the coupled linear stochastic (CLS) model couples microtubule and spring dynamics. As the chromatin spring lengthens, tension on the kMT increases, switching the MT from shortening to growth (rescue), while the growing kMT allows the chromatin spring to shorten, reducing tension. We incorporated experimentally measured motor on and off rates and distributed the total number of motors among four species (unbound, kMTs, ipMTs, and double bound in the interpolar zone, see Materials and methods). The interpolar overlap zone (L_{lap}) is the

region where antiparallel ipMTs from each spindle pole are bundled (Winey et al., 1995; O'Toole et al., 1999). The extensional force (F_{ip}) depends on the number of kinesin motors bound to antiparallel microtubules (L_{lap}). Parameter values are detailed in Table 2.6. Since Ase1 binds anti- and parallel microtubule bundles (Janson et al., 2007) this provides an upper estimate on overlap zone length. To estimate L_{lap} we introduced Ase1-GFP in cells with labeled spindle pole bodies (Spc29-RFP, Figure 2.9). The distribution of Ase1-GFP increases linearly with spindle length in metaphase (slope of 0.45, Figure 2.9 A). Utilizing either constant or length-adjusted L_{lap} does not affect the trends in spindle length and variation (Figure 2.9 and 2.10). We used the constant overlap zone in the model based on the robustness of the sensitivity analysis (Figure 2.10 and 2.11).

The physical behavior of the pericentric chromatin depends upon the concentration of cohesin and condensin complexes. Reduction of pericentric cohesin (*mcm21*Δ) or condensin (*brn1-9*) leads to increased spindle length and variation (Figure 2.3 A, II and III; Stephens et al., 2011). Variation in spindle length refers to fluctuations about the mean over a time-course of observation. In the model, *mcm21*Δ is captured by decreasing the chromatin spring constant (Figure 2.3 B I, Table 2.2). A decreased (softer) spring in the CLS model leads to an increased mean spindle length and greater variance in spindle length, (Figure 2.3 B, II and III). Introduction of experimentally measured motor on/off rates and kMT dynamics, and 16 individual springs did not alter the trend from the minimal model (Figure 2.2, E and F). Increases in spindle length and variation upon depletion of pericentric cohesin or condensin can be recapitulated through decreasing the linear chromatin spring constant in both a minimal (MLS) and coupled model (CLS).

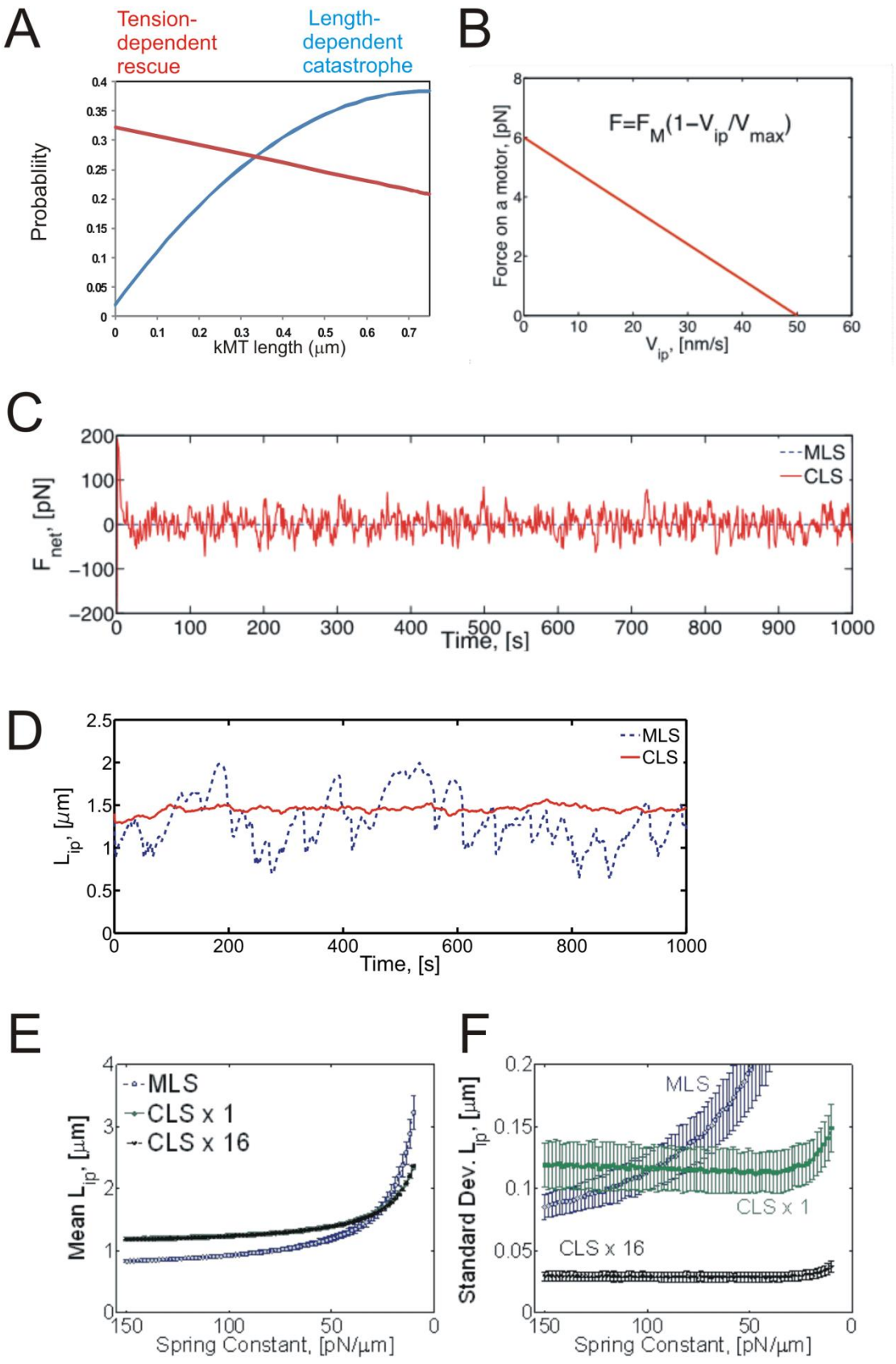
A
Tension-dependent rescue
Length-dependent catastrophe
Probability
kMT length (μm)
B
F=F_M(1−V_ip/V_max)
Force on a motor, [pN]
V_ip, [nm/s]
C
MLS
CLS
F_net, [pN]
Time, [s]
D
MLS
CLS
L_ip, [μm]
Time, [s]
E
MLS
CLS x 1
CLS x 16
Mean L_ip, [μm]
Spring Constant, [pN/μm]
F
MLS
CLS x 1
CLS x 16
Standard Dev. L_ip, [μm]
Spring Constant, [pN/μm]

Figure 2.2 Addition of experimentally measured kMT dynamics and motor on/off rates maintains trends of a minimal model

(A) Fitted probabilities of switching kMT states based on tension-dependent rescue and length-dependent catastrophe (Gardner et al., 2005). (B) Motor velocity vs. force on motor determined as a linear equation between maximum velocity (50 nm/sec) and motor stall force (6 pN). (C) F_{net} in the MLS and CLS models. (D) Spindle length over time for MLS and CLS models. (E) Mean spindle length and (F) spindle variation over a time-lapse for MLS, CLS 1 spring, and CLS 16 springs upon decreasing the spring constant.

A non-linear spring hypothesis

During metaphase sister LacO/LacI-GFP arrays inserted proximal to the centromere appear as diffraction limited spots that transiently separate into two foci upon biorientation (Goshima and Yanagida, 2000; He et al., 2000; Tanaka et al., 2000; Pearson et al., 2001). These LacO arrays can switch between a focus and a linear filament (~450 nm length, nucleosome fiber packing) indicative of decompaction and extension (Figure 2.3 C and Figure 2.5; He et al., 2000; Bachant et al., 2002; Warsi et al., 2008). If the pericentric chromatin were a simple linear spring as in the CLS model, sister chromatid LacO arrays would experience the same force and stretch to the same degree. For wild-type, 10% of cells exhibit chromatin stretching. However only one of the sister LacO arrays stretches (ex. Figure 2.3 C and 2.5; Asymmetric stretching: WT 100% n = 102; *mcm21Δ* 90% n = 59; *brn1-9* 95% n = 43, Stephens et al., 2011). In the stretched state LacO arrays occupy a spindle proximal position relative to the compacted foci (Stephens et al., 2011). The changes in compaction and spatial position provide evidence for dynamic chromatin loops not accounted for by linear spring models (MLS or CLS).

To account for the asymmetry in chromatin extension we model chromatin loops (Figure 2.3 C I; Stephens et al., 2011) as a piecewise continuous function that exhibits a saw-tooth force vs. extension law. At a characteristic "threshold" length, a loop unravels, switching the spring constant (Figure 2.3 C I). In the stretched state, the increase in available chromatin ($L_1 + L_{openloop} = L_2$) is compensated by a decrease in spring constant, such that $k_2 = k_1*(L_1/ L_2)$ in order to maintain force ($F = -k\ (L - L_{rest})$). The aggregate experimental wild-type spring length is 800 nm (L_1, Figure 2.1 A). The length of chromatin added upon triggering the threshold condition is estimated to be 450 nm ($L_{openloop}$). The length reflects the

nucleosomal contour length of the sub-loops (see Figure 2.1 A; Table 2.6, 10kb of pericentric chromatin ~450nm of 11nm fiber, L_2 = 800 + 450 =1250 nm). Furthermore we consider an increase in the chromatin rest length $L_{1rest} + L_{openloop} = L_{2rest}$, in agreement with experimental evidence that depletion of pericentric cohesin or condensin affects pericentric sister LacO separation in the absence of tension (Lam et al., 2006; Vas et al., 2007; Ng et al., 2009). Unlike previous models, this coupled non-linear stochastic model (CNLS) contains a piecewise continuous spring that accounts for dynamically extensible asymmetry in the chromatin spring.

The non-linear spring model recapitulates the frequency of chromatin stretching and increase in both the mean and variance of spindle length observed in mutant cells

To estimate the threshold at which the spring stretches, we explored model values that best fit the frequency of stretching observed *in vivo*. The mean distance between paired kinetochore microtubules is ~800nm in wild-type cells. In simulations we explored parameter values of spring extension threshold between 800-1100 nm. A threshold of 975 nm reproduces the frequency of ~10% stretching in wild-type cells (Figure 2.3, A IV and C IV). Cells depleted of pericentric cohesin or harboring temperature sensitive mutants in condensin have longer spindles in metaphase, increased spindle length variance and increased frequency of chromatin stretching (Figure 2.3 A). The distance at which chromatin stretching is observed therefore depends upon the concentration of cohesin and condensin within the spindle (Stephens et al., 2011). As the spring threshold is reduced, there is an increased frequency of chromatin stretching in the CNLS model (Figure 2.3 C IV). Decreasing the threshold in the model to 925-950 nm best matches the frequency of stretching observed in mutant cells depleted of cohesin or condensin (~50% stretching).

Simulations with the CNLS model show an increase in spindle length variation with increases in the fraction of stretched chromatin strands (variation 65 to 135 nm, 10-50% stretching, Figure 2.3 C, III and IV). When all 16 springs are in the same conformational state (all k_1 or k_2) the variance on the spindle length is minimal. Similarly, the maximum variance occurs when roughly half of the springs are in a given state (Figure 2.3 C, III and IV). In experiments, populations of WT spindles (~10% stretching) have reduced length variance relative to mutant populations where ~50% of cells show pericentric chromatin stretching (pericentric cohesin and condensin mutants; Figure 2.3 A, III and IV). Experimental observations of spindle length distributions in cells with compact vs. stretched LacO arrays reveal two distinct populations in both wild-type and mutant cells (WT, $P < 1.5\times10^{-11}$; *mcm21Δ*, $P < 1.3\times10^{-10}$; *brn1-9*, $P < 1\times10^{-6}$; Figure 2.4, F-H). This is also evident from fitting the probability distribution functions (PDFs) of spindle lengths in WT, *mcm21Δ*, and *brn1-9* with Gaussian distributions (Figure 2.4, C-E; Table 2.1). While fittings to the CLS data with one or two Gaussians were indistinguishable from each other; introducing a second Gaussian consistently improved the goodness of fit for the CNLS data (Table 2.1, R^2 values). The multiplicities of modes in the CNLS model reflect the stretching process through the non-linear spring law.

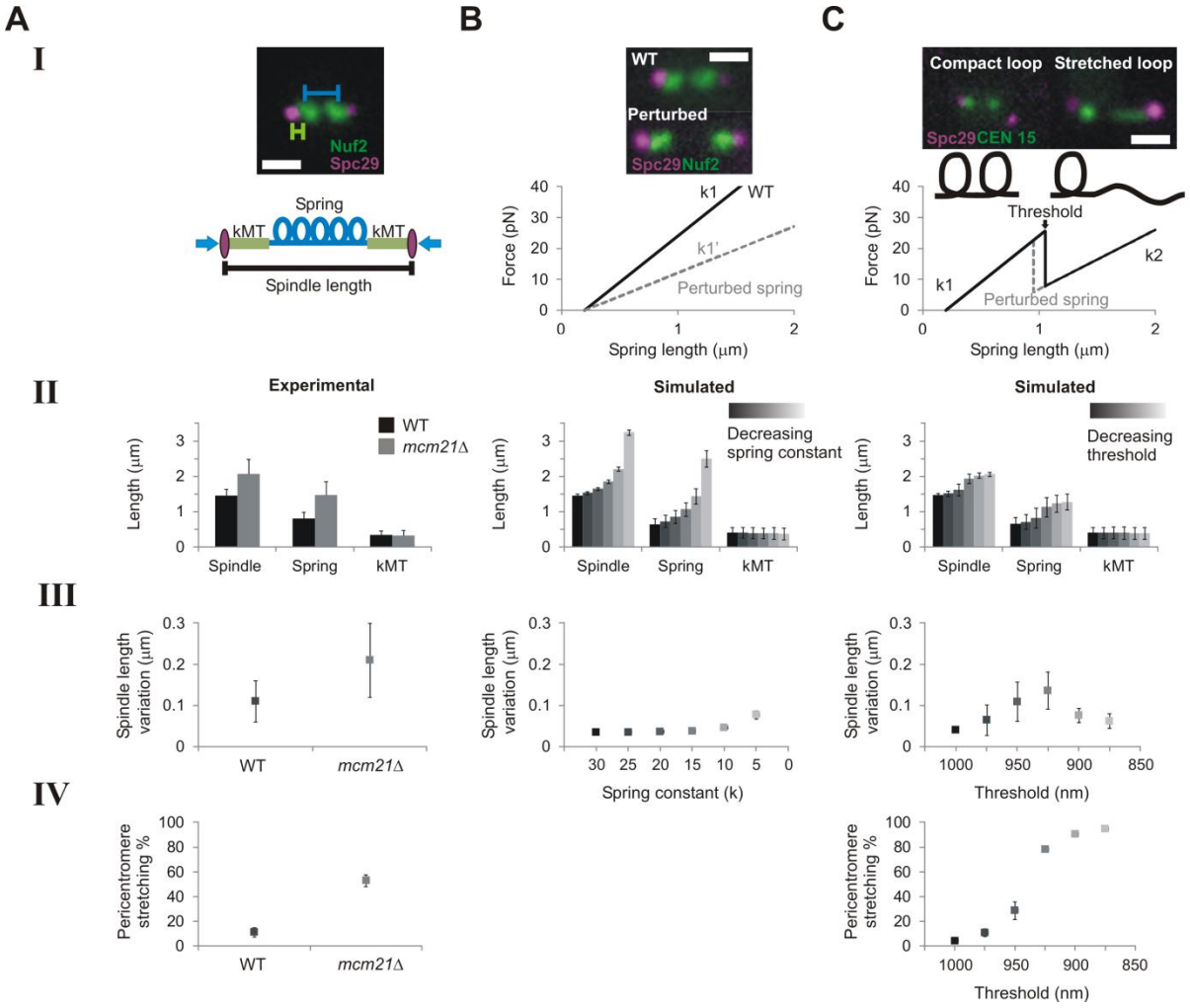
A
B
C
I
II
III
IV
H
Nuf2
Spc29
Spring
kMT
kMT
Spindle length
WT
Perturbed
Spc29Nuf2
Force (pN)
k1
WT
k1'
Perturbed spring
Spring length (μm)
Compact loop
Stretched loop
Spc29CEN 15
Threshold
k2
k1
Perturbed spring
Experimental
Simulated
Simulated
WT
mcm21Δ
Length (μm)
Spindle
Spring
kMT
Decreasing spring constant
Decreasing threshold
Spindle length variation (μm)
WT
mcm21Δ
Spring constant (k)
Threshold (nm)
Pericentromere stretching %

Figure 2.3 Model simulations with a piecewise continuous spring recapitulate experimental observations

(A) Experimental data of WT and *mcm21*Δ cells (pericentromere depleted of cohesin). Spindle length (II) and pericentromere stretching (IV) were measured using population images of cells containing Spc29-RFP spindle poles and LacO at CEN15 respectively. Spindle length variation (III, fluctuation about the mean spindle length) was measured by tracking spindle poles over ~10 min (Stephens et al., 2011). (B) Numerical simulations of spindle dynamics with a linear chromatin spring $F = -k\ (L_{spring} - L_{rest})$ where L_{rest} = 200nm (lighter = decreasing spring constant). The spring constant (k) was decreased to simulate perturbation of the spring (see B I). Experimental images display an increase in the interkinetochore distance (distance between kinetochore clusters, Nuf2) in cohesin/condensin mutants. Simulations using a Hookean spring do not generate asymmetric pericentromere stretching. (C) Simulations of spindle dynamics with the spring defined by a piecewise continuous equation dependent on a threshold (lighter = decreasing threshold). Experimental images (top) reveal two spring states (compact, stretched) of a pericentromere LacO array. Under a force threshold ($L_{threshold}$) the spring is looped (k_1 and L_{rest1}, compact) and above the threshold a loop stretches adding length to the spring which decreases the spring constant and increases the rest length (k_2 and L_{rest2}, stretched). When $L_{spring} < L_{threshold}$, $F = -k_1\ (L_{spring} - L_{rest})$. At $L_{spring} \geq L_{threshold}$, the spring constant is reduced from k_1 to k_2 ($k_2 = k_1\ (L_1/L_1+L_{openloop})$ and greater rest length ($L_{rest2} = L_{rest1} + L_{openloop}$), giving $F = -k_2\ (L_{spring} - L_{rest2})$, where the mean experimental aggregate spring length is L_1 = 800 nm and $L_{openloop}$= 450 nm (10 kb of nucleosomal chromatin from stretched loop). Simulated population measurements for (B) linear and (C) non-linear spring models (spindle length, II and pericentromere stretching, IV) were generated by running the model and randomly selecting one time step (n = 500, 5

groups 100 simulations each). Simulated (B and C) time lapses (III) were run for 1000 seconds, 50 sec for equilibrating and 950 sec measured (n = 25). Scale bar = 1 μm. Error bars represent standard deviation.

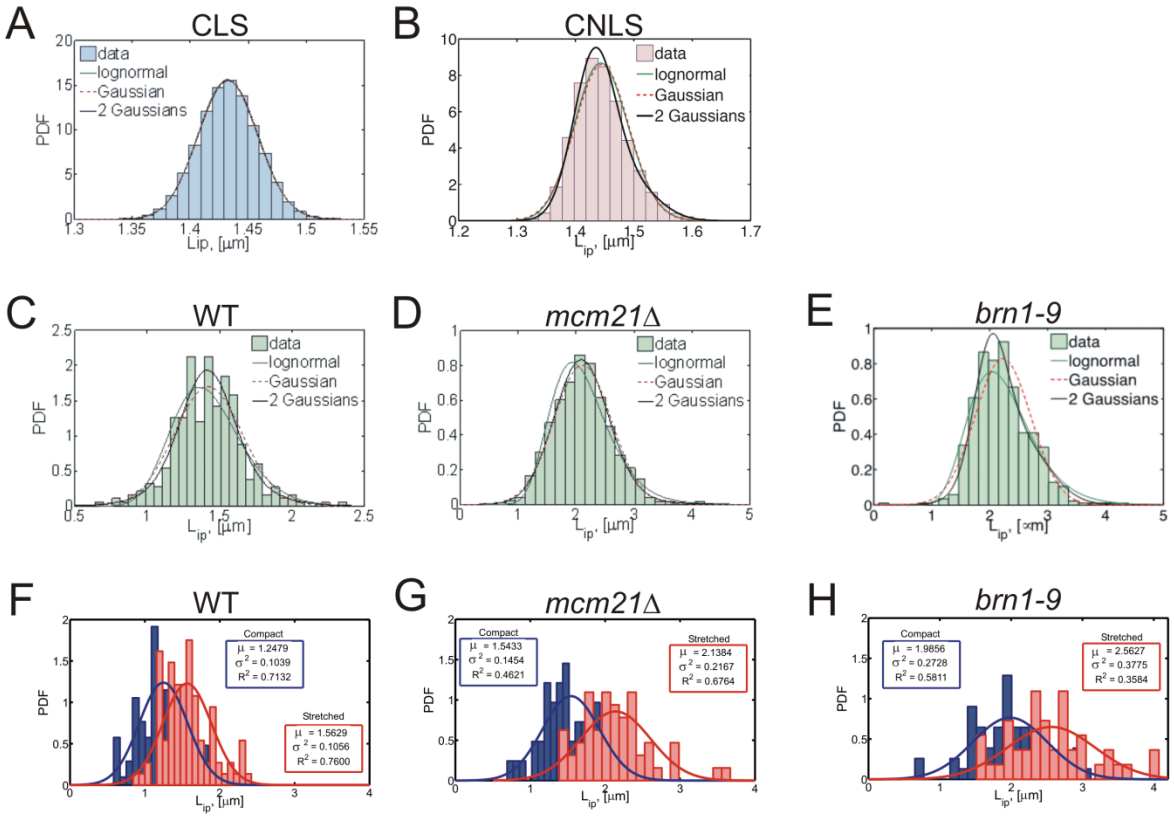
A
CLS
data
lognormal
Gaussian
2 Gaussians
PDF
Lip, [μm]
B
CNLS
C
WT
D
mcm21Δ
E
brn1-9
F
WT
Compact
μ = 1.2479
σ2 = 0.1039
R2 = 0.7132
Stretched
μ = 1.5629
σ2 = 0.1056
R2 = 0.7600
G
mcm21Δ
Compact
μ = 1.5433
σ2 = 0.1454
R2 = 0.4621
Stretched
μ = 2.1384
σ2 = 0.2167
R2 = 0.6764
H
brn1-9
Compact
μ = 1.9856
σ2 = 0.2728
R2 = 0.5811
Stretched
μ = 2.5627
σ2 = 0.3775
R2 = 0.3584

Figure 2.4 Spindle length histograms of simulations and experimental conditions Probability distribution functions of (A) CLS, wild-type (B) CNLS, wild-type (C) Experimental, wild-type (D) Experimental, *mcm21Δ*, depletion of pericentric cohesin and (E) Experimental, *brn1-9*, depletion of condensin. Each histogram was fitted with a lognormal (green line), 1 Gaussian (red dotted-line), and 2 Gaussian (black line). Lognormal and 1 Gaussian represent unimodal, while 2 Gaussian represents bimodal. R^2 values are given in Table S2. Histograms of the spindle length distributions in (F) WT, (G) *mcm21Δ*, and (H) *brn1-9* cells with only compact LacO arrays (blue) vs. cells with stretched LacO arrays (red). These graphs reveal two distinct populations in both wild-type and mutant cells (WT, n = 218, $P < 1.5\times10^{-11}$; *mcm21Δ*, n = 106, $P < 1.3\times10^{-10}$; *brn1-9*, n = 106, $P < 1\times10^{-6}$). Spindles with stretched LacO arrays are on mean 500nm longer and exhibit increased variance relative to spindles with compact LacO arrays.

Table 2.1 WT and mutant spindle length histogram best-fits

R^2 fit	WT	*mcm21Δ*	*brn1-9*	CLS	CNLS
1 Gaussian	.8895	0.9732	0.9364	0.9971	0.9788
Lognormal	.8699	0.9502	0.9457	**0.998**	0.9813
2 Gaussians	**0.8977**	**0.9792**	**0.9742**	**0.998**	**0.9971**
N	317	756	496	9000	9000

Bold = best-fit

Dynamics of chromatin stretching reflect the rate of microtubule depolymerization

The dynamics of chromatin stretching provides a measure of kinetic coupling to microtubule growth and shortening. Chromatin stretching is not instantaneous but occurs within a timescale of 15 sec to minutes (Figure 2.5). In the model, kinetochore microtubule depolymerization is limited by the shortening rate (1.5 μm/min). Upon an instantaneous change in spring constant, the tension on kinetochore microtubules is reduced and the microtubules switch to the shortening state (catastrophe). To determine whether the rate of pericentric chromatin extension and compaction is predicted by kMT dynamics we imaged cells depleted of pericentric cohesin (*mcm21Δ*) with LacO 1.8 kb from CEN 15 at 5 second intervals (Figure 2.5). The rate of chromatin extension (13 nm/sec or 0.8 ± 0.8 μm/min, $n = 9$ from 6 cells) and compaction (15 nm/sec or 0.9 ± 0.7 μm/min, $n = 9$ from 6 cells) is on the same timescale of microtubule shortening and growth, respectively (~1-1.5 μm/min, see Figure 2.5; Carminati and Stearns, 1997; Gardner et al., 2005). The CNLS model recapitulates the observed rate of change in chromatin shape. While the mechanism of chromatin extension and compaction are likely to be more complex than stretching and recoil of a random coil described herein, the rate of microtubule growth and shortening are consistent with the observed rate of change from spot to stretched LacO array in the pericentric chromatin. In addition, it is likely that microtubule shortening along the spindle axis pulls the LacO arrays proximal to the spindle axis where the chromatin continues to stretch as kMTs shorten (Stephens et al., 2011).

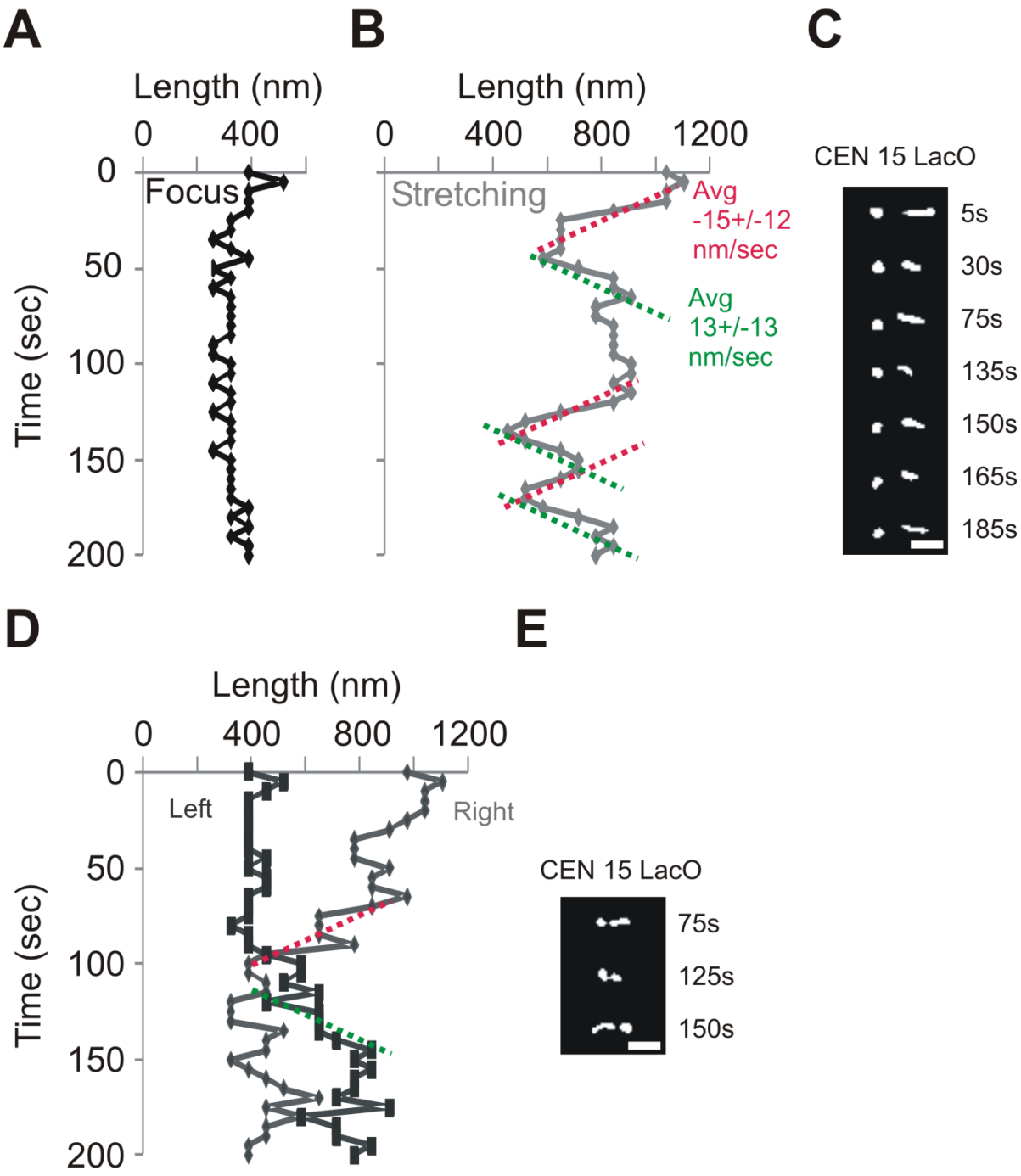
A
Length (nm)
0
400
0
50
100
150
200
Time (sec)
Focus
B
Length (nm)
0
400
800
1200
Stretching
Avg
-15+/-12
nm/sec
Avg
13+/-13
nm/sec
C
CEN 15 LacO
5s
30s
75s
135s
150s
165s
185s
D
Length (nm)
0
400
800
1200
0
50
100
150
200
Time (sec)
Left
Right
E
CEN 15 LacO
75s
125s
150s

Figure 2.5 Rate of pericentromere chromatin stretching and recompaction

Time-lapse microscopy of sister pericentric CEN 15 LacO arrays in *mcm21*Δ cells. Images were taken every 5s for 200s. Images were deconvolved as described in the Materials and methods, to determine the length of a LacO array along the spindle axis. (A,B,C) A representative time lapse shows stretching (line) and compaction (foci) of the LacO array over time. (A) Change in length of the left sister LacO array as a function of time in a single cell. The left LacO array appears predominantly as a spot, and is slightly larger than the diameter of a diffraction spot. (B) Length of the right sister LacO array as a function of time. To determine a mean compaction and stretching rate we fit a linear slope to regions that displayed greater than 3 successive steps in one direction. The mean compaction and stretching rates are -15 ± 12 nm/sec, n = 9; 13 ± 13 nm/sec, n = 9, respectively for 6 cells. (C) Selective images from the time lapse of sister LacOs A and B, time point indicated to the right. (D) Example from a time lapse indicating that sister chromatid stretching can switch from side to side. The right LacO array condenses as the left LacO array commences stretching. (E) Selective images from D, time point indicated to the right. Scale bar = 1 μm.

Decreasing the spring length threshold predicts declustering of kinetochore microtubule plus-ends

The 32 yeast kinetochores and kinetochore microtubule plus-ends, 16 on each side, are clustered into two foci each slightly larger than a diffraction-limited spot in metaphase (Haase et al., 2012). Based on the stochastic growth and shortening of kinetochore microtubules with no other spatial information, there is no *a priori* reason to expect that 16 individual microtubules emanating from the spindle pole will have the same length. In previous models spatial gradients for microtubule dynamics (Gardner et al., 2005) or Aurora gradients for kinetochore detachment (Gay et al., 2012) have been invoked. These gradients provide plausible mechanisms for kinetochore microtubule clustering. Alternatively, mechanisms to cluster individual kinetochore proteins or pericentric chromatin could contribute to kinetochore microtubule length control in the spindle. Depletion of histone H3 or pericentric cohesin (*mcm21*Δ) has been shown to result in the declustering of 16 kinetochores (Ng et al., 2009; Verdaasdonk et al., 2012). Herein we examined the clustering of the inner (Ame1p-GFP) and outer (Ndc80-GFP or Nuf2p-GFP) kinetochore (Figure 2.6 A, Nuf2 top). There is a significant disruption of kinetochore clusters in experimental conditions that increase chromatin stretching (*mcm21Δ* 32 ± 6% declustered, n = 230 vs. WT 9 ± 4%, n = 209; Figure 2.6 A). The physical basis for kinetochore declustering in these mutant conditions is unknown.

To compare predictions on kinetochore clustering from the coupled linear (CLS) and non-linear (CNLS) model with respect to experimental observations, we convolved the position of kinetochore microtubule plus-ends from the model with the point spread function (PSF) of our microscope objective; a process known as model convolution (Sprague et al., 2003; Gardner et al., 2010). The power of model convolution lies in the ability to perform a

statistical comparison between multiple runs of the model and multiple experimental images (Gardner et al., 2007; Gardner et al., 2010). To determine whether perturbation of a linear chromatin spring influences kinetochore microtubule plus-end clustering, we reduced the spring constant of the chromatin spring in the CLS model. This results in an insignificant change in kinetochore declustering over an order of magnitude change in spring constant (k = 30 pN/μm, 9 ± 1% vs. k = 5 pN/μm, 12 ± 3%, $\chi^2 > 0.30$; Figure 2.6 C). This is consistent with observed kinetochore clustering upon removal of the chromatin spring by preventing DNA replication via *cdc6* (Gardner et al., 2005). In contrast, when the chromatin stretching threshold is decreased (CNLS model) the incidence of declustering increases to experimentally observed levels (10 ± 1% to 22 ± 4%, $\chi^2 < 1\times10^{-4}$; Figure 2.6, B and D). In the CNLS model, declustering arises because of the non-linear behavior of 16 independent springs in the system. Thus, unlike simpler chromatin spring models, the discontinuous spring predicts kinetochore declustering in wild-type and mutant strains, as well as spindle length variation and asymmetric chromatin stretching (Table 2.2).

Chromatin springs may be cross-linked

To address whether the pericentromere chromatin springs of each chromosome are independent or coupled, we introduced two centromere-linked LacO arrays on different chromosomes (CEN 15 LacO/LacI-GFP, CEN11 TetO/TetR-CFP, Figure 2.7). In wild-type cells with a single labeled chromosome, the incidence of stretching is 12 ± 3% (Figure 2.7, *n* = 261; 11% Stephens et al., 2011). LacO and TetO arrays exhibit similar stretching frequencies (13% LacO and 11% TetO). If the springs stretch independently, then upon one

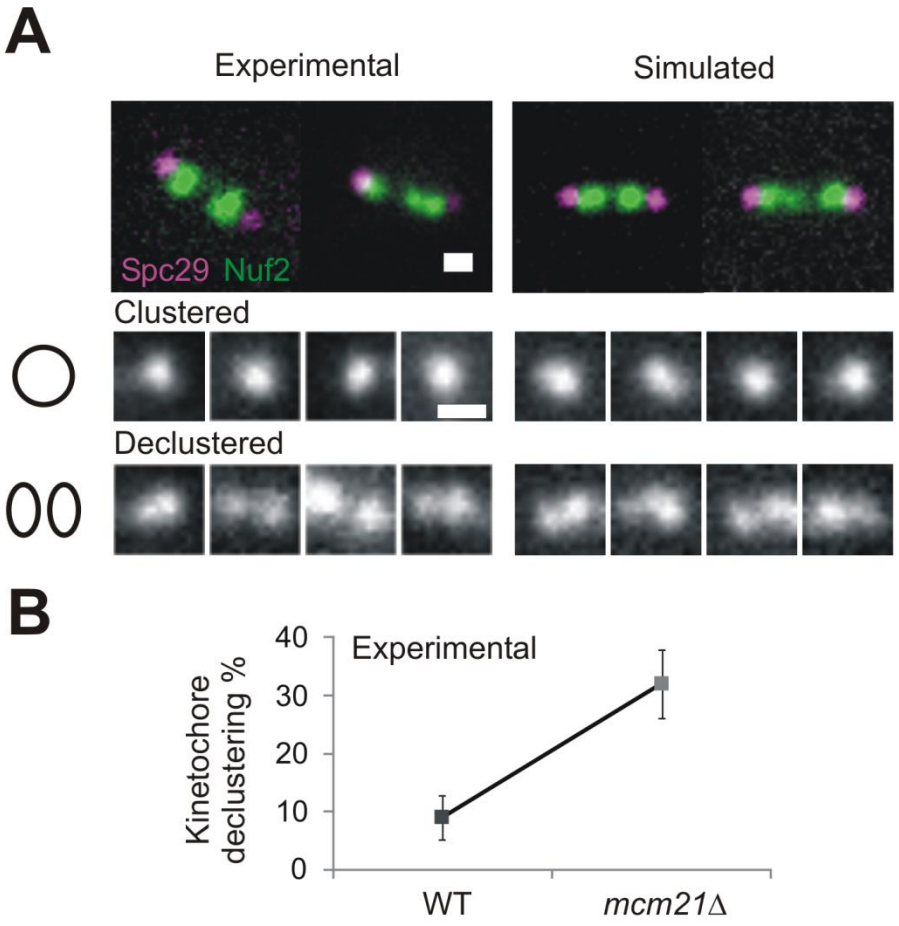
A
Experimental
Simulated
Spc29 Nuf2
Clustered
Declustered
B
Experimental
Kinetochore declustering %
40
30
20
10
0
WT
mcm21Δ
C
Simulated
Kinetochore declustering %
40
30
20
10
0
30 25 20 15 10 5 0
Spring constant (k)
D
Simulated
Kinetochore declustering %
40
30
20
10
0
1000 950 900 850
Threshold (nm)

Figure 2.6 Experimental kinetochore declustering is predicted by simulations with a piecewise continuous chromatin spring (CNLS), but not a linear spring (CLS)

(A) Experimental and simulated images of WT and *mcm21Δ* cells with Spc29-RFP (spindle poles, purple) and Nuf2 or Ndc80-GFP (kinetochores, green) were scored as clustered (kinetochore focus) or declustered in cells having the focus of 16 kinetochores split into multiple foci. Example experimental (left) and simulated (right) images showing a bundle of clustered (middle) and declustered (bottom). (B) Experimental declustering in WT and *mcm21Δ* cells (WT 9±4%, n = 209, 2 experiments; *mcm21Δ* 32 ± 6%, n = 230, 2 experiments). (C, D) Model simulations were used to generate images that match the physical geometry of the mitotic spindle (Model Convolution; Quammen et al., 2008; Gardner et al., 2010). The position of the spindle poles and plus end of each kMT were convolved with the point-spread function (PSF) of our microscope objective to produce a simulated image of spindle poles and clusters of kinetochore proteins at the microtubule plus-ends. Declustering was scored using the same criteria as in experimental images (n = 300, 3 groups of 100). (C) Decreasing the linear spring constant by an order of magnitude results in an insignificant increase (9% to 12%, $\chi^2 > 0.30$) kinetochore declustering. (D) Decreasing the threshold of a piecewise continuous spring results in a significant increase in declustering (10% to 22%, $\chi^2 < 1\times10^{-4}$) comparable to experimental (B vs. D). Scale bar = 1 μm. Error bars represent standard deviation.

spring stretching only 12% of cells should have a second labeled spring stretched. In contrast, coordinated stretching was much more frequent (Figure 2.7 B, WT 40 ± 16 % coordinated stretching, $n = 45$, $\chi^2 < 2\times10^{-17}$). The ~4-fold increase from the expected probability suggests that the dynamics of chromatin loops on different chromosomes are not independent. With pericentric chromatin cylindrically distributed around the spindle axis (based on the distribution of kinetochore microtubules), each strand would have two nearest neighbors in the region proximal to the kinetochores. We introduced cross-links in the model by introducing additional springs between nearest-neighbor chromatin strands. In this model, each chromosome is represented by a chromatin spring between the two spindle pole bodies and one cross-link spring is attached to each of the neighboring strands on either side (see Materials and methods). The cross-link springs apply force proportional to the difference in length between adjacent strands, acting to bring them to the same length.

In the CNLS model with no cross-linking, a threshold for stretching of 975 nm yields a spring stretching frequency of 11 ± 3% (n = 500, Figure 2.3 C IV) for any given chromosome, and a correlated stretching frequency of 13 ± 4% (Figure 2.7 B, simulated cross-linking = 0) for any given pair of chromosomes, consistent with independent probabilities. We investigated cross-linking spring constants ($k_{cross\text{-}link}$) corresponding to 0.1-0.5X the chromatin spring constant (30 pN/μm). Addition of cross-linking provides a mechanism to distribute tension between neighbors, making each chromatin spring less likely to stretch at a given spindle length. For a given $k_{cross\text{-}link}$, the threshold was altered to match the observed frequency of single chromosome stretching in wild-type cells (12 ± 2%, yielding 965-947 nm thresholds for 0.1-0.5X cross-linking springs). We found that

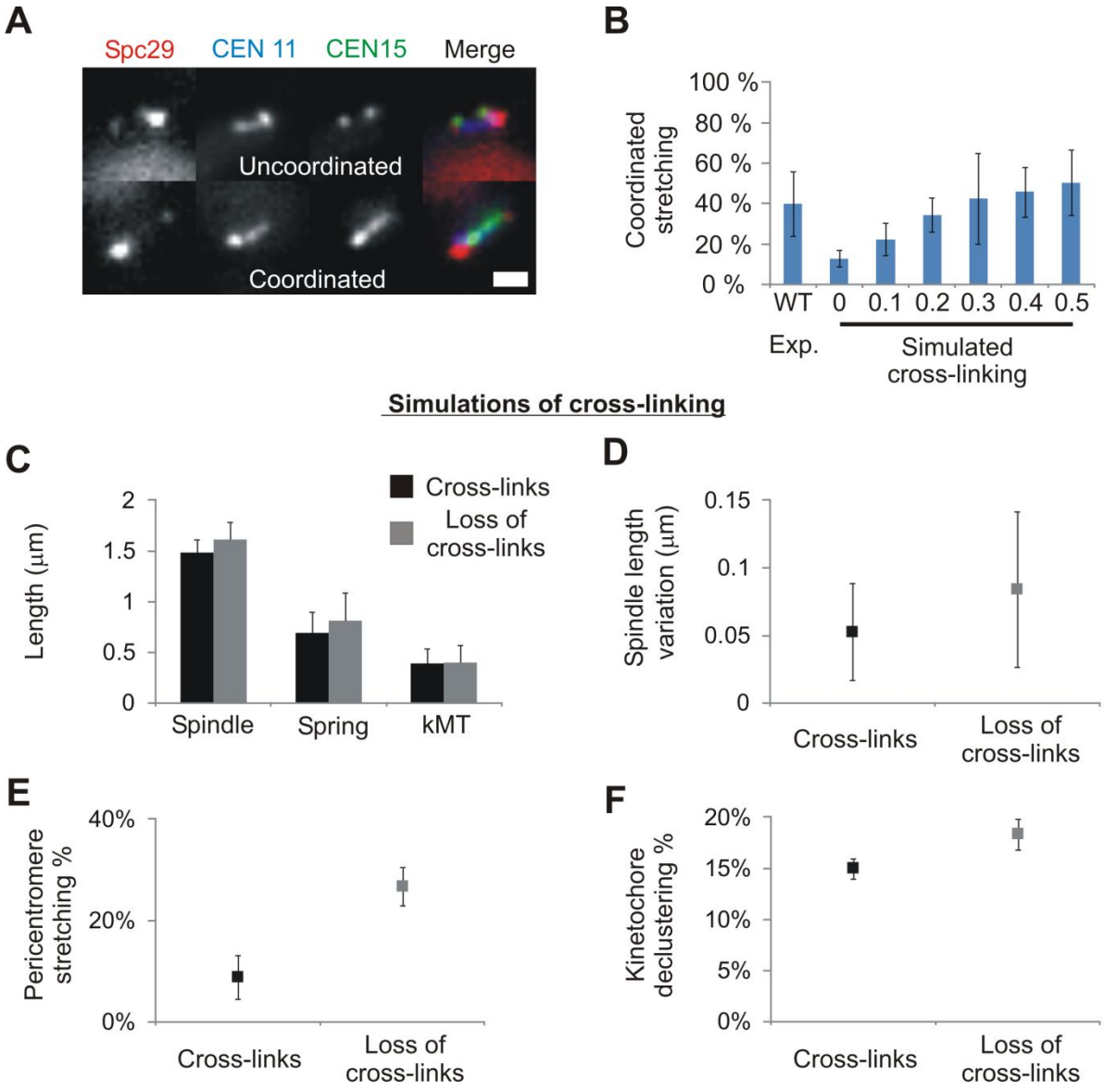
A
Spc29
CEN 11
CEN15
Merge
Uncoordinated
Coordinated
B
Coordinated stretching
100 %
80 %
60 %
40 %
20 %
0 %
WT
0
0.1
0.2
0.3
0.4
0.5
Exp.
Simulated cross-linking
Simulations of cross-linking
C
Length (μm)
2
1.5
1
0.5
0
Cross-links
Loss of cross-links
Spindle
Spring
kMT
D
Spindle length variation (μm)
0.15
0.1
0.05
0
Cross-links
Loss of cross-links
E
Pericentromere stretching %
40%
20%
0%
Cross-links
Loss of cross-links
F
Kinetochore declustering %
20%
15%
10%
5%
0%
Cross-links
Loss of cross-links

Figure 2.7 Observed coordinated stretching is predicted in simulations with cross-links between adjacent chromatin springs

Cells were labeled with Spc29-RFP (spindle poles), TetO/TetR-CFP at 0.5 kb from CEN 11, and LacO/LacI-GFP 1.8 kb from CEN 15. Wild-type cells exhibit stretching of a single pericentromere LacO in 11% of cells (Stephens et al., 2011) and recapitulated herein (12 ± 3%, n = 261). (A) Cells with two labeled LacO arrays (CEN11, CEN15) exhibit one stretching (uncoordinated, top) or both stretching (coordinated, bottom; WT 40 ± 16 %, n = 45 stretching cells). (B) Coordinated stretching was measured in simulations of a piecewise continuous spring, in which asymmetric stretching can be predicted (Figure 2 C). Chromatin springs were cross-linked with a Hookean spring of increasing strength relative to the chromatin spring constant (0–0.5X = 0–15 pN vs. chromatin spring constant of 30 pN, n = 500 5 experiments of 100). For each cross-linking spring constant the threshold was altered to obtain 12 ± 2% stretching if a single pericentromere was labeled (experimental WT single stretching %). Population simulations were then measured for coordinated stretching of any pair of springs. In the absence of cross-linking (0, Simulated) the predicted frequency of coordinated stretching is 13 ± 4%, less than observed experimentally (left, WT). Cross-linking springs with 0.3X the spring constant of the chromatin spring best match experimental (P = 0.88, 42 ± 22 %, right, vs. WT 40 ± 16 %, left). Loss of cross-linking (0 $k_{cross\text{-}link}$, 955 nm $L_{threshold}$) displays increased spindle length (C), spindle variation (D), pericentromere stretching (E), and kinetochore declustering (F; P < 0.05). Scale bar = 1 μm. Error bars represent standard deviation.

Table 2.2 Comparison of model predictions and experimental outcomes

Attributes	Experimental	Minimal Linear Stochastic	Coupled Linear Stochastic	Coupled Non-Linear Stochastic	Coupled Non-Linear Stochastic + Cross-links
Outward motor force		Poisson	On/off rates	On/off rates	On/off rates
Inward spring force		Hookean	Hookean	Piecewise continuous	Piecewise continuous
kMT dynamics		Gaussian	(Gardner et al., 2005)	(Gardner et al., 2005)	(Gardner et al., 2005)
Spring network		Individual	Individual	Individual	Cross-linked network
Measurable	Perturbation of the chromatin spring				
Spindle length	Increases	Increases	Increases	Increases	Increases
Spindle variation	Increases	Increases	Increases	Increases	Increases
Chromatin stretching	Increases	NM	NM	Increases	Increases
Kinetochore declustering	Increases	NM	Constant	Increases	Increases
Coordinated stretching	~40% WT	Not Predicted	Not Predicted	Not Predicted	Predicted

NM= not measureable

.

$k_{cross\text{-}link}$ = 0.3X yielded the best fit to the observed correlated stretching frequency (P = 0.88, Figure 5 B).

To determine if depletion of cross-linking in the CNLS + cross-linking model could account for experimentally observed behavior, we simulated loss of cross-links. We analyzed spindle length, length variation, loop stretching, and declustering in the CNLS with $k_{cross\text{-}link}$ = 0.3X (WT proxy) and upon depletion of cross-linking springs $k_{cross\text{-}link}$ = 0 (perturbed spring proxy). Upon removing the cross-links spindle behavior was similar to the CNLS model with a decreased threshold. All simulation outputs increased (Figure 2.7, C-F, $P < 0.05$), recapitulating *in vivo* perturbation of the chromatin spring via pericentric cohesin or condensin depletion. Ablation of cross-linking serves as another mechanism to increase loop stretching.

Discussion

The mitotic spindle is a force regulatory machine built for chromosome segregation. Utilizing the mitotic spindle in yeast allows us to investigate the core components to avoid complexities that exist in larger spindles found in mammalian cells. The key features of the machine are an extensional microtubule-based motor force and a restoring chromatin spring force. Tension or microtubule attachment at kinetochores silences the spindle checkpoint in preparation for faithful segregation (Bloom and Yeh, 2010). A major question in the field is how the cell measures tension across an attachment site consisting of multiple kinetochore microtubules. The lack of information regarding the functional properties of the chromatin

spring hinders a mechanistic understanding of how tension is distributed between sister kinetochores in mitosis.

To address the biophysical basis of the chromatin spring, we utilized mathematical models of the yeast spindle. The main experimental features (see Table 2.2) are spindle length and variation, pericentric chromatin stretching and kinetochore clustering. The simplest models containing a linear chromatin spring (noise, MLS; coupled, CLS) capture spindle length and variation but fail to recapitulate the complexities found *in vivo* (Table 2.2). Visualization of a single chromosome using integrated LacO spots revealed asymmetric pericentric chromatin spring behavior during metaphase (Figure 2.3 C and 2.5). LacO spots exhibit dynamic transitions from a focus to an extended state (Figure 2.5). When a LacO spot on one sister stretches, the other sister does not (n = 102; Stephens et al., 2011). These data suggest pericentric chromatin does not function as a linear spring. A simple non-linear spring is a piecewise continuous force-extension rule with a threshold condition for switching between looped and unlooped springs. An alternative form of a non-linear spring is a worm-like chain, with an exponential force-extension curve. Our model exhibits a saw-tooth force-extension curve and recapitulates chromatin stretching and kinetochore declustering (Table 1), not matched by systems with linear springs. A Hookean spring ($F = - k_{spring} (L_{spring} - L_{rest})$) has two adjustable parameters, rest length (L_{rest}) and spring constant (k_{spring}, Figure 2.8 A). The piecewise continuous spring contains a third additional parameter, a threshold ($L_{threshold}$) for determining the state of chromatin looping which alters the linear spring parameters (Figure 2.8 B). An additional fourth parameter is the cross-linking spring constant ($k_{cross\text{-}link}$, Figure 2.8 C) invoked to fit experimental data of 40% coordinated stretching (Figure 2.7 B,

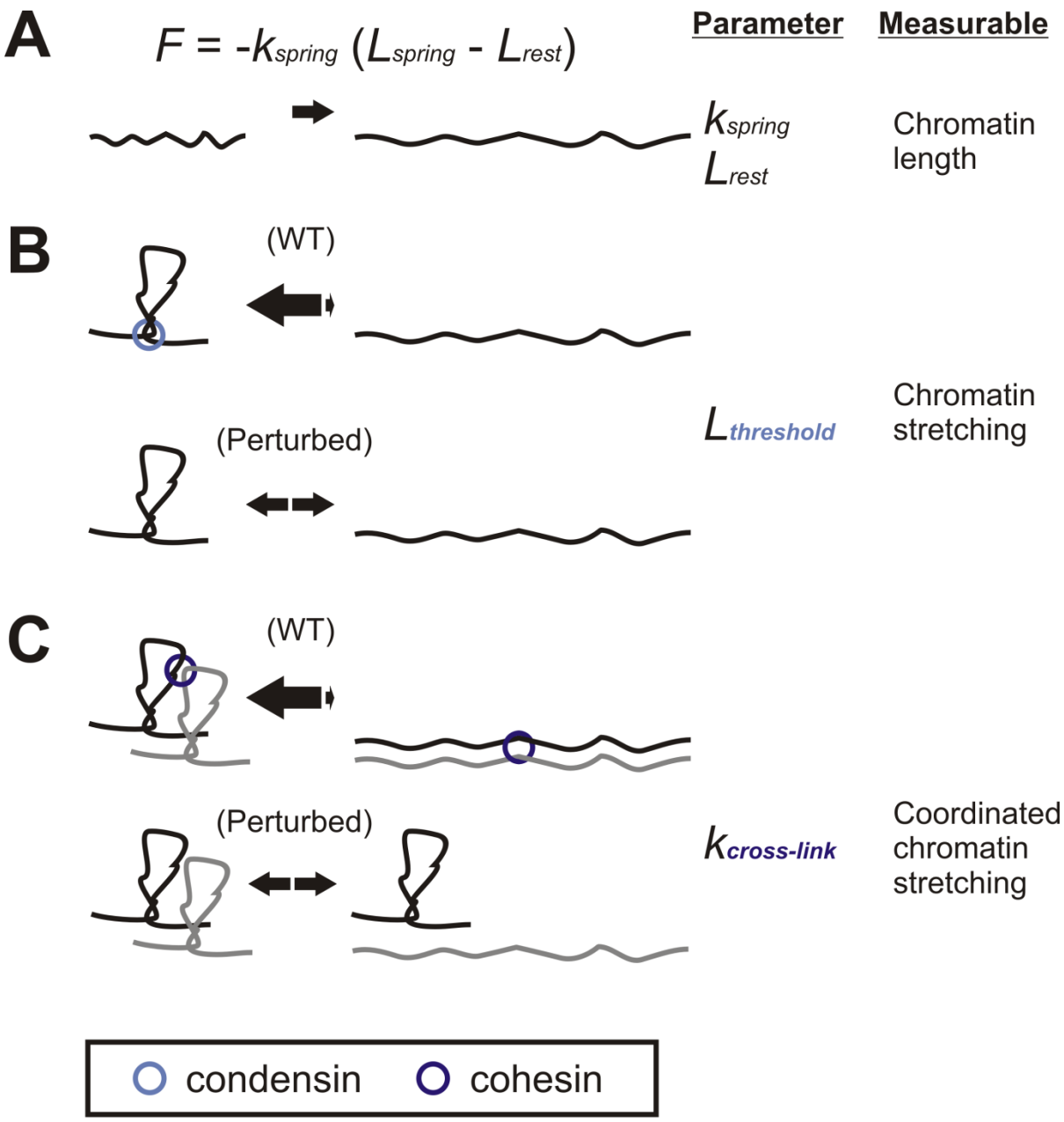
A
F = -kspring (Lspring - Lrest)
Parameter
Measurable
kspring
Lrest
Chromatin length
B
(WT)
(Perturbed)
Lthreshold
Chromatin stretching
C
(WT)
(Perturbed)
kcross-link
Coordinated chromatin stretching
condensin
cohesin

Figure 2.8 Testable Parameters of a Piecewise Continuous Spring

(A) The most common form of a spring is given by a Hookean spring equation $F = -k_{spring}$ ($L_{spring} - L_{rest}$) where k is the spring constant, and L_{rest} is the spring rest length. Simulations of a linear spring fail to account for behavior of the spindle and the pericentric chromatin upon experimental depletion of pericentric cohesin or condensin (see Table 2.2). (B) A non-linear spring with a threshold length ($L_{threshold}$) recapitulates increase in spindle length and fluctuations, asymmetric chromatin stretching and kinetochore declustering. The threshold represents the length/force at which a compact loop transitions to a stretched loop. Cohesin and condensin increase the threshold of the chromatin loops maintaining compaction (equilibrium arrows shifted towards loops). Perturbation of the chromatin spring through depletion of pericentric cohesin or condensin decreases the length/force the loops can resist causing the loops to stretch freely (equal amounts of compact and stretched loops, Figure 2.3, A and C). The $L_{threshold}$ variable is an alternative way to modulate the native linear spring constant (k) and rest length (L_{rest}). (C) Experimentally observed stretching of two chromosomes could be simulated through the addition of a cross-linking spring between neighboring chromosomes ($k_{cross\text{-}link}$, Figure 2.7). Cross-linked chromatin springs can distribute tension, thereby increasing the ability of a single chromatin spring to resist reaching $L_{threshold}$ or extreme stretching (equilibrium arrows shifted towards the looped state). Simulation and experimental data suggests condensin and cohesin modulate $L_{threshold}$ and $k_{cross\text{-}link}$, respectively.

WT). The cross-linking spring parameter affects both the threshold and linear spring parameters. These additional model parameters provide new functional attributes for probing the role of chromatin proteins such as cohesin and condensin in organizing pericentric chromatin into higher-order loops that function as a spring.

The physical basis for a system with spring extension thresholds is consonant with chromatin loops in the pericentric region. The evidence for chromatin loops is two-fold. One is the transition from spots to linear arrays of pericentric DNA visualized with LacO; two is the spatial redistribution from a spindle distal to proximal position coincident with the spot to linear transition (Stephens et al., 2011). The enrichment of cohesin and condensin and their ability to bring distal regions of chromatin into proximity (Hirano, 2006; Nativio et al., 2009; Mishra et al., 2010) provides additional evidence for pericentric chromatin loops. Pericentric condensin is localized proximal to the spindle axis and is responsible for axial compaction in accord with the SMC complex dictating the $L_{threshold}$ parameter (Figure 2.8 B). Pericentric cohesin's distal localization from the spindle axis and role in radial confinement of the pericentric chromatin best fits with the depicted $k_{cross\text{-}link}$ parameter (Figure 2.8 C; Stephens et al., 2011). The depiction of cohesin and condensin in Figure 6 accounts for their spatial segregation in the pericentromere, different biochemical roles, and common effect on the spindle and spring looping behavior both experimentally and in simulations. Therefore, we propose that cohesin and condensin together with pericentric DNA form a non-linear spring that is part of a cross-linked network in the pericentromere. A similar cross-linked network mechanism for constraint of mammalian mitotic chromosomes has been attributed to protein-mediated compaction, linking and DNA entanglements (Kawamura et al., 2010; Sun et al., 2011). Cross-linking between kinetochores and/or kinetochore microtubules could also

contribute to such a mechanism. Condensin and cohesin function to adjust chromatin compaction and provide a mechanism to distribute tension across single and multiple microtubule attachments in the spindle.

The organization of pericentric chromatin loops into a cross-linked network provides new insights into mechanisms of tension sensing in mitosis. The force exerted at the point of microtubule attachment is unlikely to be distributed uniformly between sister microtubule attachment sites. It is unclear how tension is sensed at a multi-microtubule attachment site such as the mammalian kinetochore (16-20 microtubules), or the clusters of 16 yeast kinetochores, with stochastic microtubule dynamics. Alternatively, the cross-linking model provides a mechanism whereby the sum of forces from a multi-attachment site structure can be integrated. When tension is applied to a cross-linked network, the heterogeneous distribution of cross-links can lead to local regions of high stress (Panyukov et al., 2009). Slip rings (or molecular pulleys) provide a mechanism to distribute tension from one location to the entire network (Okumura and Ito, 2001; Granick and Rubinstein, 2004). Cohesin and condensin have the physical attributes to function as slip rings (Glynn et al., 2004; Lengronne et al., 2004; Cuylen et al., 2011; Hu et al., 2011) and provide the chemistry for regulating elasticity both within the centromere and across multiple attachment sites. Upon the loss or depletion of these proteins pericentric chromatin and tension sensing is impaired in both yeast (Yong-Gonzalez et al., 2007; Ng et al., 2009) and mammals (Ribeiro et al., 2009; Samoshkin et al., 2009; Uchida et al., 2009; Manning et al., 2010). We propose that a chromatin network composed of SMC “tension adjusters” functions to equalize tension across sister kinetochores, whose microtubule attachment sites exhibit stochastic dynamics throughout early mitosis.

Materials and methods

Cell preparation

Cells were incubated in YPD (2% glucose, 2% peptone, and 1% yeast extract) at 24°C or 32°C for wild-type or *mcm21Δ* strains. Asynchronous cultures were grown to log phase then imaged. Only metaphase cells were analyzed as outlined in (Stephens et al., 2011). Cells were considered in metaphase with separated Nuf2 kinetochore foci and not linearly increasing in spindle length (indicative of anaphase). Cells with pericentric LacO and TetO were considered in metaphase when sister arrays were separated (LacO and TetO) and not linearly increasing in separation distance.

Imaging

Wide field microscope images were acquired at room temperature (25°C) using a Nikon Eclipse TE2000-U (Nikon, East Rutherford, NJ, USA) microscope stand with a 100X Plan Apo 1.4 NA digital interference contrast (DIC) oil immersion lens with an Orca ER Camera (Hamamatsu Photonics K.K., Hamamatsu City, Japan). MetaMorph 7.1 (Molecular Devices, Downington, PA, USA) was used to acquire un-binned z-series image stacks with z-step size of 300 nm. Population Imaging was carried out in water on ConA coated cover slips. Live-imaging of cells was carried out on 25% gelatin slab with yeast complete (YC) 2% glucose media. Image exposure times were between 400-800 ms.

Analyzing pericentric LacO array stretching

LacO/lacI-GFP strains were grown in SD-His media to induce lacI-GFP under the *HIS* promoter as outlined by (Goshima and Yanagida, 2000; Pearson et al., 2001). LacO array strains used to determine rate of chromatin stretching and shrinkage KBY 9039

(*mcm21Δ*) LacO 6.8 kb centroid from CEN15 (10 kb array inserted at 1.8 kb from CEN15). Time-lapse images of LacO/lacI-GFP stretching with Spc29-RFP labeled spindle poles in KBY 9039 were captured using un-binned (65 nm/pixel) single plane acquisitions at 5 second intervals. Each single plane image was rotated using MATLAB to align all spindles axis horizontally along the same y coordinate. Images were deconvolved using Huygens Compute engine 4.1.0 (Scientific Volume Imaging, Hilversum, Netherlands) and background was subtracted using MetaMorph. The length of the focus and stretched LacO/lacI-GFP signal were measured inclusively in MetaMorph and logged into Excel (Microsoft Corporation, Redmond, WA, USA). A compact spot exhibits an isotropic shape, parallel and perpendicular to the spindle axis, and a stretched spot is anisotropic, extended parallel to the spindle axis (Stephens et al., 2011). An aspect ratio (parallel/perpendicular) of greater than 1.2 is a quantitative measure of anisotropy (Haase et al., 2012). Extended arrays are at least 600nm in length along the spindle axis (see Figure 2.5 A; aspect ratio of 1.2).

Kinetochore declustering

Population images were acquired of strains containing a kinetochore marker (Nuf2, Ndc80, or Ame1) with labeled spindle poles (Spc29). KBY 8526 473A Nuf2-GFP-Ura Spc29-RFP-Hb; KBY 9413, 473A, Ndc80-tdtomato-Nat, Ame1-GFP-Kan; KBY 9070, 473A, *mcm21Δ*-Nat, Nuf2-GFP-Ura, Spc29-RFP-Hb; KBY 9423, 473A, *mcm21Δ*–Nat, Nat::Trp, Ndc80-tdtomato-Nat, Ame1-GFP-Kan. MetaMorph line scans were drawn along the spindle axis through the kinetochores to determine if each sister kinetochore structure remain clustered as one peak or declustered into multiple peaks.

Simulation output of spindle length and the length of each of the 32 kinetochore microtubules emanating from each pole (16 each) were converted into XML files for

generating simulated fluorescent images. A CSV to XML converter script was used in MATLAB to import the lengths into a set geometry to be used for the Microscope Simulator 2.1.1 (CISMM UNC-Chapel Hill) (Quammen et al., 2008). For each pole the 16 corresponding kinetochore microtubules were arranged in a 250 nm diameter around the spindle pole axis. The spindle pole was marked by an oblong sphere and labeled purple. The plus-end of each of the kinetochore microtubules (rods) was marked with a small sphere labeled green. The Microscope Simulator convolved the image using the point-spread function of our microscope as outlined by (Sprague et al., 2003). The simulated image was configured to match experimental signal to noise (410 max, 270 min) and background noise standard deviation (±4.8) using a gain, offset, and Gaussian noise functions. The simulated images were then analyzed in MetaMorph the same as experimental images outlined in the previous paragraph.

Coordinated stretching

To build a strain with pericentric regions labeled on two different chromosomes, we incorporated a 10 kb TetO array 0.4 kb away from the centromere at the met14 locus of CEN 11 using a plasmid targeting protocol (Rohner et al., 2008) into a strain that already contained a 10 kb LacO array tagged with LacI-GFP 1.8 kb from CEN 15. TetR-CFP (pDB49: TetR-CFP-Hb) was used to tag the TetO array. Spindle pole bodies were marked with Spc-29-RFP. Images were acquired using Metamorph and were obtained in z series stacks of ten images with a step size of 200 nm. Images were binned 2x2 (pixel size of 130 nm). A triple pass dichroic was used in conjunction with YFPg, CFP and RFP excitation filters, no detectable bleed-through was found. LacO and TetO array stretching was analyzed in metaphase cells with two separated arrays for both the LacO and TetO. Stretching events

were determined as previously explained in the subsection *Analyzing pericentric LacO array stretching*.

Simulation population outputs were analyzed for uncoordinated or coordinated stretching amongst all 16 chromosomes.

Mitotic spindle simulation

The Mitotic Spindle Simulation software, written in MATLAB/Simulink, along with an accompanying manual can be downloaded at *JCB* or the CISMM UNC-Chapel Hill website.

Minimal linear stochastic (MLS) model

This minimal model considers prescribed stochastic cellular forces, a linear chromatin spring, and viscous drag, each of them acting along the spindle axis. Thus a force balance along the spindle axis includes the extensional motor force from double bound motors, F_{ip} (+); the chromatin spring restoring force, F_k (-); and, the drag force opposing spindle movement, F_{drag}:

$$\sum F_{on\ spindle\ axis} = F_{ip} + F_k + F_{drag} = 0. \qquad \textbf{Eqn. A1}$$

1) Force Laws

a) The drag force is given by Stokes' drag law:

$$F_{drag}(t) = -C_{drag}\, V_{ip}(t), \qquad \textbf{Eqn. A2}$$

where V_{ip} is the velocity of the interpolar microtubules.

Table 2.3 MLS model parameters

Parameter	Notation	Default value
Spring constant	k_{sp}	22 pN/μm
Drag coefficient	C_{drag}	30 pN-s/μm
Motor detachment rate	K_{off}	0.25 motors/s
Motor attachment rate	K_{on}	0.5 motors/s
Mean of L_{kMT}	L_m	0.4 μm
Standard deviation of L_{kMT}	σ_m	0.088 μm
Spring rest length	ℓ_r	0.2 μm

b) The motor force from double bound motors is additive:

$$F_{ip}(t) = F_M\, D(t), \qquad \textbf{Eqn. A3}$$

where F_M is the force per motor and $D(t)$ is the number of double bound motors. Stall forces determined experimentally are in the range ~5.5–7.5 pN, depending upon ATP concentration (Visscher et al., 1999). In this study F_M is assumed constant and equal to 6 pN. For this minimal model, we posit $D(t)$ as a Poisson distribution with given rates of attachment and detachment, k_{on} and k_{off}. This assumption on the number of motors is equivalent to a population balance of motors, where the only species are double bound and unbound motors,

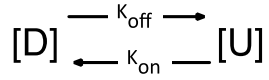

c) The length of the kinetochore microtubules (kMTs) is normally distributed with mean L_m and variance σ_m:

$$L_{kMt}^{\text{left,right}} \sim \mathcal{N}(L_m, \sigma_m). \qquad \textbf{Eqn. A4}$$

d) The restoring force from chromatin is that of a Hookean (linear) spring:

$$F_k(t) = -k_{sp}\left(L_{ip}(t) - L_{kMT}^{\text{left}}(t) - L_{kMT}^{\text{right}}(t) - L_{rest}\right), \qquad \textbf{Eqn. A5}$$

where $L_{rest} = 200$ nm is the rest length of the spring.

Introducing these assumptions into Eqn. A1, solving for V_{ip}, and then writing V_{ip} as the discrete rate of change of the spindle length, $L_{ip}(t)$, we find:

$$V_{ip}(t) = \frac{1}{C_{drag}}\left(F_M D(t) - k_{sp}\ \left(L_{ip}(t) - L_{kMt}^{\text{left,right}}(t) - L_{rest}\right)\right) \quad \textbf{Eqn. A6}$$

$$\frac{L_{ip}(t+\Delta t) - L_{ip}(t)}{\Delta t} = V_{ip}(t+\Delta t). \quad \textbf{Eqn. A7}$$

Finally, solving for $L_{ip}(t+\Delta t)$ gives

$$L_{ip}(t+\Delta t) = \frac{C_{drag}}{C_{drag} + k_{sp}\,\Delta t} L_{ip}(t) \quad \textbf{Eqn. A8}$$
$$- \frac{\Delta t}{C_{drag} + k_{sp}\,\Delta t}\left(L_{kMt}^{\text{left,right}}(t+\Delta t) + L_{rest} - F_M D(t+\Delta t)\right).$$

Note that here we can use values of $L_{kMt}^{\text{left,right}}$ and D at time $t+\Delta t$, since these quantities are independent of the spindle length. A typical solution of Eqn. A8 is plotted in Figure S1 D and Table S4 shows the parameters of the MLS model and the default values used in our simulations.

Distribution of $L_{ip}(t)$ calculated using the MLS model follows a log-normal distribution. A variable X is said to be log-normally distributed if $\log(X)$ is normally distributed. While in a normal distribution the effects of independent factors are additive, the effects of independent factors acting on a log-normally distributed variable are multiplicative, and log-normal distributions usually refer to variables that remain positive.

Coupled Linear Stochastic (CLS) model

1. Motor Dynamics

Rather than simply draw the number of double bound motors, D(t), from a Poisson distribution parameterized by k_{on} and k_{off}, we now distribute the total number of motors among four species: S_{ipMT} for motors single bound to the interpolar microtubules (ipMTs), S_{kMT} for motors single bound to the kMTs, U for unbound or free motors, and D for double bound motors in the ipMT overlap zone.

The population dynamics is summarized in the figure below, rates given in 1/s.

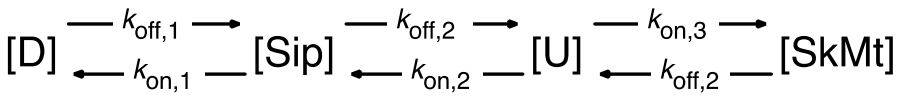

For each simulation the total motor pool $D + S_{ip} + U + S_{kMT}$ is constant. Table 2.4 summarizes the assumptions made on the different rates of detachment and attachment.

(a) The dynamics of attachment of single bound motors in ipMTs to become double bound motors is assumed to follow a binomial process,

$$S_{ipMT} \rightarrow D \sim B(S_{lap}, 0.12), \qquad \textbf{Eqn. B1}$$

where S_{lap} is the number of motors in the overlap region L_{lap}, of ipMTs,

$$S_{lap} = S_{ipMT} \cdot \frac{2L_{lap}}{L_{ip} + L_{lap}},$$

where our simulations assume $L_{lap} = 0.8$ μm. An estimated overlap zone labeled with Ase1-GFP reveals length changing proportional to spindle length (Figure 2.9).

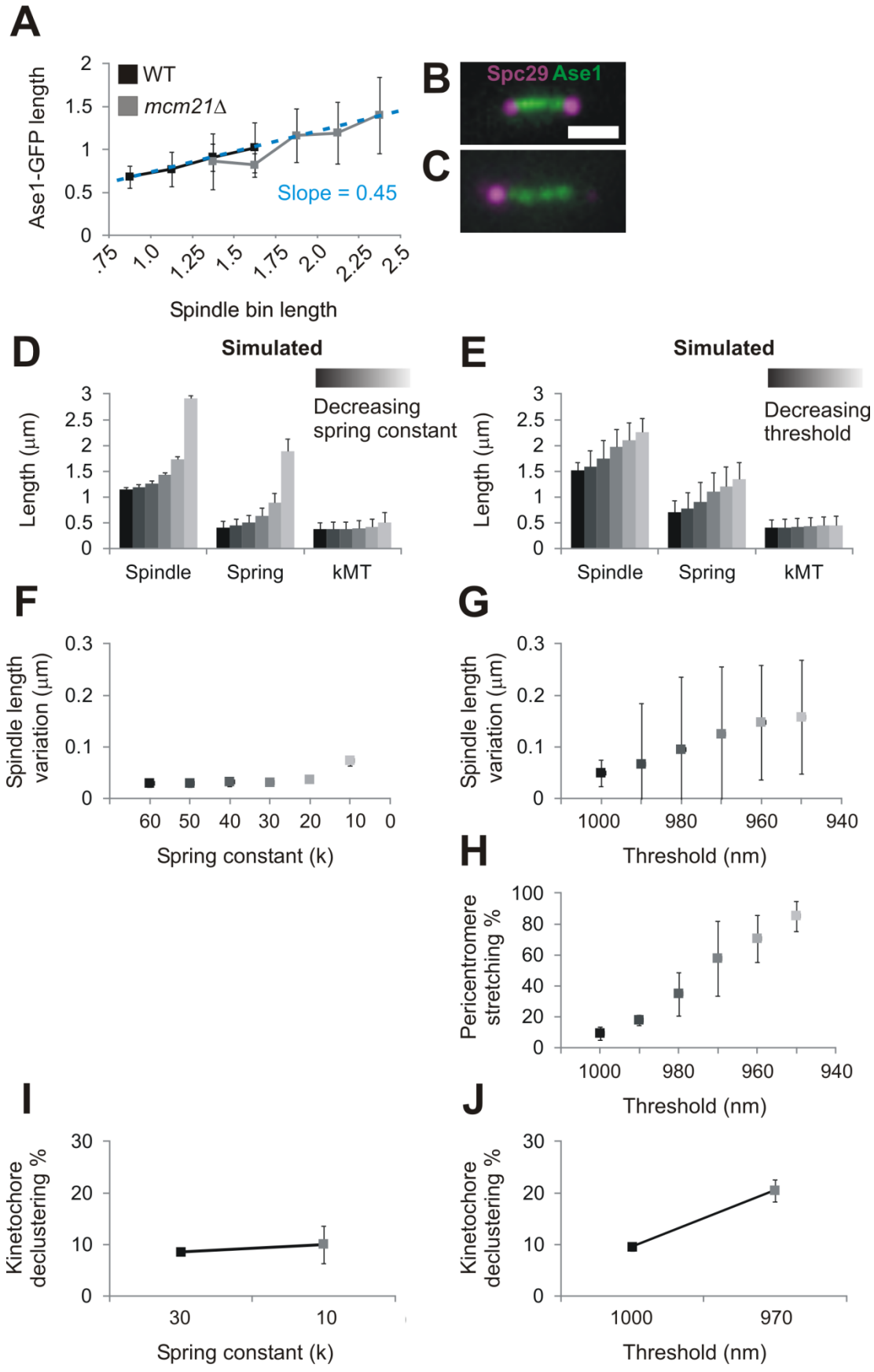
A
WT
mcm21Δ
Ase1-GFP length
Slope = 0.45
Spindle bin length
B
Spc29 Ase1
C
D
Simulated
Decreasing spring constant
Length (μm)
Spindle
Spring
kMT
E
Simulated
Decreasing threshold
Length (μm)
Spindle
Spring
kMT
F
Spindle length variation (μm)
Spring constant (k)
G
Spindle length variation (μm)
Threshold (nm)
H
Pericentromere stretching %
Threshold (nm)
I
Kinetochore declustering %
Spring constant (k)
J
Kinetochore declustering %
Threshold (nm)

Figure 2.9 The model is insensitive to overlap dynamics

(A) Length of the Ase1-GFP signal for increasing spindle lengths in wild-type (black, $n = 51$) and *mcm21Δ* (gray, $n = 46$) spindles. Ase1-GFP signal increases proportionally with spindle length with a slope of 0.45 (dotted blue line). Example images of (B) wild-type and (C) *mcm21Δ* spindles labeled with Ase1-GFP (green) and Spc29-RFP (purple). Simulations were run for the linear (CLS model, left column D, F, and I) and piecewise (CNLS model, right column E, G, H, and J) with increasing overlap zone dynamics from A. Spindle length (D and E), spindle variation (F and G), pericentromere stretching (H), and declustering (I and J) showed similar trends compared to constant overlap zone (see Figure 2.3, B and C; CLS and CNLS models, respectively). Error bars represent standard deviation. Scale bar = 1 μm.

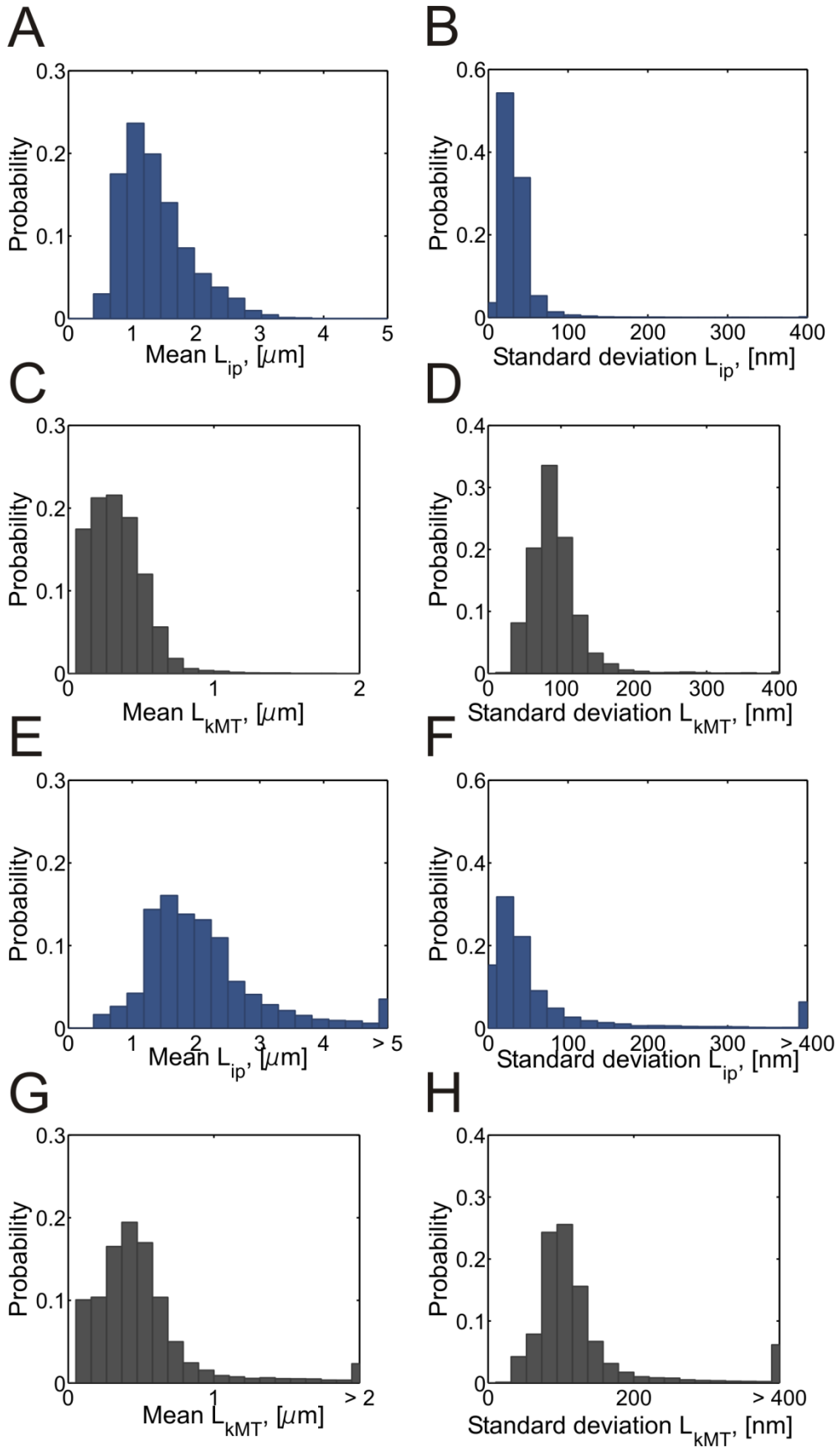
A
Probability
0.3
0.2
0.1
0
0 1 2 3 4 5
Mean L_{ip}, [μm]
B
Probability
0.6
0.4
0.2
0
0 100 200 300 400
Standard deviation L_{ip}, [nm]
C
Probability
0.3
0.2
0.1
0
0 1 2
Mean L_{kMT}, [μm]
D
Probability
0.4
0.3
0.2
0.1
0
0 100 200 300 400
Standard deviation L_{kMT}, [nm]
E
Probability
0.3
0.2
0.1
0
0 1 2 3 4 > 5
Mean L_{ip}, [μm]
F
Probability
0.6
0.4
0.2
0
0 100 200 300 > 400
Standard deviation L_{ip}, [nm]
G
Probability
0.3
0.2
0.1
0
0 1 > 2
Mean L_{kMT}, [μm]
H
Probability
0.4
0.3
0.2
0.1
0
0 200 > 400
Standard deviation L_{kMT}, [nm]

Figure 2.10 Model sensitivity analysis reveals robustness of the model

Values for the seven parameters are chosen randomly within each corresponding interval outlined in Table 2.5. 10000 random searches were performed using the CNLS with cross-links model with either a constant (A-D) and increasing (E-H) overlap region (L_{lap}). Histograms of spindle length (L_{ip}) (A, E) mean and (B, F) standard deviation and kinetochore microtubules (L_{kMT}) length (C, G) mean and (D, H) standard deviation are shown. Clustering of spindle lengths in the histograms indicate that model predictions are tolerant to variations over wide intervals of parameter space. Spindle lengths greater than 3 μm are considered as outliers. Sensitivity analysis of a model with a constant overlap zone generated outliers in less than 1% of simulations (74 out of 10000) while a model with an overlap zone that increases proportionally with spindle length (Figure 2.9) generated outliers in ~14% of simulations (1379 out of 10000).

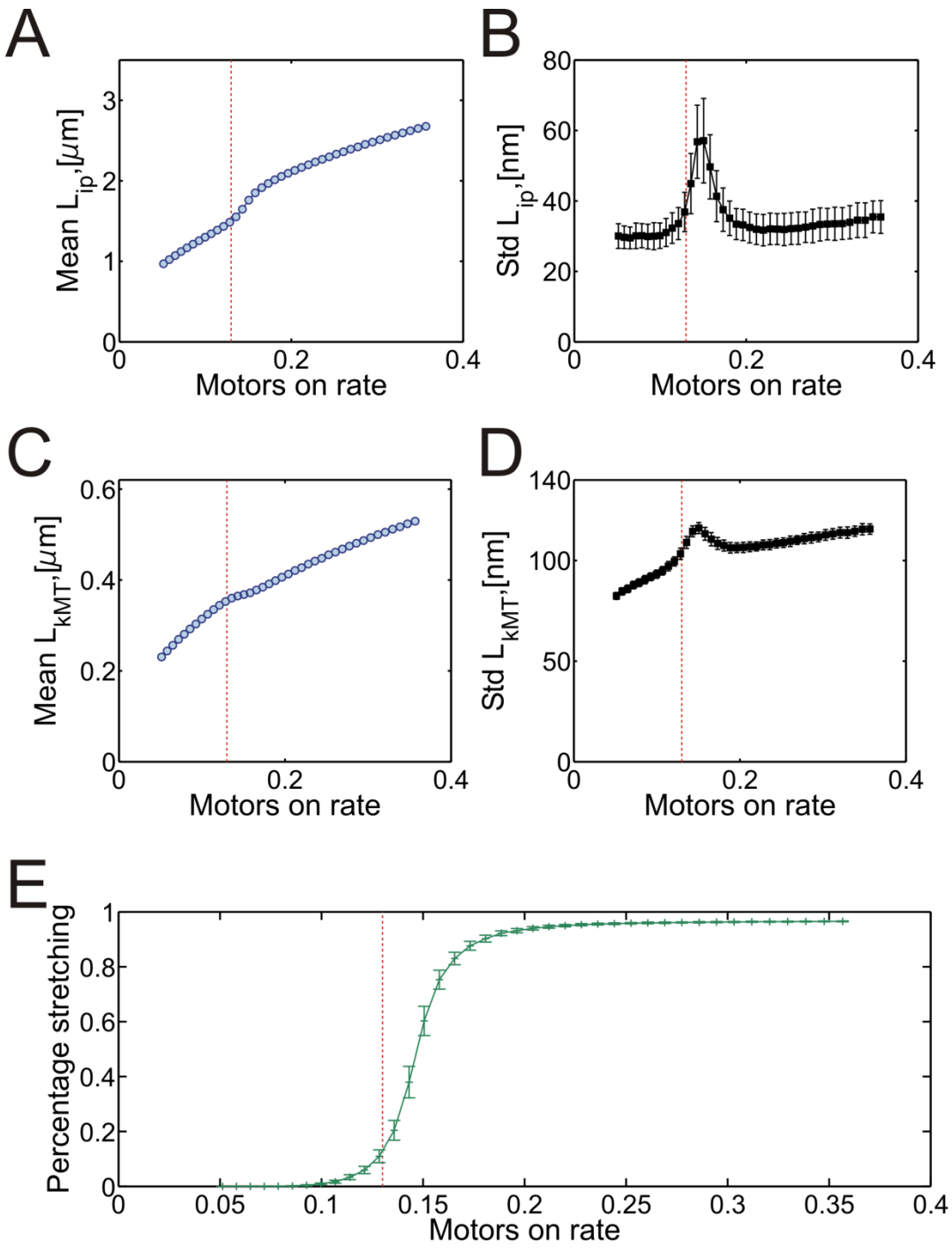
A
Mean L_{ip},[μm]
Motors on rate
B
Std L_{ip},[nm]
Motors on rate
C
Mean L_{kMT},[μm]
Motors on rate
D
Std L_{kMT},[nm]
Motors on rate
E
Percentage stretching
Motors on rate

Figure 2.11 The threshold for loop stretching disproportionally affects spindle length variation

An example of single parameter analysis for the CNLS with cross-links model. The effect of changing motor on rate on (A) mean spindle length, (B) standard deviation of spindle length, (C) mean kMT length, (D) standard deviation of kMT length, and (E) loop stretching. Red line denotes wild-type default values. Spindle length varies monotonically with motor on rate. As expected, the addition of motors increases the extensional force and therefore spindle length increases. In contrast, the standard deviation of spindle and kMT length is not monotonic (B, D). A peak in standard deviation is coincident with threshold values where 50% of the springs are stretched (E). This indicates that the threshold value is a sensitive parameter in the model.

Table 2.4 Motor on/off rates

Description		Dependence	Value	Notes
$\boldsymbol{k_{on,1}}$**:**	Attachment rate of single bound motors to ipMTs	Constant	$0.13s^{-1}$	(a)
$\boldsymbol{k_{on,2}}$**:**	Attachment rate of unbound motors to ipMTs	$L_{ip}, L_{kMt}^{\text{left,right}}$		(b)
$\boldsymbol{k_{on,3}}$**:**	Attachment rate of unbound motors to kMTs	$L_{ip}, L_{kMt}^{\text{left,right}}$		(b)
$\boldsymbol{k_{off,1}}$**:**	Detachment rate of double bound motors	Constant	$0.3\ s^{-1}$	(c)
$\boldsymbol{k_{off,2}}$**:**	Detachment rate of single bound motors	Constant	$0.3\ s^{-1}$	(c)

a,b,c refer to Materials and methods subsection *Motor dynamics*

.

Table 2.5 Model sensitivity analysis parameters

Parameter	Default	Min	Max	Eqn.
MT rescue rate, [1/s]	0.017	0.010	0.030	
MT catastrophe rate, [1/s]	0.025	0.015	0.035	
Single to double on rate, [1/s]	0.130	0.005	0.160	
Double to single off rate, [1/s]	0.300	0.200	0.400	
Overlap length constant, C_0, [μm]	0.800	0.500	1.000	$L_{lap} = C_0$
	0.500	0.300	0.700	$\Delta L_{lap} = C_0\, \Delta L_{ip}$
Rescue probability, C_1	1.000	0.200	1.800	$p_r = 0.21 - C_1 \times 9.5 F_k$
Catastrophe probability, C_1				$p_c = 0.27 + C_1 \times 0.442\ (L_{kMT} - 0.34)$

Sensitivity analysis of a model with a constant vs. dynamic overlap zone reveals similar results (Figure xxx). Sensitivity analysis reveals that models with a constant overlap zone are more robust and thus were used throughout the simulations (Figure 2.10). In addition, the probability of success is constant and equal to 12%. Since the relation between the probability of attachment, p_{on}, and the rate of attachment, $k_{\mathrm{on},1}$, is

$$p_{on} = 1 - e^{-k_{\mathrm{on},1}}, \qquad \textbf{Eqn. B2}$$

we find $k_{\mathrm{on},1} \approx 0.13$.

(b) The rate of attachment of free motors to ipMTs and kMTs is assumed to be proportional to the tubulin concentration (constant) and the percentage of the total length that is available for attachment,

$$k_{\mathrm{on}.2} = [\mathrm{tubulin}] \times \frac{L_{ip} + L_{lap}}{L_{ip} + L_{lap} + L_{kMt}^{\mathrm{left}} + L_{kMt}^{\mathrm{right}}}, \qquad \textbf{Eqn. B3}$$

$$k_{\mathrm{on}.3} = [\mathrm{tubulin}] \times \frac{L_{kMt}^{\mathrm{left\ or\ right}}}{L_{ip} + L_{lap} + L_{kMt}^{\mathrm{left}} + L_{kMt}^{\mathrm{right}}}. \qquad \textbf{Eqn. B4}$$

(c) The rate of detachment of bound motors is assumed constant,

$$k_{\mathrm{off},2} = k_{\mathrm{off},1} = 0.3\ s^{-1}. \qquad \textbf{Eqn. B5}$$

2. Kinetochore Microtubule Length Dynamics

The kMTs grow and shrink stochastically through polymerization and depolymerization, but the process is biased by the state of the kMTs, i.e. their length relative to a threshold length and the tension in the kMTs. The dynamics of this process was studied by Gardner et al., (2005) and probability of switching states is graphed in Figure 2.2 A.

Fitting to Gardner *et al.* data gives the following relationships for the probabilities of rescue, p_r, and catastrophe, p_c,

$$p_r = |0.21 - 9.5 \cdot F_k| \qquad \textbf{Eqn. B6}$$

$$p_c = |0.38 - 0.65\,(L_{kMT} - 0.75)^2|. \qquad \textbf{Eqn. B7}$$

In addition, if $L_{kMT} < 50$ nm, $p_r = 1$ and if $L_{kMT} > 800$ nm, $p_c = 0.389$.

In Eqns. B6 and B7 F_k is given in pN and L_{kMT} in microns. To find if at a given time step a kinetochore microtubule is growing or shortening, the following procedure is implemented.

i. Two random numbers, r_c and r_r, are drawn from a uniform distribution

ii. r_c and r_r are used to compute two logical values, a_1 and a_2, as

$$a_1 = \begin{cases} 0 & \text{if } p_c < r_c \\ 1 & \text{if } p_c > r_c \end{cases} \qquad a_2 = \begin{cases} 0 & \text{if } p_r < r_r \\ 1 & \text{if } p_r > r_r \end{cases}$$

iii. Changes in kMT length are then determined by the rule:,

$a_1 = 0$; $a_2 = 0$ – Do nothing

$a_1 = 0$; $a_2 = 1$ – Rescue (at a rate of 17 nm/s)

$a_1 = 1$; $a_2 = 0$ – Catastrophe (at a rate of 25 nm/s)

$a_1 = 1$; $a_2 = 1$ – Same as previous time step

3. Coupled dynamics of 16 chromatin springs

In this model, we include the dynamics of all 16 chromatin springs and their corresponding kMTs. Furthermore, we assume the springs are arranged in parallel so that the total spring force, F_k, is the sum of individual spring forces,

$$F_k = \sum_{n=1}^{16} F_{k,n}. \qquad \textbf{Eqn. B8}$$

The consequences of including more than one spring in the spindle dynamics are shown in Figure 2.2, E-F and discussed in the results subsection *A linear spring model recapitulates the increase in both the mean and variance of spindle length observed in mutant cells.*

Force – Velocity relationship of the Interpolar Microtubules

We impose a linear force-velocity relationship defined by two parameters: a maximum (stall) force, $F_M = 6$ pN, and a maximum speed, $V_{max} = 50$ nm/s. The net force (sum of forces) felt by double bound motors on ipMTs is,

$$F_{net} = F_{ip} + F_k + F_{drag}, \qquad \textbf{Eqn. B9}$$

which is then distributed evenly across double bound motors and gives an mean force per motor,

$$\frac{F_{net}}{D} = \frac{F_{ip} + F_k + F_{drag}}{D} = \frac{F_M D + F_k + F_{drag}}{D}$$
$$F_{\text{per motor}}(t) = F_M + \frac{F_k(t) + F_{drag}(t)}{D(t)}. \qquad \textbf{Eqn. B10}$$

The interpolar microtubule (therefore spindle) velocity can be determined as,

$$V_{ip}(t) = \frac{F_{net}(t)}{D(t)} \cdot \frac{V_{max}}{F_M} = V_{max}\left(1 + \frac{F_k(t) + F_{drag}(t)}{F_M D(t)}\right). \qquad \textbf{Eqn. B11}$$

From Eqn. B11 we see that:

- If $F_k + F_{drag} = 0$, then $V_{ip} = V_{max}$. In other words, if the forces from the chromatin spring and fluid drag cancel, the spindle will move at the maximum speed of one motor.
- If the net force on the ipMTs is zero, $F_{net} = 0$, then $V_{ip} = 0$ and the spindle is stationary. In this quasi-equilibrium condition, each motor is at or near stall force (6 pN) and this force arises from the spring and drag forces acting on the motors.
- The mean force acting on a motor can be found as $F_{per\ motor} = F_M\left(1 - V_{ip}/V_{max}\right)$ as shown in Figure 2.2 B.

4. Numerical Integration

With these new dynamics, $L_{ip}(t + \Delta t)$ can no longer be solved explicitly since $D(t + \Delta t)$ and $L_{kMt}^{\text{left,right}}(t + \Delta t)$ depend on $L_{ip}(t + \Delta t)$. Solving Eqn. B12 for the spindle velocity gives,

$$V_{ip}(t) = \left(\frac{V_{max}}{F_M D(t) + V_{max} C_{drag}}\right) \cdot \left(F_M D(t) + F_k(t)\right), \qquad \textbf{Eqn. B12}$$

so that,

$$V_{ip}(t) = \left(\frac{V_{max}}{F_M D(t) + V_{max} C_{drag}}\right) \times \left(F_M D(t) - k_{sp}\left(L_{ip}(t) - L_{kMT}^{\text{left}}(t) - L_{kMT}^{\text{right}}(t) - L_{rest}\right)\right).$$

To integrate this equation in time and find $L_{ip}(t + \Delta t)$, we perform a predictor-corrector scheme. The spindle length in the predictor step, $L_{ip}(t^*)$, is calculated as,

$$L_{ip}(t^*) = L_{ip}(t) + \Delta t\, V_{ip}(t). \qquad \textbf{Eqn. B13}$$

After this predictor step, we use $L_{ip}(t^*)$ to find $D(t^*)$ and $L_{kMt}^{\text{left,right}}(t^*)$, and perform a corrector step,

$$L_{ip}(t+\Delta t) = L_{ip}(t) + \frac{\Delta t}{2}\left[V_{ip}(t) + V_{ip}(t^*)\right], \qquad \textbf{Eqn. B14}$$

where,

$$V_{ip}(t^*) = \left(\frac{V_{max}}{F_M D(t^*) + V_{max} C_{drag}}\right) \times \left(F_M D(t^*) - k_{sp}\left(L_{ip}(t^*) - L_{kMT}^{\text{left}}(t^*) - L_{kMT}^{\text{right}}(t^*) - L_{rest}\right)\right).$$

Finally, from Eqn. B10 is clear that the CLS model no longer imposes a deterministic force-balance as in the MLS model (Eqn.A1). In contrast, the sum of all forces is a stochastic variable, F_{net}, that fluctuates around zero, as shown in Figure 2.2 C.

Coupled Nonlinear Stochastic (CNLS) model

In this model we assume a *nonlinear spring force*, as explained in the results subsection *A non-linear spring hypothesis*. In this new spring force, we posit a threshold value for the spring extension. Spring lengths above the threshold value (X_{thres}) result in a decreased spring constant and increase in rest length. This new spring force can be then written as,

$$F_k = \begin{cases} -k_{sp}\left(L_{sp} - L_{r\,1}\right), & L_{sp} < X_{thres} \\ -\left(\dfrac{L_1}{L_1 + x_{loop}}\right) k_{sp}\left(L_{sp} - L_{r\,2}\right), & L_{sp} \geq X_{thres} \end{cases} \qquad \textbf{Eqn. C1}$$

Here we assume x_{loop} and L_1 to be constants and equal to 450 nm and 800 nm, respectively, which gives$k_2 = 0.64\, k_1$. We recognize that the instantaneous switching between spring states may be more accurately modeled using Kramers' theory. This theory

describes the transition between bistable states as motions over a potential energy barrier. However for the purposes of this model the course-grained switching has proven sufficient to capture our experimental observations.

Coupled Nonlinear Cross-linked Stochastic (CNCLS) model

The sixteen springs are arranged in parallel and linked to their two nearest neighbors. The links are assumed to be soft linear springs with spring constant $k_{\text{cross-link}} = 0 - 15$ pN/μm. Furthermore the springs are assumed to be close enough to each other so that the force law in each link is given by,

$$\mathrm{F}_{\mathrm{cross-link}}|_{\mathrm{n+1}} = -\mathrm{k}_{\text{cross-link}}\left[\left(\mathrm{L}_{\mathrm{spr}} - \mathrm{L}_{\mathrm{spr}}\big|_{\mathrm{n+1}}\right)\cos(\theta)\right],$$

$$\mathrm{F}_{\mathrm{cross-link}}|_{\mathrm{n-1}} = -\mathrm{k}_{\text{cross-link}}\left[\left(\mathrm{L}_{\mathrm{spr}}\big|_{\mathrm{n-1}} - \mathrm{L}_{\mathrm{spr}}\right)\cos(\theta)\right],$$

here θ is the angle between a crosslink and a spring, and we assumed that adjacent springs are close enough to each other so that $\theta \approx 0$ and $\cos(\theta) \approx 1$. The force exerted by the spring is then,

$$F_k^{\mathrm{cross-link}} = F_k + F_{\mathrm{cross-link}}|_{\mathrm{n+1}} + F_{\mathrm{cross-link}}|_{\mathrm{n-1}},$$

$$F_k^{\mathrm{cross-link}} = F_k - \mathrm{k}_{\text{cross-link}}\left[\mathrm{L}_{\mathrm{spr}}\big|_{\mathrm{n-1}} - \mathrm{L}_{\mathrm{spr}}\big|_{\mathrm{n+1}}\right].$$

where F_k is calculated using Eqn.C1.

Table 2.6 List of model parameters

Spindle length

Variable Name	Label	Default Values	Parameter Source	*In vivo* values	Parameter Relationships	Citations
Spindle Length	L_{ip}	1.5 $\times 10^{-6}$ m	Measured; Minimum 0.8 $\times 10^{-6}$ m due to overlap	WT: 1.5 $\times 10^{-6}$ m	L_{ip} is the integral of V_{ip} L_{ip}-L_{kMT}=L_{spring}	(Winey et al., 1995; Stephens et al., 2011)
Spindle Velocity	V_{ip}	-	Measured; observed range -3.5 to 3.5 10^{-6} m/min	Shortening .54 – 2.34 $\times 10^{-6}$ m/min, Growth .42 – 1.6 10^{-6} m/min, No spring: 3.5 10^{-6} m/min	V_{ip} = 3 10^{-6} m/min × [1 + ((F_k + F_{drag})/ F_{ip})]	Motor speed: (Hunt et al., 1994; Svoboda and Block, 1994) *in vivo* (Harrison et al., 2009); this paper
Outward Motor Force	F_{ip}	2 to 3 $\times 10^{-10}$N	-	-	F_{ip} = D × (6 × 10^{-12} N	
Inward Spring Force	F_k	-2 to -3 $\times 10^{-10}$N	-	-	$\Sigma F_k 1 \rightarrow F_k 16 = F_k$	
Drag Force	F_{drag}	-5 to 5 $\times 10^{-12}$N	-	-	V_{ip}*C_{drag}=F_{drag}	
Drag Coefficient	C_{drag}	3×10^{-5} Nsec/m	Measured; Model insensitive	175 poise*L_{ip}	V_{ip}*C_{drag}=F_{drag} F_{ip}+F_k+F_{drag}=F_{net}	(Fisher et al., 2009)

ipMTs and Motors

Variable Name	Label	Default Values	Parameter Source	In vivo values	Parameter Relationships	Citations
Overlap Zone	L_{lap}	0.8 $\times 10^{-6}$N m	Measured; Constant	-	L_{lap} is involved in singleToDouble and freeToSingle	(Winey et al., 1995; Schuyler et al., 2003)
Free Motors	*Free/U*	400	Total measured (Bound and free); initial distribution insensitive	-	Involved in singleToDouble and singleToFree	(Lawrimore, Stephens and Bloom, unpublished)
Single bound interpolar motors	*Single ipMT*	35 (×4 ipMT pairs, 140 total)	Initial distribution insensitive	-	Involved in singleToFree and freeToSingleipMt	
Single bound kinetochore motors	*Single kMT*	150	Initial distribution insensitive	-	Involved in singleToFree and freeToSinglekMT	
Double Bound Motors	*D*	10 (×4 ipMT pairs, 40 total)	Initial distribution insensitive	-	*Fip = D*Nmotors* *D* depends on functions doubleToSingle, freeToSingle, singleToDouble, and singleToFree	
Motor Force	F_m	6 × 10^{-12}N	Measured *in vitro* stall force	-	$F_{ip} = D \times F_m$	(Hunt et al., 1994; Svoboda and Block, 1994)

kMTs and Springs

Variable Name	Label	Default Values	Parameter Source	*In vivo* values	Parameter Relationships	Citations
Kinetochore Microtubule Length	L_{kMT}	350 $\times 10^{-9}$ m	Measured; 50 $\times 10^{-9}$ m minimum from EM	350 $\times 10^{-9}$ m, avg kMT	L_{kMT} switches stochastically between growth and shrinkage. Switching depends on F_k and L_{kMT}, respectivley	(Winey et al., 1995; Gardner et al., 2005)
Growth Rate	R_{gro}	17×10^{-9} m/s	Measured (probability to switch states fitted)	17 $\times 10^{-9}$ m/s	The length added to each kMT is the integral of R_{gro}	(Gardner et al., 2005)
Shrinking Rate	R_{shr}	25×10^{-9} m/s	Measured (probability to switch states fitted)	25 $\times 10^{-9}$ m/s	The length subtracted from each kMT is the integral of R_{shr}	(Gardner et al., 2005)
Spring Length	L_{spring}	800 $\times 10^{-9}$ m	Measured aggregate inter-kinetochore distance	800 $\times 10^{-9}$ m	$L_{spring} = L_{ip} - (L^{left}_{kMT} + L^{right}_{kMT})$	(Bouck and Bloom, 2007; Stephens et al., 2011)
Spring Force	F_k^{ind}	-	-	-	If $L_{spring} < L_{threshold}$, $F_k^{ind} = k_1(L_{spring} - L_{rest1})$ If $L_{spring} \geq L_{threshold}$ $F_k^{ind} = k_2(L_{spring} - L_{rest2})$	
Looped Spring Constant	k_1	30×10^{-6} N/m	Free; Explored 5 - 150 $\times 10^{-6}$ N/m	-	If $L_{spring} < L_{threshold}$ $F_k^{ind} = k_1(L_{spring} - L_{rest1})$	
Unlooped Spring Constant	k_2	-	-	-	$k_2 = k_1 * [L_1 / (L_1 + L_{openloop})]$ If $L_{spring} \geq L_{threshold}$ $F_k^{ind} = k_2(L_{spring} - L_{rest2})$	
Looped Rest Length	L_{rest1}	200 $\times 10^{-9}$ m	Estimated from measured	< than 250 $\times 10^{-9}$ m	If $L_{spring} < L_{threshold}$ $F_k^{ind} = k_1(L_{spring} - L_{rest1})$	(Bystricky et al., 2004)

Unlooped Rest Length	L_{rest2}	650 $\times 10^{-9}$ m	-	> than 250 $\times 10^{-9}$ m	$L_{rest2} = L_{rest1} + L_{openloop}$	
Threshold	$L_{threshold}$	975 $\times 10^{-9}$ m (best-fit WT)	Free; explored 1.1 -0.8 $\times 10^{-6}$ m	-	Deterministic length at which spring switches from k_1 to k_2 and L_{rest1} to L_{rest2}	
Loop Length	$L_{openloop}$	450 $\times 10^{-9}$ m	Estimated from measured‡	10 kb LacO = 450 $\times 10^{-9}$ m of 11nm fiber	Used to calculate k_2 and L_{rest2}	(Stephens et al., 2011)
Loop Stretching		-	True or False	10% of the time in WT	If stretched true, the spring is not looped If stretched is false, the spring is looped	
Cross-linking Spring Constant	$k_{cross\text{-}link}$	9 $\times 10^{-6}$ N/m (best-fit WT)	Free; explored 0 -15 $\times 10^{-6}$ N/m	-	$F_k^{cross\text{-}link} = F_k - k_{cross\text{-}link}(L_{spring}^{n-1} - L_{spring}^{n+1})$	This paper

‡Wild-type mean axial distance between a 1.7 kb LacO and a 6.8 kb LacO focus translates into a 102 bp/nm compaction. The mean axial distance between a wild-type 1.7 kb LacO to a stretched 6.8 kb LacO has an increase in distance (50nm to 189 nm), which translates into a 27 bp/nm compaction and is consistent with extended nucleosomal compacted chromatin (11 nm fiber).

Additional spindle forces

Astral microtubules: In metaphase there are approximately 2-3 astral microtubules extending from the spindle pole into the cytoplasm, versus the ~40 spindle microtubules. The astral microtubules are critical for spindle orientation and are acted upon by cytoplasmic dynein (Pearson and Bloom, 2004). Deletion of dynein has little to no effect on the kinetics of spindle elongation or the duration of metaphase (Yeh et al., 1995). Rather, loss of dynein results in mis-oriented spindles whose position is monitored by the spindle position checkpoint.

Nuclear membrane forces: The nuclear membrane has a heterogeneous morphology. Membrane protrusions have been observed to even precede the spindle upon migration into the daughter cell during anaphase (Yeh et al., 1995; Walters et al., 2012). Since spindle elongation is highly stereotypic and independent of changes in nuclear shape we do not consider the impact of nuclear envelop force on the spindle.

*Inward motor forces***:** An important component of the spindle machine is the minus-end motor Kar3. *KAR3* is a non-essential gene that nonetheless contributes to the fidelity of chromosome segregation in mitosis. Kar3 is found in metaphase along the ipMTs as well as kMTs and microtubule plus-ends. Deletion of kar3 suppresses the loss of outward motors, Cin8 and Kip1 giving rise to the model that Kar3 provides an important inward force in metaphase (Saunders and Hoyt, 1992; Saunders et al., 1997). While it is important to model the role of Kar3 in mitosis, the simplest model is that Kar3 opposes the outward motors Cin8 and Kip1. Incorporation of an additional parameter that opposes Cin8 and Kip1 will not substantively change the model.

Kinetochore forces: Kinetochore forces are implicit as the mechanism that translates the spatial catastrophe gradient and tension dependent rescue from the chromatin spring to kinetochore microtubule plus-ends. The question of how much force the kinetochore generates has been addressed through elegant in vitro experiments with isolated kinetochores (Akiyoshi et al., 2010). The rupture force to dissociate the kinetochore from a microtubule is approximately 9pN (Akiyoshi et al., 2010). This is equivalent to the force of a single motor protein (~6pN). The implicit assumption in the values used in the model is that motors reach their stall force *in vivo*, and consequently the spring constant is on the order of motor stalling. An unanswered question in the field is whether motors ever reach their stall force *in vivo* and how close to the rupture force the system is working. Implementing the microtubule-based force at the kinetochore will change the value of the spring constant, but does not substantively change the model.

Variation in chromatin springs is not incorporated in the model including: histone exchange in the pericentric chromatin (Verdaasdonk et al., 2012), the likelihood that spring constants for different chromosomes are not identical nor are the switching thresholds, and variation in chromatin protein number (e.g. cohesin, condensin). These listed sources account for *in vivo* noise but should not alter the overall trends or behavior of the model.

References

Akiyoshi, B., K.K. Sarangapani, A.F. Powers, C.R. Nelson, S.L. Reichow, H. Arellano-Santoyo, T. Gonen, J.A. Ranish, C.L. Asbury, and S. Biggins. 2010. Tension directly stabilizes reconstituted kinetochore-microtubule attachments. *Nature*. 468:576-9.

Alushin, G., and E. Nogales. 2011. Visualizing kinetochore architecture. *Curr Opin Struct Biol*. 21:661-9.

Bachant, J., A. Alcasabas, Y. Blat, N. Kleckner, and S.J. Elledge. 2002. The SUMO-1 isopeptidase Smt4 is linked to centromeric cohesion through SUMO-1 modification of DNA topoisomerase II. *Mol Cell*. 9:1169-82.

Batchelor, G.K. 1967. An Introduction to Fluid Dynamics. Cambridge University Press.

Birtwistle, M.R., J. Rauch, A. Kiyatkin, E. Aksamitiene, M. Dobrzynski, J.B. Hoek, W. Kolch, B.A. Ogunnaike, and B.N. Kholodenko. 2012. Emergence of bimodal cell population responses from the interplay between analog single-cell signaling and protein expression noise. *BMC Syst Biol*. 6:109.

Blat, Y., and N. Kleckner. 1999. Cohesins bind to preferential sites along yeast chromosome III, with differential regulation along arms versus the centric region. *Cell*. 98:249-59.

Bloom, K., and E. Yeh. 2010. Tension management in the kinetochore. *Curr Biol*. 20:R1040-8.

Bouck, D.C., and K. Bloom. 2007. Pericentric chromatin is an elastic component of the mitotic spindle. *Curr Biol*. 17:741-8.

Bystricky, K., P. Heun, L. Gehlen, J. Langowski, and S.M. Gasser. 2004. Long-range compaction and flexibility of interphase chromatin in budding yeast analyzed by high-resolution imaging techniques. *Proc Natl Acad Sci U S A*. 101:16495-500.

Carminati, J.L., and T. Stearns. 1997. Microtubules orient the mitotic spindle in yeast through dynein-dependent interactions with the cell cortex. *J Cell Biol*. 138:629-41.

Civelekoglu-Scholey, G., D.J. Sharp, A. Mogilner, and J.M. Scholey. 2006. Model of chromosome motility in Drosophila embryos: adaptation of a general mechanism for rapid mitosis. *Biophys J*. 90:3966-82.

Cuylen, S., J. Metz, and C.H. Haering. 2011. Condensin structures chromosomal DNA through topological links. *Nat Struct Mol Biol*. 18:894-901.

Cytrynbaum, E.N., P. Sommi, I. Brust-Mascher, J.M. Scholey, and A. Mogilner. 2005. Early spindle assembly in Drosophila embryos: role of a force balance involving cytoskeletal dynamics and nuclear mechanics. *Mol Biol Cell*. 16:4967-81.

Fisher, J.K., M. Ballenger, E.T. O'Brien, J. Haase, R. Superfine, and K. Bloom. 2009. DNA relaxation dynamics as a probe for the intracellular environment. *Proc Natl Acad Sci U S A*. 106:9250-5.

Gardner, M.K., D.J. Odde, and K. Bloom. 2007. Hypothesis testing via integrated computer modeling and digital fluorescence microscopy. *Methods*. 41:232-7.

Gardner, M.K., C.G. Pearson, B.L. Sprague, T.R. Zarzar, K. Bloom, E.D. Salmon, and D.J. Odde. 2005. Tension-dependent regulation of microtubule dynamics at kinetochores can explain metaphase congression in yeast. *Mol Biol Cell*. 16:3764-75.

Gardner, M.K., B.L. Sprague, C.G. Pearson, B.D. Cosgrove, A.D. Bicek, K. Bloom, E.D. Salmon, and D.J. Odde. 2010. Model Convolution: A Computational Approach to Digital Image Interpretation. *Cell Mol Bioeng*. 3:163-170.

Gay, G., T. Courtheoux, C. Reyes, S. Tournier, and Y. Gachet. 2012. A stochastic model of kinetochore-microtubule attachment accurately describes fission yeast chromosome segregation. *J Cell Biol*. 196:757-74.

Glynn, E.F., P.C. Megee, H.G. Yu, C. Mistrot, E. Unal, D.E. Koshland, J.L. DeRisi, and J.L. Gerton. 2004. Genome-wide mapping of the cohesin complex in the yeast Saccharomyces cerevisiae. *PLoS Biol*. 2:E259.

Goshima, G., and M. Yanagida. 2000. Establishing biorientation occurs with precocious separation of the sister kinetochores, but not the arms, in the early spindle of budding yeast. *Cell*. 100:619-33.

Granick, S., and M. Rubinstein. 2004. Polymers: a multitude of macromolecules. *Nat Mater*. 3:586-7.

Greulich, K.O., E. Wachtel, J. Ausio, D. Seger, and H. Eisenberg. 1987. Transition of chromatin from the "10 nm" lower order structure, to the "30 nm" higher order structure as followed by small angle X-ray scattering. *J Mol Biol*. 193:709-21.

Haase, J., A. Stephens, J. Verdaasdonk, E. Yeh, and K. Bloom. 2012. Bub1 kinase and Sgo1 modulate pericentric chromatin in response to altered microtubule dynamics. *Curr Biol*. 22:471-81.

Hagstrom, K.A., V.F. Holmes, N.R. Cozzarelli, and B.J. Meyer. 2002. C. elegans condensin promotes mitotic chromosome architecture, centromere organization, and sister chromatid segregation during mitosis and meiosis. *Genes Dev*. 16:729-42.

Harrison, B.D., M.L. Hoang, and K. Bloom. 2009. Persistent Mechanical Linkage Between Sister Chromatids Throughout Anaphase *Chromosoma*. 118:633-645.

He, X., S. Asthana, and P.K. Sorger. 2000. Transient sister chromatid separation and elastic deformation of chromosomes during mitosis in budding yeast. *Cell*. 101:763-75.

Hirano, T. 2006. At the heart of the chromosome: SMC proteins in action. *Nat Rev Mol Cell Biol*. 7:311-22.

Hu, B., T. Itoh, A. Mishra, Y. Katoh, K.L. Chan, W. Upcher, C. Godlee, M.B. Roig, K. Shirahige, and K. Nasmyth. 2011. ATP hydrolysis is required for relocating cohesin from sites occupied by its Scc2/4 loading complex. *Curr Biol*. 21:12-24.

Hunt, A.J., F. Gittes, and J. Howard. 1994. The force exerted by a single kinesin molecule against a viscous load. *Biophys J*. 67:766-81.

Janson, M.E., R. Loughlin, I. Loiodice, C. Fu, D. Brunner, F.J. Nedelec, and P.T. Tran. 2007. Crosslinkers and motors organize dynamic microtubules to form stable bipolar arrays in fission yeast. *Cell*. 128:357-68.

Kawamura, R., L.H. Pope, M.O. Christensen, M. Sun, K. Terekhova, F. Boege, C. Mielke, A.H. Andersen, and J.F. Marko. 2010. Mitotic chromosomes are constrained by topoisomerase II-sensitive DNA entanglements. *J Cell Biol*. 188:653-63.

Kim, K.H., and H.M. Sauro. 2012. In search of noise-induced bimodality. *BMC Biol*. 10:89.

Lam, W.W., E.A. Peterson, M. Yeung, and B.D. Lavoie. 2006. Condensin is required for chromosome arm cohesion during mitosis. *Genes Dev*. 20:2973-84.

Lengronne, A., Y. Katou, S. Mori, S. Yokobayashi, G.P. Kelly, T. Itoh, Y. Watanabe, K. Shirahige, and F. Uhlmann. 2004. Cohesin relocation from sites of chromosomal loading to places of convergent transcription. *Nature*. 430:573-8.

Liu, D., G. Vader, M.J. Vromans, M.A. Lampson, and S.M. Lens. 2009. Sensing chromosome bi-orientation by spatial separation of aurora B kinase from kinetochore substrates. *Science*. 323:1350-3.

Manning, A.L., M.S. Longworth, and N.J. Dyson. 2010. Loss of pRB causes centromere dysfunction and chromosomal instability. *Genes Dev*. 24:1364-76.

McIntosh, J.R., M.I. Molodtsov, and F.I. Ataullakhanov. 2012. Biophysics of mitosis. *Q Rev Biophys*. 45:147-207.

Megee, P.C., C. Mistrot, V. Guacci, and D. Koshland. 1999. The centromeric sister chromatid cohesion site directs Mcd1p binding to adjacent sequences. *Mol Cell*. 4:445-50.

Mishra, A., B. Hu, A. Kurze, F. Beckouet, A.M. Farcas, S.E. Dixon, Y. Katou, S. Khalid, K. Shirahige, and K. Nasmyth. 2010. Both interaction surfaces within cohesin's hinge domain are essential for its stable chromosomal association. *Curr Biol*. 20:279-89.

Mogilner, A., and E. Craig. 2010. Towards a quantitative understanding of mitotic spindle assembly and mechanics. *J Cell Sci*. 123:3435-45.

Munsky, B., G. Neuert, and A. van Oudenaarden. 2012. Using gene expression noise to understand gene regulation. *Science*. 336:183-7.

Nativio, R., K.S. Wendt, Y. Ito, J.E. Huddleston, S. Uribe-Lewis, K. Woodfine, C. Krueger, W. Reik, J.M. Peters, and A. Murrell. 2009. Cohesin is required for higher-order chromatin conformation at the imprinted IGF2-H19 locus. *PLoS Genet*. 5:e1000739.

Ng, T.M., W.G. Waples, B.D. Lavoie, and S. Biggins. 2009. Pericentromeric sister chromatid cohesion promotes kinetochore biorientation. *Mol Biol Cell*. 20:3818-27.

O'Toole, E.T., M. Winey, and J.R. McIntosh. 1999. High-voltage electron tomography of spindle pole bodies and early mitotic spindles in the yeast Saccharomyces cerevisiae. *Mol Biol Cell*. 10:2017-31.

Okumura, Y., and K. Ito. 2001. The Polyrotaxane Gel: A topological gel by figure-of-eight Cross-links. *Advanced Materials*. 13:485-487.

Panyukov, S.V., S.S. Sheiko, and M. Rubinstein. 2009. Amplification of tension in branched macromolecules. *Phys Rev Lett*. 102:148301.

Pearson, C.G., and K. Bloom. 2004. Dynamic microtubules lead the way for spindle positioning. *Nat Rev Mol Cell Biol*. 5:481-92.

Pearson, C.G., P.S. Maddox, E.D. Salmon, and K. Bloom. 2001. Budding yeast chromosome structure and dynamics during mitosis. *J Cell Biol*. 152:1255-66.

Peterson, J.B., and H. Ris. 1976. Electron-microscopic study of the spindle and chromosome movement in the yeast Saccharomyces cerevisiae. *J Cell Sci*. 22:219-42.

Quammen, C.W., A.C. Richardson, J. Haase, B.D. Harrison, R.M. Taylor, and K.S. Bloom. 2008. FluoroSim: A Visual Problem-Solving Environment for Fluorescence Microscopy. *Eurographics Workshop Vis Comput Biomed*. 2008:151-158.

Ribeiro, S.A., J.C. Gatlin, Y. Dong, A. Joglekar, L. Cameron, D.F. Hudson, C.J. Farr, B.F. McEwen, E.D. Salmon, W.C. Earnshaw, and P. Vagnarelli. 2009. Condensin regulates the stiffness of vertebrate centromeres. *Mol Biol Cell*. 20:2371-80.

Rohner, S., S.M. Gasser, and P. Meister. 2008. Modules for cloning-free chromatin tagging in Saccharomyces cerevisae. *Yeast*. 25:235-9.

Samoshkin, A., A. Arnaoutov, L.E. Jansen, I. Ouspenski, L. Dye, T. Karpova, J. McNally, M. Dasso, D.W. Cleveland, and A. Strunnikov. 2009. Human condensin function is essential for centromeric chromatin assembly and proper sister kinetochore orientation. *PLoS One*. 4:e6831.

Saunders, W., V. Lengyel, and M.A. Hoyt. 1997. Mitotic spindle function in Saccharomyces cerevisiae requires a balance between different types of kinesin-related motors. *Mol Biol Cell*. 8:1025-33.

Saunders, W.S., and M.A. Hoyt. 1992. Kinesin-related proteins required for structural integrity of the mitotic spindle. *Cell*. 70:451-8.

Schuyler, S.C., J.Y. Liu, and D. Pellman. 2003. The molecular function of Ase1p: evidence for a MAP-dependent midzone-specific spindle matrix. Microtubule-associated proteins. *J Cell Biol*. 160:517-28.

Sprague, B.L., C.G. Pearson, P.S. Maddox, K.S. Bloom, E.D. Salmon, and D.J. Odde. 2003. Mechanisms of microtubule-based kinetochore positioning in the yeast metaphase spindle. *Biophys J*. 84:3529-46.

Stephens, A.D., J. Haase, L. Vicci, R.M. Taylor, 2nd, and K. Bloom. 2011. Cohesin, condensin, and the intramolecular centromere loop together generate the mitotic chromatin spring. *J Cell Biol*. 193:1167-80.

Sun, M., R. Kawamura, and J.F. Marko. 2011. Micromechanics of human mitotic chromosomes. *Phys Biol*. 8:015003.

Svoboda, K., and S.M. Block. 1994. Force and velocity measured for single kinesin molecules. *Cell*. 77:773-84.

Tanaka, T., M.P. Cosma, K. Wirth, and K. Nasmyth. 1999. Identification of cohesin association sites at centromeres and along chromosome arms. *Cell*. 98:847-58.

Tanaka, T., J. Fuchs, J. Loidl, and K. Nasmyth. 2000. Cohesin ensures bipolar attachment of microtubules to sister centromeres and resists their precocious separation. *Nat Cell Biol*. 2:492-9.

Uchida, K.S., K. Takagaki, K. Kumada, Y. Hirayama, T. Noda, and T. Hirota. 2009. Kinetochore stretching inactivates the spindle assembly checkpoint. *J Cell Biol*. 184:383-90.

Umbreit, N.T., and T.N. Davis. 2012. Mitosis puts sisters in a strained relationship: force generation at the kinetochore. *Exp Cell Res*. 318:1361-6.

Vas, A.C., C.A. Andrews, K. Kirkland Matesky, and D.J. Clarke. 2007. In vivo analysis of chromosome condensation in Saccharomyces cerevisiae. *Mol Biol Cell*. 18:557-68.

Verdaasdonk, J.S., R. Gardner, A.D. Stephens, E. Yeh, and K. Bloom. 2012. Tension-dependent nucleosome remodeling at the pericentromere in yeast. *Mol Biol Cell*. 23:2560-70.

Visscher, K., M.J. Schnitzer, and S.M. Block. 1999. Single kinesin molecules studied with a molecular force clamp. *Nature*. 400:184-9.

Walters, A.D., A. Bommakanti, and O. Cohen-Fix. 2012. Shaping the nucleus: factors and forces. *J Cell Biochem*. 113:2813-21.

Wang, B.D., D. Eyre, M. Basrai, M. Lichten, and A. Strunnikov. 2005. Condensin binding at distinct and specific chromosomal sites in the Saccharomyces cerevisiae genome. *Mol Cell Biol*. 25:7216-25.

Warsi, T.H., M.S. Navarro, and J. Bachant. 2008. DNA topoisomerase II is a determinant of the tensile properties of yeast centromeric chromatin and the tension checkpoint. *Mol Biol Cell*. 19:4421-33.

Watanabe, Y. 2012. Geometry and force behind kinetochore orientation: lessons from meiosis. *Nat Rev Mol Cell Biol*. 13:370-82.

Welburn, J.P., M. Vleugel, D. Liu, J.R. Yates, 3rd, M.A. Lampson, T. Fukagawa, and I.M. Cheeseman. 2010. Aurora B phosphorylates spatially distinct targets to differentially regulate the kinetochore-microtubule interface. *Mol Cell*. 38:383-92.

Winey, M., and K. Bloom. 2012. Mitotic spindle form and function. *Genetics*. 190:1197-224.

Winey, M., C.L. Mamay, E.T. O'Toole, D.N. Mastronarde, T.H. Giddings, Jr., K.L. McDonald, and J.R. McIntosh. 1995. Three-dimensional ultrastructural analysis of the Saccharomyces cerevisiae mitotic spindle. *J Cell Biol*. 129:1601-15.

Wollman, R., E.N. Cytrynbaum, J.T. Jones, T. Meyer, J.M. Scholey, and A. Mogilner. 2005. Efficient chromosome capture requires a bias in the 'search-and-capture' process during mitotic-spindle assembly. *Curr Biol*. 15:828-32.

Yeh, E., J. Haase, L.V. Paliulis, A. Joglekar, L. Bond, D. Bouck, E.D. Salmon, and K.S. Bloom. 2008. Pericentric chromatin is organized into an intramolecular loop in mitosis. *Curr Biol*. 18:81-90.

Yeh, E., R.V. Skibbens, J.W. Cheng, E.D. Salmon, and K. Bloom. 1995. Spindle dynamics and cell cycle regulation of dynein in the budding yeast, Saccharomyces cerevisiae. *J Cell Biol*. 130:687-700.

Yong-Gonzalez, V., B.D. Wang, P. Butylin, I. Ouspenski, and A. Strunnikov. 2007. Condensin function at centromere chromatin facilitates proper kinetochore tension

and ensures correct mitotic segregation of sister chromatids. *Genes Cells*. 12:1075-90..

CHAPTER 3

INDIVIDUAL PERICENTROMERES BEHAVE AS AN ENSEMBLE IN THE YEAST SPINDLE

This chapter is adapted from a manuscript submitted to The Journal of Cell Biology. Chloe E. Snider, Julian Haase, Rachel A. Haggerty, Paula A. Vasquez, M. Gregory Forest, and Kerry Bloom aided in experiments, analysis of data, and writing.

Summary

The mitotic spindle apparatus, composed of microtubules and chromatin, functions to faithfully segregate a duplicated genome into two daughter cells. Microtubules exert an extensional pulling force on sister chromatids towards opposite poles while pericentric chromatin resists with contractile spring-like properties. Tension generated from these opposing forces silences the spindle checkpoint to ensure accurate chromosome segregation. It is unknown how the cell senses tension across multiple microtubule attachment sites considering the stochastic dynamics of microtubule growth and shortening. In budding yeast, there is one microtubule attachment site per chromosome. By labeling several chromosomes we find that pericentromeres display coordinated motion and stretching in metaphase. The pericentromeres of different chromosomes exhibit physical linkage dependent on centromere function. Coordinated motion is dependent on condensin and the kinesin motor Cin8 while

coordinated stretching is dependent on pericentric cohesin and Cin8. Linking of pericentric chromatin, through cohesin and condensin, and kinetochore microtubules, through Cin8, functions to equalize tension over a dynamic multiple attachment site.

Introduction

In mitosis sister chromatids are bioriented on the spindle. Spindle microtubules bind to the chromosome's centromere via the kinetochore. Microtubule dynamics are balanced by chromatin with a spring-like force. The tension generated stabilizes kMT attachments and signals the proper alignment of chromosomes to the spindle checkpoint (Bloom and Yeh, 2010; Maresca and Salmon, 2010). In yeast there are 16 chromosomes each with a single microtubule attachment site (Peterson and Ris, 1976; O'Toole et al., 1999). The pericentric chromatin (50 kb surrounding the centromere) along with cohesin and condensin generate the chromatin spring (Stephens et al., 2011). However, we do not know if the chromatin spring exists as 16 separate springs or as one interlinked spring in metaphase. This is important for understanding how different kinetochore attachments adapt to different tension and signaling states.

The stereotypical structure of the spindle apparatus of *S. cerevisiae* allows us to investigate the behavior of chromatin proximal to a single kinetochore microtubule attachment site. The kinetochores from 16 chromosomes each with a single centromere attachment site form two sister clusters (Goshima and Yanagida, 2000; Pearson and Bloom, 2004). In yeast, the centromere is defined by 125 bp sequence (Fitzgerald-Hayes et al., 1982) allowing for precise insertion of LacO relative the kinetochore attachment. In metaphase

sister pericentric LacO arrays appear as two foci bioriented on the spindle axis (Tanaka et al., 2000; He et al., 2000; Goshima and Yanagida, 2000; Pearson et al., 2001). The arrays are dynamic and can transiently reassociate into one spot. Pericentromere LacO arrays stretch (~10%) and decompact along the spindle axis (He et al., 2000; Bachant et al., 2002; Warsi et al., 2008; Stephens et al., 2011).

The pericentric chromatin is enriched three fold in cohesin and condensin (Megee et al., 1999; Tanaka et al., 1999; Wang et al., 2005; D'Ambrosio et al., 2008). These SMC (Structural Maintenance of Chromosomes) protein complexes are necessary for the function of the chromatin spring and faithful segregation of the genome in yeast (Yong-Gonzalez et al., 2007; Ng et al., 2009; Stephens et al., 2011) as well as mammals (Samoshkin et al., 2009; Uchida et al., 2009; Ribeiro et al., 2009; Manning et al., 2010). Interestingly, these two complexes have differing roles in the pericentromere. Cohesin localizes distal to the spindle axis where it radially confines pericentric chromatin while condensin is localized along the spindle axis where it axially compacts the pericentromere (Stephens et al., 2011). It is unknown how cohesin and condensin promote elasticity of the chromatin spring. Condensin is known to compact distal regions along a single chromatid (Kimura and Hirano, 1997; Hirano et al., 1997; Sutani et al., 1999; Freeman et al., 2000), while cohesin can tether sister chromatids (Guacci et al., 1997; Michaelis et al., 1997) as well as distal regions (Nativio et al., 2009). These functions may provide the mechanistic basis for a spring network in mitosis.

In order to investigate how pericentromeres of different chromosomes behave relative to each other we have built strains with multiply labeled pericentromeres. We describe correlated chromatin motion and coordinated stretching of pericentromeres of different

chromosomes. These results suggest that a chromatin network exists to coordinate dynamics across multiple microtubule attachment sites in the mitotic spindle.

Results

Pericentromeres of different chromosomes display correlated movement in metaphase

To determine if pericentromeres of different chromosomes behave in a coordinated fashion during metaphase, we imaged LacO and TetO arrays linked to CEN 15 and CEN 11 respectively. Movement of each pericentromere was measured relative to its respective spindle pole body (red, Figure 3.1 A). The movements of pericentromeres in the same half spindle were compared using cross-correlation analysis. Pericentromere foci movements were correlated in mitosis (R = 0.33 ± .34, n = 88), and significantly lower in G1 (R= 0.15 ± .33, n = 80, P < 0.001, Figure 3.1 D). Similar results were found with a different set of labeled chromosomes (CEN 3 CEN 11, Figure 3.2 A).

TetO and LacO arrays in a single pericentromere provide a measure of maximum correlation. Motion analysis of TetO and LacO arrays in cis (CEN 11 centroids at 4.5 kb and 9.4 kb respectively) resulted in a cross-correlation of 0.30 ± .36 (n = 24, Figure 3.1, B and D). A similar value of cross-correlation is observed for cis labels in G1 (0.40 ± .23, n = 71, P > 0.2, Figure 3.1 D). Sister centromere movements, analyzed relative to the mid spindle, were also found to have a comparable degree of cross-correlation (0.34 ± .33, n = 88, all metaphase P > 0.5, Figure 3.1, C and D). The uniformity of motion irrespective of the physical relationship of the markers (cis or trans) is indicative of a network rather than independently regulated springs.

To explore the physical state of the chromatin we examined the spatial position of cis TetO and LacO arrays *in vivo*. If the chromatin is stiff, the more likely the spatial position of these arrays will match their physical position in the pericentromere. In contrast if the chromatin spring is floppy the spatial position of the arrays will be poorly correlated with their physical position. To estimate chromatin stiffness we imaged cis labels relative to their respective spindle pole. There is an equal chance for each cis label to be closer to the pole (Figure 3.1 E cis). This spatial relationship is similar for labels on different chromosomes as well (Figure 3.1 E trans). The lack of correspondence in spatial vs. physical position reflects the floppiness of the chromatin in vivo (Figure 3.1 E graphic). Therefore the relatively low cross-correlation value (~0.3 Figure 3.1 D) across the network is expected.

Coordinated stretching of pericentromeres

LacO arrays in the pericentromere are observed as foci or decompacted linear filaments. These filaments reflect stretching of the pericentromere in response to force (He et al., 2000; Bachant et al., 2002; Warsi et al., 2008; Stephens et al., 2011). The frequency of any given pericentromere LacO array stretching is ~10% in wild-type cells. If each pericentromere behaves independently then when one chromosome stretches it should not affect the probability of the second labeled chromosome to stretch. If coordinate stretching is greater than the independent chance of the second chromosome stretching then different chromosomes are likely to be linked/dependent.

Using pericentromeres labeled in trans (CEN 11 and CEN 15) we investigated the occurrence of coordinated stretching (Figure 3.1, F-I). Each pericentromere LacO/TetO displayed similar stretching (CEN 11, 12%; CEN 15, 11%, n = 267, Figure 3.1 H). Coordinated stretching resulted in 40% ± 1% (n = 37, Figure 3.1 I) of cells showing

stretching, significantly more than predicted by single stretching (11% dotted line, $\chi^2 < 1\times10^{-8}$, Figure 3.1 I). Of the coordinated stretching events 2/3 displayed stretching on the same side of the spindle (Figure 3.2 F). These results are reproducible for CEN 11 and CEN 3 (Figure 3.2, B-E). Correlated motion and stretching dynamics between pericentromeres of different chromosomes is indicative of a linked mechanism.

Simulations of cross-linking pericentromeres of different chromosomes

We utilized a mathematical model of the yeast spindle to query the extent that chromatin cross-links increase correlated motion and stretching in the spindle. A simple force-balance model provides a mechanism to deduce the physical properties of the chromatin spring (Stephens et al., 2013). Addition of cross-linking springs between pericentromeres and their two adjacent neighbors (low cross-linking) increases the correlated movement of kMT plus ends in the model. Cross-linking between all chromosomes (i.e. a cross-linked network) further increases the cross-correlation of kMT plus ends (Figure 3.3, A and B). Likewise, cross-links lead to increased coordinated stretching comparable to levels measured in wild-type cells (Figure 3.3 C; Stephens et al., 2013). Thus chromatin-based cross-linking represents a physically realistic mechanism for correlated movement and stretching observed *in vivo*.

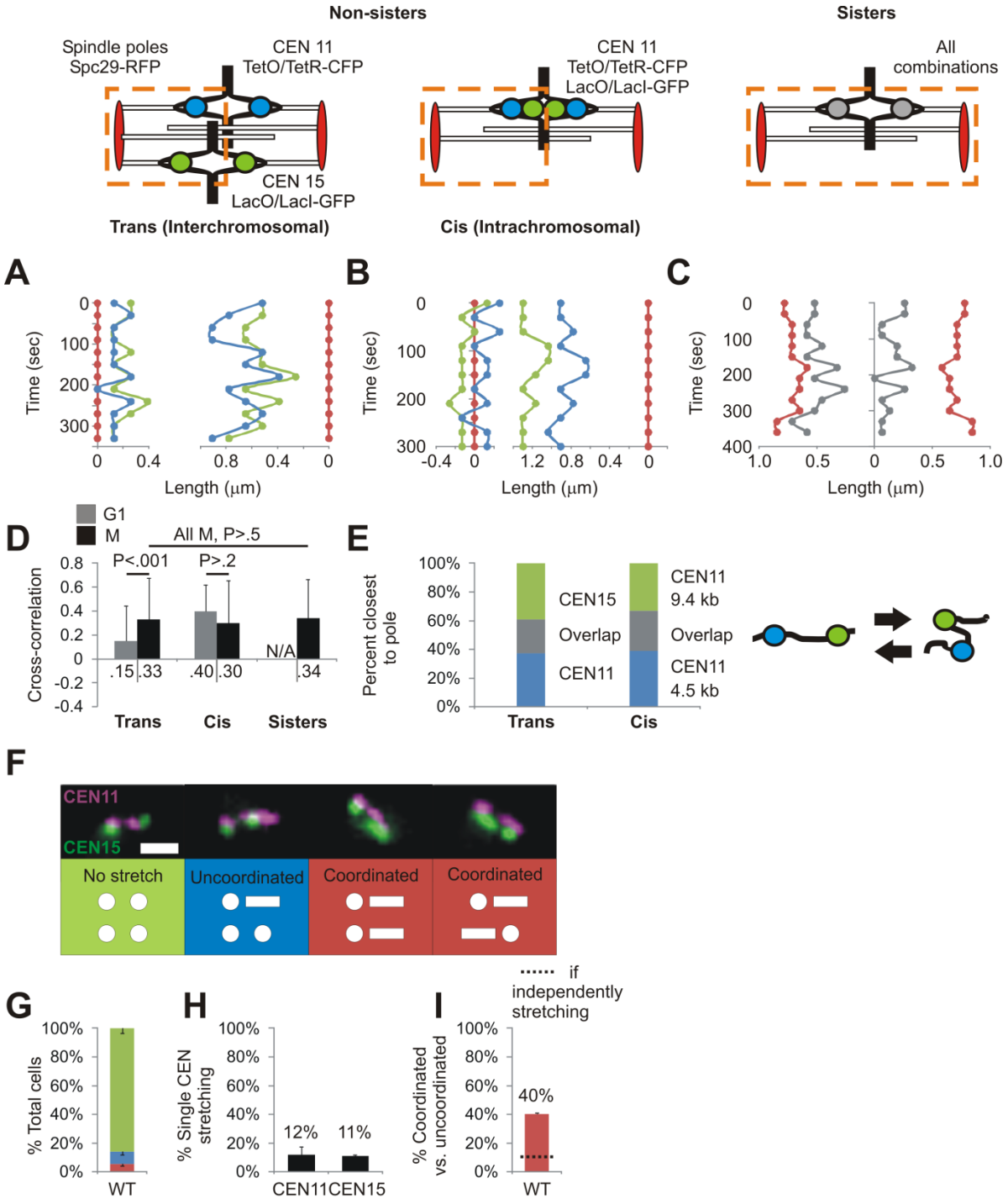
Non-sisters
Sisters
Spindle poles
Spc29-RFP
CEN 11
TetO/TetR-CFP
CEN 15
LacO/LacI-GFP
CEN 11
TetO/TetR-CFP
LacO/LacI-GFP
All
combinations
Trans (Interchromosomal)
Cis (Intrachromosomal)
A
B
C
Time (sec)
Length (μm)
D
G1
M
All M, P>.5
P<.001
P>.2
N/A
Cross-correlation
.15
.33
.40
.30
.34
Trans
Cis
Sisters
E
Percent closest to pole
CEN15
Overlap
CEN11
CEN11
9.4 kb
Overlap
CEN11
4.5 kb
Trans
Cis
F
CEN11
CEN15
No stretch
Uncoordinated
Coordinated
Coordinated
G
% Total cells
WT
H
% Single CEN stretching
12%
11%
CEN11
CEN15
I
if independently stretching
% Coordinated vs. uncoordinated
40%
WT

Figure 3.1 Pericentromeres of different chromosomes display correlated movement and coordinated stretching in metaphase

Compact (foci) pericentromere movements were tracked at 30 second intervals relative to their respective spindle pole body (Spc29-RFP) in (A) trans (TetO/TetR-CFP 8 kb array inserted at 0.5 kb from CEN 11 and LacO/LacI-GFP 10 kb array inserted 1.8 kb from CEN 15) and (B) cis labeled strains (TetO/TetR-CFP centroid at 4.5 kb and LacO/LacI-GFP centroid at 9.4 kb from CEN 11). (C) Sister arrays were tracked relative to the mid-spindle. (D) Cross-correlation analysis of trans, cis, and sister pericentromere movement in G1 and (M) Metaphase. Student t-test values are listed above. (E) Time courses were analyzed for which pericentromere label was closest to its respective pole at each time point (trans n = 742, cis n = 176). An equal probability to be closest to the pole suggests that pericentromere (cis) DNA can "flop" over itself (shown right). (F)Trans labeled pericentromeres were analyzed for compact (focus) or stretched arrays in metaphase. Scale bar = 1 μm. (G) Cells were categorized as No stretch (green, both arrays compact foci), Uncoordinated (blue, stretching in only one of the labeled CEN arrays) Coordinated (red, both CEN non-sister arrays display stretching). (H) Wild-type pericentromere stretching frequency is graphed for each CEN 11 and CEN 15. (I) If pericentromeres stretch independently, when one stretches the second chromosome should also stretch 11% of the time (dotted line, average single CEN stretching %). Coordinated stretching occurs in 40 ± 1% of cells that show stretching, higher than predicted by independent stretching frequencies. Independent experiments (Stephens et al., 2013) found similar coordinated stretching. Error bars represent standard deviation.

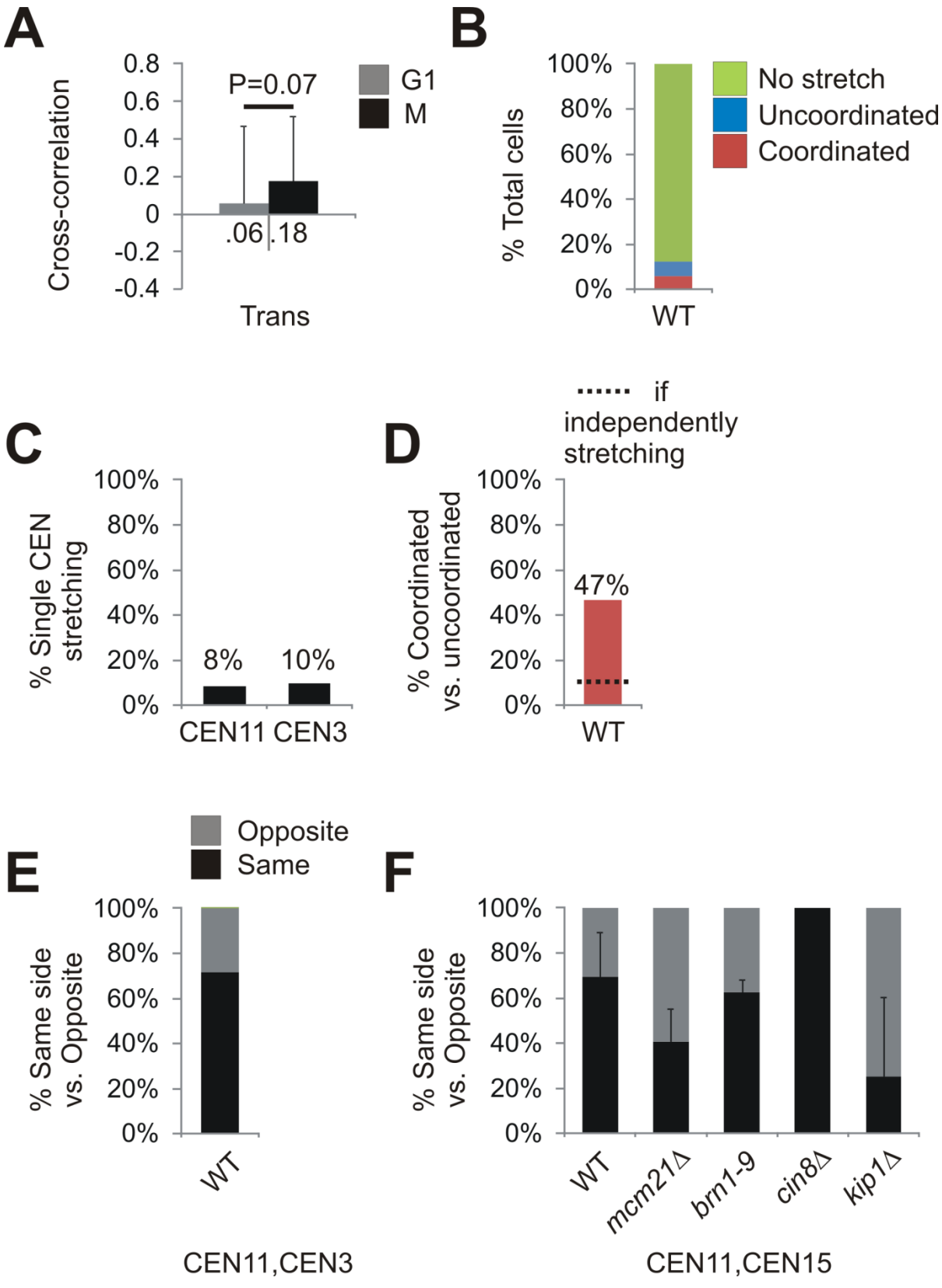
A
Cross-correlation
0.8
0.6
0.4
0.2
0
-0.2
-0.4
P=0.07
G1
M
.06
.18
Trans
B
% Total cells
100%
80%
60%
40%
20%
0%
No stretch
Uncoordinated
Coordinated
WT
C
% Single CEN stretching
100%
80%
60%
40%
20%
0%
8%
10%
CEN11 CEN3
D
if independently stretching
% Coordinated vs. uncoordinated
100%
80%
60%
40%
20%
0%
47%
WT
E
Opposite
Same
% Same side vs. Opposite
100%
80%
60%
40%
20%
0%
WT
CEN11,CEN3
F
% Same side vs. Opposite
100%
80%
60%
40%
20%
0%
WT
mcm21Δ
brn1-9
cin8Δ
kip1Δ
CEN11,CEN15

Figure 3.2 Trans labeled CEN 3 and CEN 11 recapitulate correlated movement and coordinated stretching

(A) Trans labeled strain was analyzed for correlated motion (TetO/TetR-CFP 8 kb array inserted at 0.5 kb from CEN 11 and LacO/LacI-GFP 10 kb array inserted 3.8 kb from CEN 3). Cross-correlation values for cells in G1 (n = 70) or Metaphase (M, n = 52). Student t-test values are listed above the graph for comparing G1 to M and for comparing all metaphase values (top). (B) Cells were categorized as No stretch (green, both arrays compact foci), Uncoordinated (blue, stretching in only one of the labeled CEN arrays) Coordinated (red, both CEN non-sister arrays display stretching; n = 121, 1 experiments). (C)Wild-type pericentromere stretching frequency is graphed for each CEN 11 and CEN 3. (D) If pericentromeres stretch independently, when one stretches the second chromosome should stretch 9% of the time (dotted line, average single CEN stretching %). Coordinated stretching occurs in 47% of cells, greater than predicted by independent stretching frequencies (n = 15 stretching events; also see CEN 11 and 15, Figure 3.1, G-I). (E, F) Percentage of coordinated stretching events displaying stretching in the same (black) or opposite (gray) half spindle for CEN 11 and CEN 3 WT (E) and CEN 11 and CEN 15 WT and mutants (F). In wild-type the majority of coordinated stretching events occur on the same side (67%). Error bars represent standard deviation.

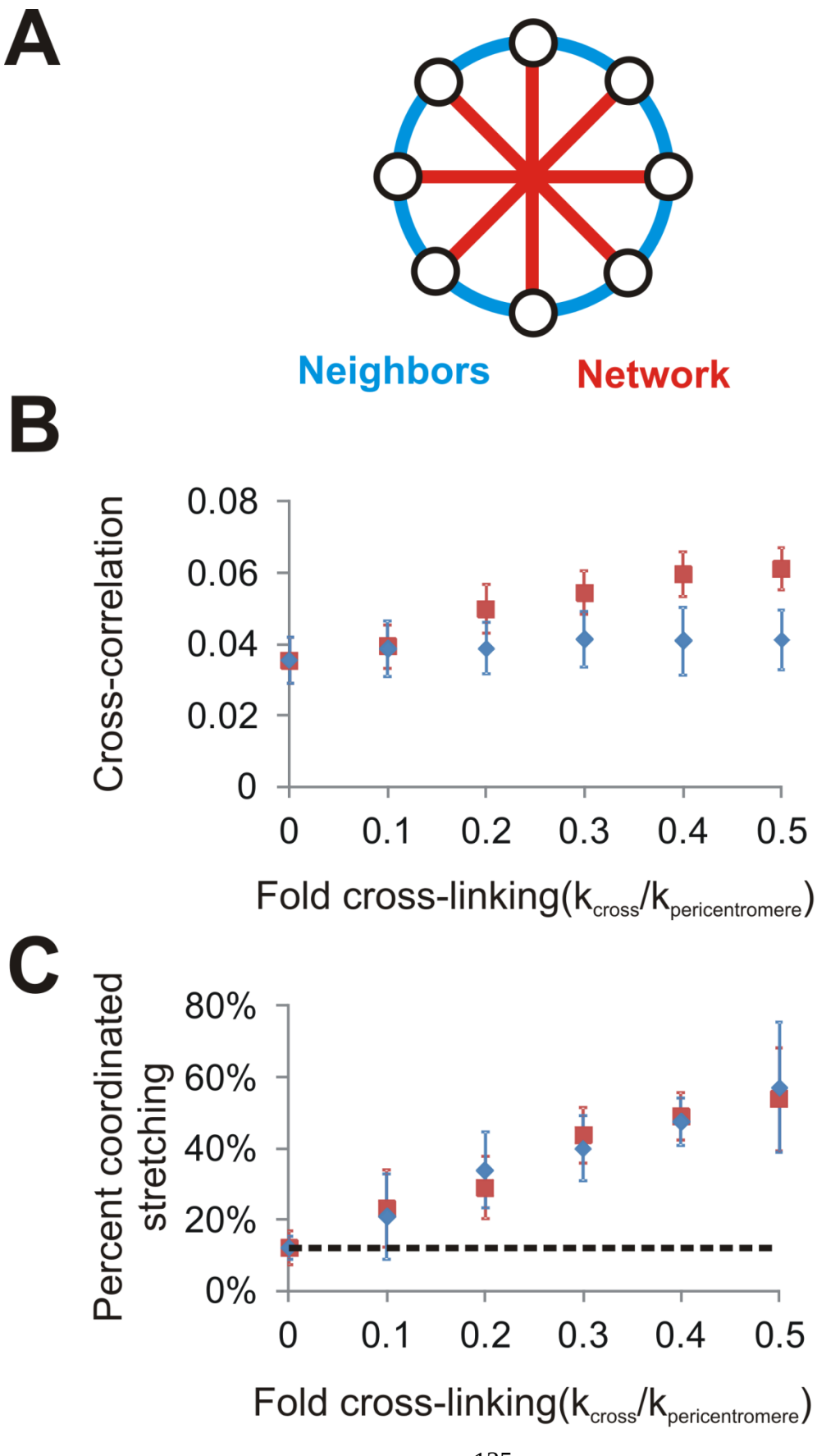
A
Neighbors
Network
B
Cross-correlation
0.08
0.06
0.04
0.02
0
0
0.1
0.2
0.3
0.4
0.5
Fold cross-linking(k_cross/k_pericentromere)
C
Percent coordinated stretching
80%
60%
40%
20%
0%
0
0.1
0.2
0.3
0.4
0.5
Fold cross-linking(k_cross/k_pericentromere)

Figure 3.3 Simulation of cross-linking springs between pericentromeres recapitulates correlated movement and stretching

A mathematical model of spindle length force balance, including kMT dynamics and a non-linear spring, was used to simulate the results of adding cross-linking springs between pericentromeres (Stephens et al., 2013). (A)Springs were added to cross-link neighbors (blue) or all pericentromeres (red) into a network. Graphs show (B) cross-correlation of kMT plus-end movements or (C) coordinated stretching upon increasing the cross-linking spring constant (k_{cross}) relative to the pericentromere spring constant ($k_{pericentromere}$, n = 500). Simulated cross-correlation of kMTs does not match experimentally measured absolute values of chromatin. The movement of the chromatin polymer is not specified in the simulation. A threshold determines the state of a piecewise continuous spring. Below the threshold a compact spring has a high spring constant and above the threshold the stretched spring has a lower spring constant. All simulations had a 12 ± 2% single pericentromere stretching frequency (dotted line) similar to *in vivo* wild-type. Error bars represent standard deviation.

Cohesin and condensin promote physical interaction between pericentromeres

To determine if pericentromeres are in physical proximity in metaphase we adapted the 3C (Chromosome Conformation Capture) technique to probe the interaction between two loci on different chromosomes. Inverse primer pairs used to map the interaction of chromatin are shown in Figure 3.4 A (pericentric chromatin P_U, P_D; arm chromatin A_U, A_D; see Materials and methods). We find a WT pericentromere interaction index of 1.75 ± 0.05 (P/A, normalized to arm 1.00, n = 10; Yeh et al., 2008).

The basis for physical interaction could reflect centromere clustering and/or protein-mediated pericentromere interaction. We disrupted the centromere of chromosome III using a conditionally functional centromere (GALCEN 3; Hill and Bloom, 1987). The intermolecular interaction of pericentromeres is dependent on a functional centromere (GALCEN 3 1.21 ± 0.02, n = 2, $P < 1\times10^{-7}$, Figure 3.4 B). Thus centromere clustering is one mechanism for physical interaction. The two major structural proteins enriched in the pericentromere are cohesin and condensin (Megee et al., 1999; Tanaka et al., 1999; Wang et al., 2005; D'Ambrosio et al., 2008). Depletion of condensin (*brn1-9*, Lavoie et al., 2000) yields a decrease in pericentromere interaction to 1.44 ± 0.05 (n = 10, P< 0.001, Figure 3.4 B). Deletion of Mcm21, a non-essential kinetochore protein, results in a threefold depletion of pericentric cohesin but maintains arm cohesin (Eckert et al., 2007; Ng et al., 2009). This mutant resulted in a decrease of 4C interaction to 1.28, similar to GALCEN3 (*mcm21Δ* 1.28 ± 0.05 n = 10, P > 0.05 vs. GalCEN 3 1.21; Figure 3.4 B). Thus physical interactions between pericentromeres are dependent on clustering of centromeres to the spindle poles via kinetochore microtubules as well as recruitment of pericentric cohesin and to a lesser extent condensin.

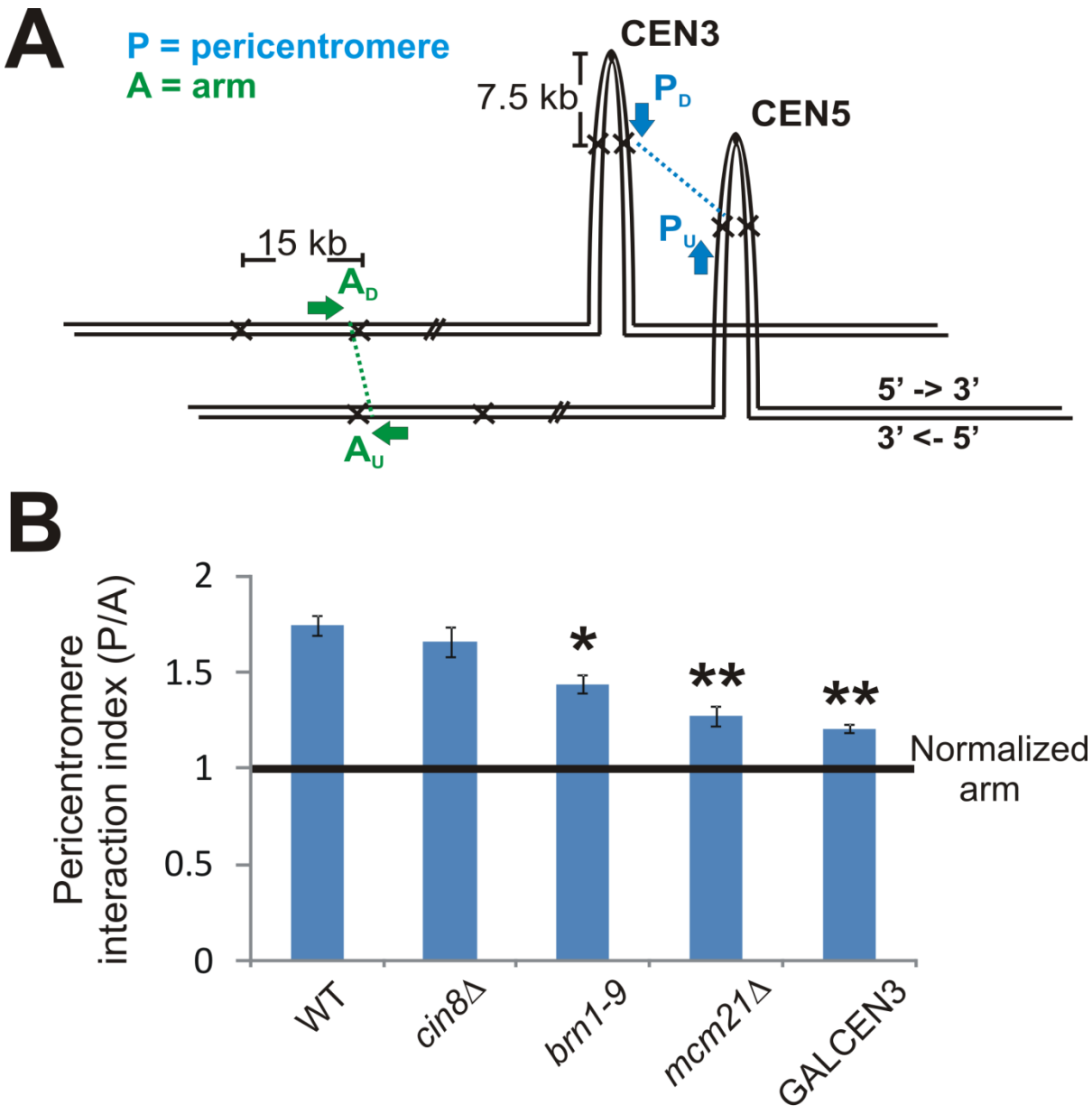
A
P = pericentromere
A = arm
CEN3
7.5 kb
P_D
CEN5
P_U
15 kb
A_D
A_U
5' -> 3'
3' <- 5'
B
Pericentromere interaction index (P/A)
2
1.5
1
0.5
0
*
**
**
Normalized arm
WT
cin8Δ
brn1-9
mcm21Δ
GALCEN3

Figure 3.4 Chromosome to Chromosome Conformation Capture (4C) reveals interactions between pericentromeres of different chromosomes

(A) Diagram of primer locations used to assay interactions, via 3C technique, between the arms (A, green) and pericentromeres (P, blue) of chromosome III and V (see Materials and Methods). (B) The interaction index is the ratio of the pericentromere (P) to the arm (A) PCR product normalized to 1 and is standardized for primer efficiency and input. Pericentromere interaction index is shown for WT, *cin8Δ*, *brn1-9*, *mcm21Δ*, and GALCEN 3 (conditionally off centromere). Asterisks denote statistically significantly different ($\chi^2 < 0.01$). Values listed in Table 3.1. Error bars represent standard deviation.

Cohesin and condensin serve distinct inter-pericentromere functions

The spatial segregation of cohesin and condensin around the spindle axis (Stephens et al., 2011) and the extent to which they aid inter-chromosomal interactions (4C) may reflect their different functional roles in the pericentromere. We probed potential distinctions by assaying pericentromere dynamics in cohesin and condensin mutants. Correlated motion analysis provides comparison of the behavior of compact arrays. Depletion of condensin resulted in a significant decrease in correlated movement of different pericentromeres (WT 0.33 to *brn1-9* 0.21 ± 0.35, $n = 58$, $P < 0.05$). In contrast, depletion of pericentric cohesin did not decrease correlated motion (*mcm21Δ* 0.36 ± 0.31, $n = 54$, $P > 0.05$, Figure 3.5 A). Correlated motions of LacO/TetO labels in the same pericentromere are not altered in either mutant compared to wild-type ($P > 0.05$, Figure 3.5 B). Thus condensin functions to cross-link pericentromeres of different chromosomes when compact and upon its depletion compact pericentromeres are less correlated in their movements.

Depletion of either pericentric cohesin or condensin results in increased single pericentromere stretching 45-55% (Figure 3.5 D, dotted lines; Stephens et al., 2011). Dependent/linked stretching is lost upon depletion of pericentric cohesin (*mcm21Δ*: single 44% vs. coordinated 44%, $\chi^2 = 1$, Figure 3.5 D and Table 3.1). Oppositely, condensin mutants maintain dependent/linked stretching similar to wild-type (*brn1-9*: single 56% vs. coordinated 65%, $\chi^2 < 0.001$, Figure 3.5 D and Table 3.1). Therefore, cohesin is more likely to cross-link distal pericentromeres and upon its depletion pericentromeres stretch independently.

Inter-pericentromere dynamics are also dependent on the microtubule motor Cin8

Coordinated dynamics may also reflect cross-links in the kinetochore or kinetochore microtubule (kMT). The kinesin 5 motor Cin8 clusters kinetochores in yeast (Tytell and Sorger, 2006; Gardner et al., 2008). Pericentromere interaction via 4C does not significantly decrease in *cin8Δ* cells (Figure 3.4 B, $P > 0.01$). To deduce the role of Cin8 in pericentromere dynamics, we tracked pericentromere motion and stretching in *cin8Δ* cells. The correlated movement of trans labels was reduced in *cin8Δ* (0.23 ± 0.35, $n = 96$, $P < 0.05$, Figure 3.5 A). Deletion of *KIP1* had an insignificant affect on correlated movement (*kip1Δ* 0.29 ± 0.33, $n = 36$, $P > 0.05$, Figure 3.5 A) which suggests that *cin8Δ* is likely influencing coordination through its role in maintaining kinetochore clustering.

The heterogeneous distribution of kMTs in *cin8Δ* cells may also result in loss of dependent coordinated stretching. Cells deleted of either *CIN8* or *KIP1* have shorter spindles, reflecting fewer motors binding to and sliding interpolar microtubules apart. The shorter spindles result in less stretching of the pericentric chromatin (CEN 11 and 15, 4-6%, Figure 3.5 D, dotted lines). Dependent stretching is lost in *cin8Δ* cells (6% single vs. 4% coordinated, $\chi^2 = 0.46$, Figure 3.5 D and Table 3.1). Oppositely, *kip1Δ* cells maintained a higher frequency of trans coordinated stretching similar to WT dependent/linked behavior (single 4% vs. coordinated 26%, $\chi^2 < 0.001$, Figure 3.5 D and Table 3.1). The maintenance of kinetochore length distributions by Cin8 contributes to correlated motion and coordinated stretching of pericentromeres.

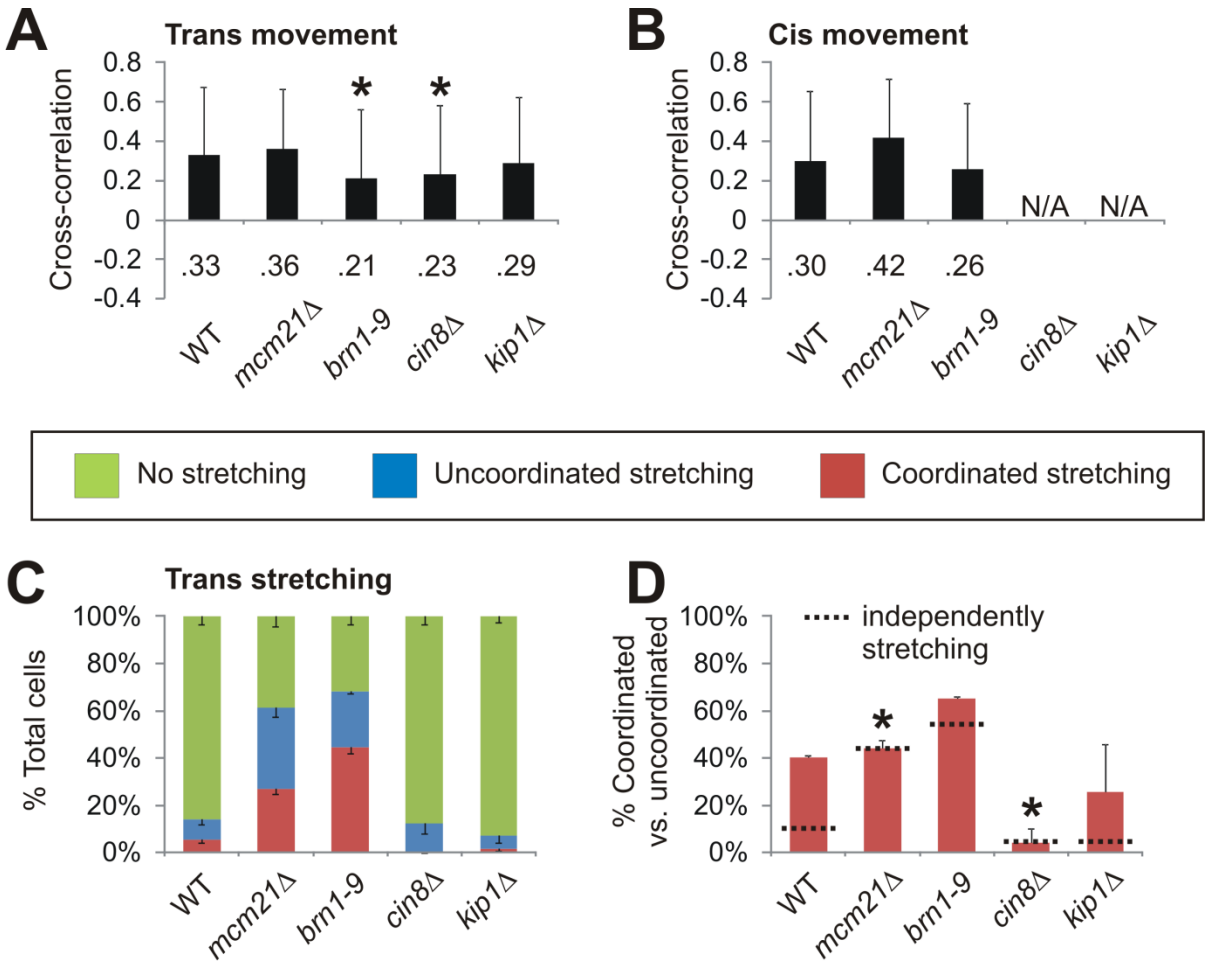
A
Trans movement
Cross-correlation
0.8
0.6
0.4
0.2
0
-0.2
-0.4
.33
.36
.21
.23
.29
*
*
WT
mcm21Δ
brn1-9
cin8Δ
kip1Δ
B
Cis movement
Cross-correlation
0.8
0.6
0.4
0.2
0
-0.2
-0.4
.30
.42
.26
N/A
N/A
WT
mcm21Δ
brn1-9
cin8Δ
kip1Δ
No stretching
Uncoordinated stretching
Coordinated stretching
C
Trans stretching
% Total cells
100%
80%
60%
40%
20%
0%
WT
mcm21Δ
brn1-9
cin8Δ
kip1Δ
D
% Coordinated vs. uncoordinated
100%
80%
60%
40%
20%
0%
independently stretching
*
*
WT
mcm21Δ
brn1-9
cin8Δ
kip1Δ

Figure 3.5 Cohesin, condensin, and Cin8 coordinated inter-pericentromere dynamics Metaphase spindles were analyzed for (A)trans or (B) cis cross-correlation of foci movement relative to their respective spindle pole and (C, D) coordinated stretching of pericentromeres on different chromosomes (trans) in chromatin mutants (pericentric cohesin, *mcm21Δ*; condensin, *brn1-9*) or microtubule motor deletions (*cin8Δ*, *kip1Δ*). (A, B) An asterisk denotes significantly different cross-correlation from WT (t-test, $P < 0.05$). (C, D) Mutants were analyzed for stretching of trans pericentromere labeled cells and were categorized as No stretch (green), Uncoordinated (blue), or Coordinated (red). Asterisk denotes mutants in which single pericentromere stretching (black line) and coordinated stretching frequency (red bar) are statistically similar ($\chi^2 > 0.4$) and thus stretching is independent. Average values are listed in Table 3.1. Error bars represent standard deviation.

Table 3.1 Summary of inter-pericentromere dynamics and interaction

	Trans correlated movement average(R)	**Single pericentromere stretching average (%)**	**Trans coordinated stretching average(%)**	**Pericentromere interaction index average(4C)**
WT	0.33	11	40	1.75
mcm21Δ	0.36	44	44 *	1.28 **
brn1-9	0.21 *	56	65	1.44 *
cin8Δ	0.23 *	6	4 *	1.66
kip1Δ	0.29	4	26	NA

*/** denotes statistically significant change from WT

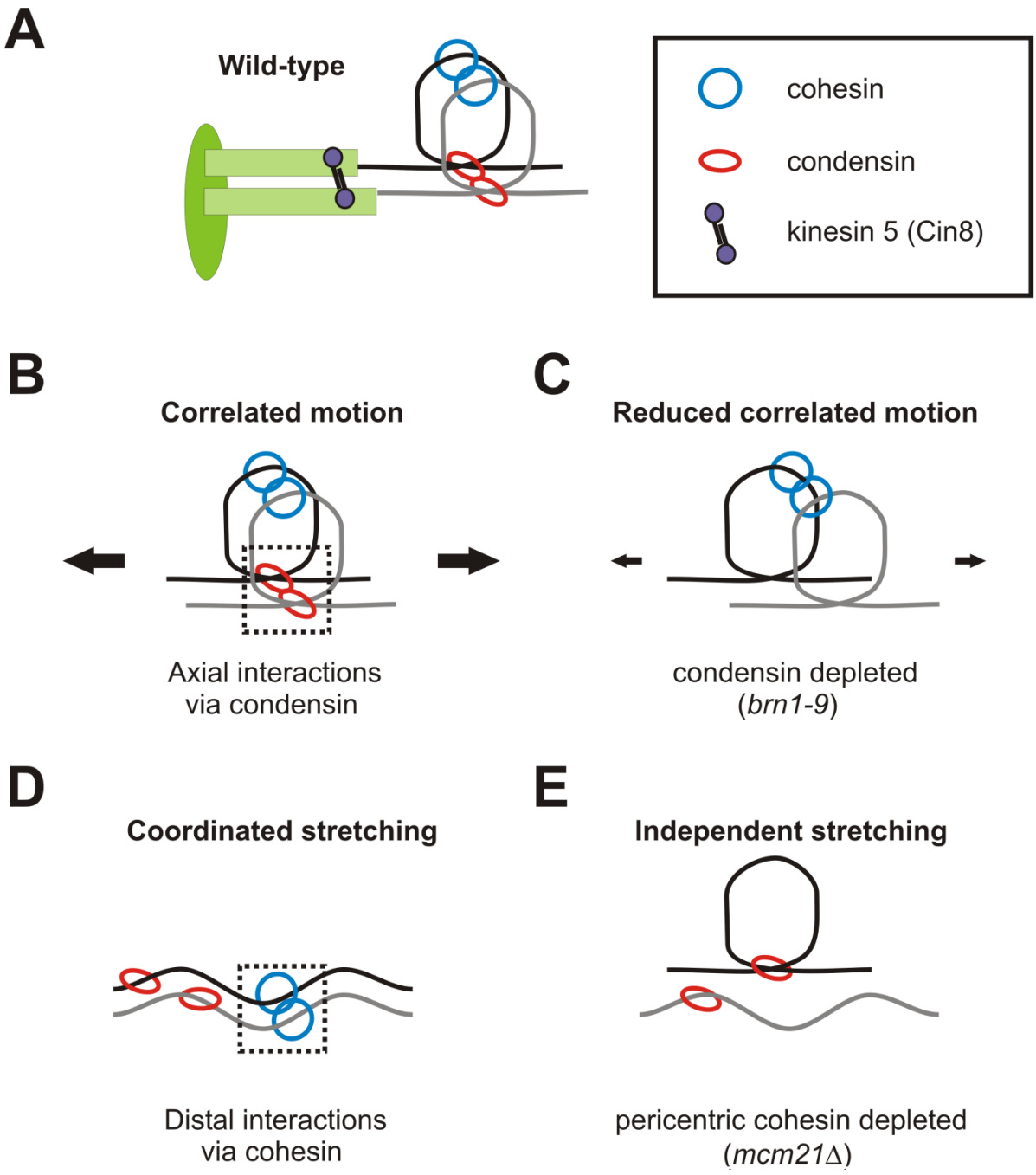
A
Wild-type
cohesin
condensin
kinesin 5 (Cin8)
B
Correlated motion
Axial interactions
via condensin
C
Reduced correlated motion
condensin depleted
(brn1-9)
D
Coordinated stretching
Distal interactions
via cohesin
E
Independent stretching
pericentric cohesin depleted
(mcm21Δ)

Figure 3.6 Model of cross-linking in the metaphase spindle apparatus

(A) Diagram of wild-type metaphase spindle structure and interactions. Kinetochore microtubules (light green) emanating from the spindle pole (dark green) are cross-linked via the kinesin 5 motor Cin8 (purple) while multiple non-linear (looped) pericentric chromatin springs (gray and black) are cross-liked via condensin (red) at the base and cohesin (blue) radially displaced (Stephens et al., 2011). (B) Condensin functions as an axial cross-linker between compact pericentromeres of different chromosomes to correlate their movement during metaphase. (C) Loss of condensin cross-links results in decreased correlated motion (smaller arrows; Figure 3.5 A). (D) Cohesin functions primarily as a distal cross-linker between pericentromeres resulting in coordinated stretching. (E) Loss of pericentric cohesin results in pericentromeres stretching independently (one stretched, one compact; Figure 3.5 D).

Discussion

Tension at the kinetochore is necessary to signal the proper alignment of chromosomes for faithful segregation. However, the cell must sense tension over many microtubule attachments in a cluster of 16 chromosomes in the yeast spindle or 16-20 microtubule attachments in a mammalian kinetochore. Since, individual microtubules continue to exhibit dynamic instability when sister chromatids are bioriented (Pearson et al., 2006), it is not clear how differences in kMT growth and shortening are averaged over the cluster of bioriented kinetochores. Cross-linking between chromatin could equalize dynamics and tension throughout multiple attachments. Through the unique ability to examine chromatin proximal to different microtubule attachments in a cluster of 16 kMTs, we show that pericentromeres exhibit coordinated behavior and physically interact. This provides evidence that instead of 16 independent springs, there is a cross-linked network between sister kinetochores. This network is dependent on cohesin, condensin and the kinesin 5 motor Cin8. Condensin localizes to the spindle axis where it compacts the pericentromere via looping as well as links pericentromeres of different chromosomes axially (Figure 3.6, B and C). Cohesin is radially displaced from the spindle axis and most likely tethers pericentromere loops confining them to the spindle and distributing tension throughout the network (Figure 3.6, D and E). The chromatin spring's resistive properties likely come from compaction and cross-linking of pericentromeres through condensin and cohesin (Figure 3.6; Guacci et al., 1997; Lavoie et al., 2002; Lavoie et al., 2004; Lam et al., 2006; Heidinger-Pauli et al., 2010; Cuylen et al., 2011; Stephens et al., 2011; Stephens et al., 2013). The chromatin spring is essential for proper tension sensing and faithful segregation of the genome in yeast (Yong-

Gonzalez et al., 2007; Ng et al., 2009; Stephens et al., 2011) and mammals (Samoshkin et al., 2009; Uchida et al., 2009; Ribeiro et al., 2009; Manning et al., 2010). The segregation apparatus allows for a variable number of microtubule attachments by generating an interlinked network in the chromatin critical for a tension sensing mechanism.

Materials and methods

Strain Construction

To build a strain with pericentric regions labeled on two different chromosomes, we incorporated a 8 kb TetO array 0.5 kb away from CEN 11 (at the met14 locus), using the plasmid protocol from the Gasser lab (Rohner et al., 2008), into a strain containing a 10 kb LacO array tagged with LacI-GFP 1.8 kb from CEN 15 (Goshima and Yanagida, 2000). A target fragment with homology to the met14 locus was transformed into the 1.8 kb LacO strain. The plasmid pSR14 (TetO) with homology to the target fragment was transformed into the strain. We then transformed pDB49 (TetR-CFP) into the stain to visualize the TetO. Similarly a strain was created with the 8 kb TetO array 0.5 kb from CEN 11 directed into a strain containing a 10 kb LacO array 3.8 kb from CEN 3 (Goshima and Yanagida, 2000). A strain with two arrays on the same chromosome (TetO array 4.5 kb from CEN 11 and a LacO array 9.4 kb from CEN 11) was constructed by inserting a 8kb TetO array centromere proximal to a 1.7 kb LacO array (Pearson et al., 2001) using the same protocol.

Cell preparation

WT, *cin8Δ*, *kip1Δ*, and *mcm21Δ* strains were grown at 24°C in SD-His. Temperature sensitive allele b*rn1-9* strains were grown at 24°C and then transferred to restrictive

temperatures (37°C) for three hours prior to imaging. Cells were grown to log phase as asynchronous cultures then prepared for imaging.

Microscopy

Images were obtained using a microscope stand (Eclipse TE2000-U; Nikon) with a 100x Plan Apo 1.4 NA digital interference contrast oil immersion lens with a camera (Orca ER; Hamamatsu Photonics) at 25°C. Images were acquired using Metamorph 7.1 (Molecular Devices) and were binned 2x2 (pixel size of 130 nm). Images were taken in water on .135 mm coverslips. Time lapse images were obtained in a single z plane at 15 and 30 second intervals with exposure times of 600 ms for CFP, 600 ms for YFPg, 800 ms for RFP, and 250 ms for trans images. Population images were obtained in z series stacks of ten images with a step size of 200 nm and similar exposure times as time lapse images.

Cross-correlation analysis of pericentromere movement

Time lapse images of the CEN 15/CEN 11 strain were rotated and aligned relative to the spindle axis using MATLAB (Math Works, Inc.). Aligned images were used to analyze foci movement relative to the spindle axis (x axis), eliminating movement perpendicular to the spindle (y axis). Correlation was determined in cells with two separated foci for both LacO and TetO arrays. The distance of the foci to their respective pole was measured using Metamorph 7.1 and logged into Excel (Microsoft) where cross-correlation analysis was performed using the CORREL function. Cells displaying both arrays separated and maintaining a constant spindle length over the time lapse were considered metaphase.

Coordination of stretching

Pericentromere LacO/TetO array stretching was analyzed in metaphase cells. Cells were considered metaphase if both LacO and TetO arrays displayed separated sisters and

spindles did not exhibit anaphase-like linear increases in spindle length. Stretching events were determined as cells with one focus and another fluorescent signal that is linear along the spindle axis (Stephens et al., 2011; Stephens et al., 2013). Stretching events are determined by measuring the Gaussian of the fluorescence signal parallel and perpendicular to the spindle axis. Compact pericentromeres will appear as a focus and have an aspect ratio of <1.2 (parallel/perpendicular). Stretched arrays appear as lines and have an aspect ratio of >1.2.

Simulations of movement and stretching

Simulations were run in MATLAB/Simulink using a mathematical model of mitotic force balance in the yeast spindle including kMT dynamics and a non-linear spring (Stephens et al., 2013). Cross-links were added to the models as follows: For neighbors the difference in a pericentromere spring length (L) compared to its two adjacent spring (+/- 1) lengths was calculated, converted into force, and added to pericentromere spring force: $F_{total} = -k_{spring}(L_i - L_{rest}) + k_{cross\text{-}link}\ [[L_i - (L_{i+1})]+[\ L_i\ - (L_{i-1})]\ )]$. For a network the difference between each spring (n) and the other 15 was calculated, converted into force, and added to pericentromere spring force: $F_{total} = -k_{spring}(L_i - L_{rest}) + k_{cross\text{-}link}\ [\Sigma\ [L_i - (Lj)]]$, for $j \neq i$.

Chromosome to chromosome conformation capture (4C)

Yeast nuclei were prepared and cross-linked with 1% formaldehyde for 10 min at room temperature. The reaction was quenched with the addition of glycine to 0.25 M. Nuclei were washed and resuspended in appropriate 1X restriction digest buffer. One percent SDS was added, and the nuclei were incubated at 65°C for 10 min to remove uncross-linked proteins. Triton X-100 was added to a final concentration of 1% to remove the SDS and allow for subsequent digestion. Sixty units of the restriction enzyme XbaI were added, and the reaction was incubated overnight at 37°C. Ten percent SDS was added to each tube and

incubated at 65C for 20 min to inactivate XbaI. Eight hundred Weiss Units of T4 DNA ligase were added, and the reaction was incubated at 16°C for 2 hours to ligate cross-linked DNA. Cross-links were then reversed with the addition of proteinase K and overnight incubation at 65°C. DNA was purified by phenolchloroform extraction and ethanol precipitation. DNA concentration was determined by running of 1% agarose gels and staining with ethidium bromide. All gels were imaged with an Alpha Innotech AlphaImager 2200 imaging system, and all images were imported into Metamorph 6.1 for analysis. Gels were analyzed by measurement of the integrated intensity of a band and correcting for background as described in (Joglekar et al., 2006; Yeh et al., 2008).

Titration PCRs were performed with increasing amounts of input DNA. Input-DNA volumes that yielded PCR products that were within the linear range of PCR amplification were then used for 4C analysis. The cross-linking frequencies of regions between chromosomes III to V were compared in the arm and the pericentromere. The centromere 3 primer (P_D) 1422 base pairs downstream of CEN3 was paired with a centromere 5 primer (P_U) 1913 base pairs upstream of CEN5. The arm region was probed with a chromosome 3 primer (A_D) 75,639 bp from CEN3 and a chromosome 5 primer (A_U) 98,424 bp from CEN5. Ligation products from these regions are detected by PCR, yielding products approximately 500–700 base pairs in size (representing the distance of each primer to the *Xba*I site). Nonspecific PCR products were not generated in any of the experiments. PCR products from cross-linked DNA were compared to identical products generated from control DNA, which was not cross-linked, allowing all possible ligation products to occur. Analysis of the resultant PCR products showed an average 75% increase in PCR product for the pericentric

region as compared to the region along the arm, indicating a statistically significant increase in physical interaction of the genome at pericentric chromatin versus random in the arm.

Strains

KBY 9199 MATa, ade2-101, his3-11, trp1-1, ura3-1, leu2-3,112 can1, LacINLSGFP:HIS3, LacO::URA3(at 1.8kb from CEN15, 10kb array), pRS14 TetO-Leu (at met 14 0.5kb from CEN 11, 8kb array), TetRCFP-Hb, Hb::Kan, Spc29RFP:Hb

KBY 9406 MATa, ade2-101, his3-11, trp1-1, ura3-1, leu2-3,112 can1, LacINLSGFP:HIS3, LacO::URA3(at 1.8kb from CEN15, 10kb array), pRS14 TetO-Leu (at met 14 0.5kb from CEN 11, 8kb array), TetRCFP-Hb, Hb::Kan, Spc29RFP:Hb, *mcm21Δ*::Nat

KBY 9407 MATa, ade2-101, his3-11, trp1-1, ura3-1, leu2-3,112 can1, LacINLSGFP:HIS3, LacO::URA3(at 1.8kb from CEN15, 10kb array), pRS14 TetO-Leu (at met 14 0.5kb from CEN 11, 8kb array), TetRCFP-Hb, Hb::Kan, Spc29RFP:Hb, *brn1-9*-Nat

KBY 9449 MATa, ade2-101, his3-11, trp1-1, ura3-1, leu2-3,112 can1, LacINLSGFP:HIS3, LacO::URA3(at 1.8kb from CEN15, 10kb array), pRS14 TetO-Leu (at met 14 0.5kb from CEN 11, 8kb array), TetRCFP-Hb, Hb::Kan, Spc29RFP:Hb, Leu::Nat, *kip1Δ*-Trp

KBY 9450 MATa, ade2-101, his3-11, trp1-1, ura3-1, leu2-3,112 can1, LacINLSGFP:HIS3, LacO::URA3(at 1.8kb from CEN15, 10kb array), pRS14 TetO-Leu (at met 14 0.5kb from CEN 11, 8kb array), TetRCFP-Hb, Hb::Kan, Spc29RFP:Hb, Leu::Nat, *cin8Δ*-Leu

KBY 9402 MATa, ade2-101, his3-11, trp1-1, ura3-1, leu2-3,112 can1, LacINLSGFP:HIS3, LacO::URA3(at 3.8kb from CEN3, 10kb array), TetO-Leu (at met 14 0.5kb from CEN 11, 8kb array), TetRCFP-Hb, Hb::Kan, Spc29RFP:Hb

KBY 9424 MATa, ade1, met14, ura3-52, leu2-3,112 his3-11,15 lys2D::lacI-GFP-NLS-NATr met14::lacO(at 0.6kb from CEN11, 1.2kb array) SPC29-GFP-KANr, Trp::Ura, pSR8 TetO-

His3(at 0.5kb from CEN11, 8kb array) at Met14, Hg::Trp1, pDB49 TetR-CFP-Hg, Hg::Leu, Spc29-GFP-KAN::Spc29-RFP-Hb, Nat::Kan

KBY 9427 MATa, ade1, met14, ura3-52, leu2-3,112 his3-11,15 lys2D::lacI-GFP-NLS-NATr met14::lacO(at 0.6kb from CEN11, 1.2kb array) SPC29-GFP-KANr, Trp::Ura, pSR8 TetO-His3(at 0.5kb from CEN11, 8kb array) at Met14, Hg::Trp1, pDB49 TetR-CFP-Hg, Hg::Leu, Spc29-GFP-KAN::Spc29-RFP-Hb, Nat::Kan, *mcm21Δ*::Nat

KBY 9433 MATa, ade1, met14, ura3-52, leu2-3,112 his3-11,15 lys2D::lacI-GFP-NLS-NATr met14::lacO(at 0.6kb from CEN11, 1.2kb array) SPC29-GFP-KANr, Trp::Ura, pSR8 TetO-His3(at 0.5kb from CEN11, 8kb array) at Met14, Hg::Trp1, pDB49 TetR-CFP-Hg, Hg::Leu, Spc29-GFP-KAN::Spc29-RFP-Hb, Nat::Kan, *brn1-9*-Nat

YEF473 MATa, trp1-63, leu2Δ1, ura3-52, his2-200, lys 2-801 (Pringle lab)

KBY 8005 (YEF473A) *cin8Δ*-Leu

KBY 9053 (YEF473A) *brn1-9*-NAT, Spc29-RFP-Hb, Nuf2-GFP-URA

KBY 9070 (YEF 473A) *mcm21*::Nat, Spc29-RFP-Hb, Nuf2-GFP-URA

KBY8126 (YEF 473A) Ame1-GFP:Kan, Spc29-RFP:Hb, JC313 GALCEN3-Ura

References

Bachant, J., A. Alcasabas, Y. Blat, N. Kleckner, and S.J. Elledge. 2002. The SUMO-1 isopeptidase Smt4 is linked to centromeric cohesion through SUMO-1 modification of DNA topoisomerase II. *Mol Cell*. 9:1169-82.

Bloom, K., and E. Yeh. 2010. Tension management in the kinetochore. *Curr Biol*. 20:R1040-8.

Cuylen, S., J. Metz, and C.H. Haering. 2011. Condensin structures chromosomal DNA through topological links. *Nat Struct Mol Biol*. 18:894-901.

D'Ambrosio, C., C.K. Schmidt, Y. Katou, G. Kelly, T. Itoh, K. Shirahige, and F. Uhlmann. 2008. Identification of cis-acting sites for condensin loading onto budding yeast chromosomes. *Genes Dev*. 22:2215-27.

Eckert, C.A., D.J. Gravdahl, and P.C. Megee. 2007. The enhancement of pericentromeric cohesin association by conserved kinetochore components promotes high-fidelity chromosome segregation and is sensitive to microtubule-based tension. *Genes Dev*. 21:278-91.

Fitzgerald-Hayes, M., L. Clarke, and J. Carbon. 1982. Nucleotide sequence comparisons and functional analysis of yeast centromere DNAs. *Cell*. 29:235-44.

Freeman, L., L. Aragon-Alcaide, and A. Strunnikov. 2000. The condensin complex governs chromosome condensation and mitotic transmission of rDNA. *J Cell Biol*. 149:811-24.

Gardner, M.K., D.C. Bouck, L.V. Paliulis, J.B. Meehl, E.T. O'Toole, J. Haase, A. Soubry, A.P. Joglekar, M. Winey, E.D. Salmon, K. Bloom, and D.J. Odde. 2008. Chromosome congression by Kinesin-5 motor-mediated disassembly of longer kinetochore microtubules. *Cell*. 135:894-906.

Goshima, G., and M. Yanagida. 2000. Establishing biorientation occurs with precocious separation of the sister kinetochores, but not the arms, in the early spindle of budding yeast. *Cell*. 100:619-33.

Guacci, V., D. Koshland, and A. Strunnikov. 1997. A direct link between sister chromatid cohesion and chromosome condensation revealed through the analysis of MCD1 in S. cerevisiae. *Cell*. 91:47-57.

He, X., S. Asthana, and P.K. Sorger. 2000. Transient sister chromatid separation and elastic deformation of chromosomes during mitosis in budding yeast. *Cell*. 101:763-75.

Heidinger-Pauli, J.M., O. Mert, C. Davenport, V. Guacci, and D. Koshland. 2010. Systematic reduction of cohesin differentially affects chromosome segregation, condensation, and DNA repair. *Curr Biol*. 20:957-63.

Hill, A., and K. Bloom. 1987. Genetic manipulation of centromere function. *Mol Cell Biol*. 7:2397-405.

Hirano, T., R. Kobayashi, and M. Hirano. 1997. Condensins, chromosome condensation protein complexes containing XCAP-C, XCAP-E and a Xenopus homolog of the Drosophila Barren protein. *Cell*. 89:511-21.

Joglekar, A.P., D.C. Bouck, J.N. Molk, K.S. Bloom, and E.D. Salmon. 2006. Molecular architecture of a kinetochore-microtubule attachment site. *Nat Cell Biol*. 8:581-5.

Kimura, K., and T. Hirano. 1997. ATP-dependent positive supercoiling of DNA by 13S condensin: a biochemical implication for chromosome condensation. *Cell*. 90:625-34.

Lam, W.W., E.A. Peterson, M. Yeung, and B.D. Lavoie. 2006. Condensin is required for chromosome arm cohesion during mitosis. *Genes Dev*. 20:2973-84.

Lavoie, B.D., E. Hogan, and D. Koshland. 2002. In vivo dissection of the chromosome condensation machinery: reversibility of condensation distinguishes contributions of condensin and cohesin. *J Cell Biol*. 156:805-15.

Lavoie, B.D., E. Hogan, and D. Koshland. 2004. In vivo requirements for rDNA chromosome condensation reveal two cell-cycle-regulated pathways for mitotic chromosome folding. *Genes Dev*. 18:76-87.

Lavoie, B.D., K.M. Tuffo, S. Oh, D. Koshland, and C. Holm. 2000. Mitotic chromosome condensation requires Brn1p, the yeast homologue of Barren. *Mol Biol Cell*. 11:1293-304.

Manning, A.L., M.S. Longworth, and N.J. Dyson. 2010. Loss of pRB causes centromere dysfunction and chromosomal instability. *Genes Dev*. 24:1364-76.

Maresca, T.J., and E.D. Salmon. 2010. Welcome to a new kind of tension: translating kinetochore mechanics into a wait-anaphase signal. *J Cell Sci*. 123:825-35.

Megee, P.C., C. Mistrot, V. Guacci, and D. Koshland. 1999. The centromeric sister chromatid cohesion site directs Mcd1p binding to adjacent sequences. *Mol Cell*. 4:445-50.

Michaelis, C., R. Ciosk, and K. Nasmyth. 1997. Cohesins: chromosomal proteins that prevent premature separation of sister chromatids. *Cell*. 91:35-45.

Nativio, R., K.S. Wendt, Y. Ito, J.E. Huddleston, S. Uribe-Lewis, K. Woodfine, C. Krueger, W. Reik, J.M. Peters, and A. Murrell. 2009. Cohesin is required for higher-order chromatin conformation at the imprinted IGF2-H19 locus. *PLoS Genet*. 5:e1000739.

Ng, T.M., W.G. Waples, B.D. Lavoie, and S. Biggins. 2009. Pericentromeric sister chromatid cohesion promotes kinetochore biorientation. *Mol Biol Cell*. 20:3818-27.

O'Toole, E.T., M. Winey, and J.R. McIntosh. 1999. High-voltage electron tomography of spindle pole bodies and early mitotic spindles in the yeast Saccharomyces cerevisiae. *Mol Biol Cell*. 10:2017-31.

Pearson, C.G., and K. Bloom. 2004. Dynamic microtubules lead the way for spindle positioning. *Nat Rev Mol Cell Biol*. 5:481-92.

Pearson, C.G., M.K. Gardner, L.V. Paliulis, E.D. Salmon, D.J. Odde, and K. Bloom. 2006. Measuring nanometer scale gradients in spindle microtubule dynamics using model convolution microscopy. *Mol Biol Cell*. 17:4069-79.

Pearson, C.G., P.S. Maddox, E.D. Salmon, and K. Bloom. 2001. Budding yeast chromosome structure and dynamics during mitosis. *J Cell Biol*. 152:1255-66.

Peterson, J.B., and H. Ris. 1976. Electron-microscopic study of the spindle and chromosome movement in the yeast Saccharomyces cerevisiae. *J Cell Sci*. 22:219-42.

Ribeiro, S.A., J.C. Gatlin, Y. Dong, A. Joglekar, L. Cameron, D.F. Hudson, C.J. Farr, B.F. McEwen, E.D. Salmon, W.C. Earnshaw, and P. Vagnarelli. 2009. Condensin regulates the stiffness of vertebrate centromeres. *Mol Biol Cell*. 20:2371-80.

Rohner, S., S.M. Gasser, and P. Meister. 2008. Modules for cloning-free chromatin tagging in Saccharomyces cerevisae. *Yeast*. 25:235-9.

Samoshkin, A., A. Arnaoutov, L.E. Jansen, I. Ouspenski, L. Dye, T. Karpova, J. McNally, M. Dasso, D.W. Cleveland, and A. Strunnikov. 2009. Human condensin function is essential for centromeric chromatin assembly and proper sister kinetochore orientation. *PLoS One*. 4:e6831.

Stephens, A.D., J. Haase, L. Vicci, R.M. Taylor, 2nd, and K. Bloom. 2011. Cohesin, condensin, and the intramolecular centromere loop together generate the mitotic chromatin spring. *J Cell Biol*. 193:1167-80.

Stephens, A.D., R.A. Haggerty, P.A. Vasquez, L. Vicci, C.E. Snider, F. Shi, C.W. Quammen, C. Mullins, J. Haase, R.M. Taylor, J.S. Verdaasdonk, M.R. Falvo, Y. Jin, M.G. Forest, and K. Bloom. 2013. Pericentric Chromatin Loops Function as a Non-linear Spring in Mitotic Force Balance *J Cell Biol*. 200:757-72.

Sutani, T., T. Yuasa, T. Tomonaga, N. Dohmae, K. Takio, and M. Yanagida. 1999. Fission yeast condensin complex: essential roles of non-SMC subunits for condensation and Cdc2 phosphorylation of Cut3/SMC4. *Genes Dev*. 13:2271-83.

Tanaka, T., M.P. Cosma, K. Wirth, and K. Nasmyth. 1999. Identification of cohesin association sites at centromeres and along chromosome arms. *Cell*. 98:847-58.

Tanaka, T., J. Fuchs, J. Loidl, and K. Nasmyth. 2000. Cohesin ensures bipolar attachment of microtubules to sister centromeres and resists their precocious separation. *Nat Cell Biol*. 2:492-9.

Tytell, J.D., and P.K. Sorger. 2006. Analysis of kinesin motor function at budding yeast kinetochores. *J Cell Biol*. 172:861-74.

Uchida, K.S., K. Takagaki, K. Kumada, Y. Hirayama, T. Noda, and T. Hirota. 2009. Kinetochore stretching inactivates the spindle assembly checkpoint. *J Cell Biol*. 184:383-90.

Wang, B.D., D. Eyre, M. Basrai, M. Lichten, and A. Strunnikov. 2005. Condensin binding at distinct and specific chromosomal sites in the Saccharomyces cerevisiae genome. *Mol Cell Biol*. 25:7216-25.

Warsi, T.H., M.S. Navarro, and J. Bachant. 2008. DNA topoisomerase II is a determinant of the tensile properties of yeast centromeric chromatin and the tension checkpoint. *Mol Biol Cell*. 19:4421-33.

Yeh, E., J. Haase, L.V. Paliulis, A. Joglekar, L. Bond, D. Bouck, E.D. Salmon, and K.S. Bloom. 2008. Pericentric chromatin is organized into an intramolecular loop in mitosis. *Curr Biol*. 18:81-90.

Yong-Gonzalez, V., B.D. Wang, P. Butylin, I. Ouspenski, and A. Strunnikov. 2007. Condensin function at centromere chromatin facilitates proper kinetochore tension and ensures correct mitotic segregation of sister chromatids. *Genes Cells*. 12:1075-90.